Trinity College Dublin
Coláiste na Tríonóide, Baile Átha Cliath
The University of Dublin

X-ray Spectroscopic Studies of the Electronic Structure of Chromium based p-type Transparent Conducting Oxides

by

Emma Norton

A thesis submitted in partial fulfilment for the degree of Doctor of Philosophy

School of Physics

Faculty of Engineering, Mathematics and Science

March 2018

Le temps ne respecte pas ce qui se fait sans lui

\- *Paul Morand*

Declaration

I, Emma Norton, declare that this thesis has not been submitted as an exercise for a degree at this or any other university and apart from the advice, assistance and joint effort acknowledged and mentioned in the text, it is entirely my own work.

I agree to deposit this thesis in the University's open access institutional repository or allow the library to do so on my behalf, subject to Irish Copyright Legislation and Trinity College Library conditions of use and acknowledgement.

Signed: ______________________

Date: ______________________

Summary

In this thesis the electronic, optical, electrical, and mechanical properties of two p-type transparent conducting oxides will be explored, primarily by spectroscopic techniques. The initial chapters will outline how high optical transparency and electrical conductivity can co-exist within one material, so called Transparent Conducting Materials (TCMs). The most industrially relevant subset of these materials, n-type Transparent Conducting Oxides (TCOs), have been pervasive in optoelectronics. The p-type counterparts suffer from inferior properties.

One of these p-type TCOs, $Cr_{2-x}Mg_xO_3$, will be shown to have electrical properties that are not strongly correlated with crystalline quality. $Cr_{2-x}Mg_xO_3$ will be analysed by a variety of spectroscopic techniques: x-ray absorption spectroscopy, x-ray photoelectron spectroscopy and resonant photoemission spectroscopy. The consensus from this spectroscopic analysis will show that the charge carriers within the material created by magnesium doping are highly localised upon the Cr 3*d* states. Similarly, results from spectroscopy on a newly discovered p-type oxide, nanocrystalline Cu_xCrO_2 will demonstrate that charge carriers are also highly localised upon the Cr 3*d* states. The author will then conclude that these localised charge carriers can be correlated to the low mobility within chromium based oxides. The highly conductive nature of the copper deficient Cu_xCrO_2 films will be also linked the presence of copper vacancies within the material.

Despite the low mobility of some p-type oxides they have found applications within electronic devices. Two electronics devices (solar cells and transparent diodes) that will be dealt with in this thesis are composed of numerous interfaces: optimising these interfaces is crucial to maximising the performance of an

overall device. Chapter 3 will outline an experimental technique that can probe the energy band alignment of two materials. This technique will reveal that $Cr_{2-x}Mg_xO_3$ has the appropriate energy band alignment with ITO, the anode in an organic solar cell, to be an efficient selective contact for extraction of holes generated in the cell.

Separately, interface studies of a transparent diode of $Cr_{2-x}Mg_xO_3$ and ZnO will reveal that a large amount of defect states exist at the interface, leading to a high ideality factor for all $Cr_{2-x}Mg_xO_3$/ZnO diodes manufactured within this work.

Finally, the resilience of Cu_xCrO_2 to mechanical strain will be investigated by depositing it on flexible substrates and looking at the effects on the electrical properties of the thin films.

Acknowledgements

I would like to thank Prof. Igor Shvets for the opportunity to carry out my graduate studies within the Applied Physics Research group as well as advice and guidance throughout the process.

I would like to acknowledge the vast amount of time and effort Dr. Karsten Flesicher put into initially training myself and thereafter providing advice. It is due to his expertise that this thesis stayed on track.

I would like to thank past and current members of the Applied Physics Research group. In particular, Dr. Leo Farrell for his initial development of the p-type materials which I studied within this thesis. I'd like to thank Mr. Daragh Mullarkey for the growth all chromium oxide films by Molecular Beam Epitaxy, the co-development of the transfer mechanism for *in-situ* movement of samples and extensive proof reading. I'd like to thank Dr. David Caffrey for sharing his knowledge of magnetron sputtering.

I'd like to thank Prof. Daniel Bellet for allowing me the opportunity to visit his lab in Grenoble Institute of Technology to test the capability of our materials to be used as flexible electrodes.

I'd also to thank for Mr. Glenn Moynihan and Prof. David O'Regan from the Condensed Matter Theory group for collaborating with the Applied Physics Research group on theoretical calculations.

Finally, I'd like to thank everyone in School of Physics and CRANN who made working here over the past four years an enjoyable experience.

List of Publications and Presentations

Publications

Published

- **E. Norton**, L. Farrell, S.D. Callaghan, C. McGuinness, I.V. Shvets and K. Fleischer, *X-ray spectroscopic studies of the electronic structure of chromium-based p-type transparent conducting oxides*, Phys.Rev B **93**, 115302, 2016

- K. Flesicher, **E. Norton**, D. Mullarkey, D. Caffrey and I.V. Shvets, *Quantifying the Performance of P-Type Transparent Conducting Oxides by Experimental Methods*, Materials, **10(9)**, 1019, 2017

- D. Caffrey, **E. Norton**, C. O'Coileain, C.M. Smith, B. Bulfin, L. Farrell, I.V. Shvets and K. Fleischer, *Decoupling the refractive index from the electrical properties of transparent conducting oxides via periodic superlattices*, Sci Rep. **6**, 33006, 2016

- L. Farrell, **E. Norton**, C.M. Smith, D. Caffrey, I.V. Shvets and K. Fleischer, *Synthesis of nanocrystalline Cu deficient* $CuCrO_2$ *–a high figure of merit p-type transparent semiconductor*, Journal of Materials Chemistry C **4**, 126 - 134, 2016

- L. Farrell, K.Flesicher, D. Caffrey, D. Mullarkey, **E. Norton** and I.V Shvets, *Conducting Mechanism in the epitaxial* p-*type transparent conducting oxide* $Cr_{2-x}Mg_xO_3$, Phys. Rev. B **91**, 125202, 2015

- L. Farrell, **E. Norton**, B.J O'Dowd, D. Caffrey, I.V. Shvets and K. Fleischer, *Spray Pyrolysis of a high figure of merit* p*-type Transparent Conducting Material*, Applied Physics Letters **107** (3), 031901, 2015
- K. Fleischer, D. Caffrey, L. Farrell, **E. Norton**, D. Mullarkey, E. Arca, and I.V. Shvets, *Raman spectra of p-type transparent semiconducting Cr2O3:Mg*, Thin Solid Films **594**, 245-249, 2015

In Preparation

- **E. Norton**, L. Farrell, D. Mullarkey, D. Caffrey, D. Oser, D. Bellet, I.V. Shvets and K. Fleischer, *Transparent p-type conducting oxide for large area flexible electronics*, Applied Physics Letters
- **E. Norton**, **G. Moynihan**, D. Mullarkey, D. O'Reagan, I.V. Shvets and K. Fleischer, *Fundamental band gap of* Cr_2O_3 *and* $Cr_{2-x}Mg_xO_3$
- **E. Norton**, D. Mullarkey, I.V. Shvets and K. Fleischer, *Transparent pn junction with room temperature deposition of a p-type transparent conducting oxide*

Presentations

Posters Presentations

- *Energy band alignment of p-*$Cr_{2-x}Mg_xO_3$ *on ITO*, European Materials Research Society Meeting, Warsaw, 2015

Oral Presentations

- *Electronic structure of chromium-based p-type transparent conducting oxides studied by X-ray Spectroscopy*, German Physical Society Meeting, Dresden, 2015

- *Towards Transparent Diodes with p-*$Cr_{2-x}Mg_xO_3$, European Materials Research Society, Lille, 2016

- *Electronic structure of chromium-based p-type transparent conducting oxides studied by X-ray Spectroscopy*, Transparent Conducting Materials, Crete, 2016

- *Electronic structure of chromium-based p-type transparent conducting oxides studied by X-ray Spectroscopy*, Transparent Conducting Materials, Grenoble Institute of Technology, Grenoble, 2016

Contents

Glossary

Acronyms

ABL	Anode Buffer Layer
AC	Alternating Current
AE	Auger Electron
AZO	Aluminium doped Zinc Oxide (ZnO:Al)
BB	Band Bending
CAE	Constant Analyser Energy
CBL	Cathode Buffer Layer
CBM	Conduction Band Minimum
CBO	Conduction Band Offset
DC	Direct Current
DFT	Density Functional Theory
DOS	Density of States
FoM	Figure of Merit
FTO	Fluorine doped Tin Oxide (SnO_2:F)
FWHM	Full Width Half Maximum
GIXRD	Grazing Incidence X-Ray Diffraction
IGZO	Indium Gallium Zinc Oxide ($InGaZnO_4$)
ITO	Indium Tin Oxide (In_2O_3:Sn)
LED	Light Emitting Diode

LEED	Low Energy Electron Diffraction
MBE	Molecular Beam Epitaxy
MCP	Microchannel Plate Detector
OLED	Organic Light Emitting Diode
PEDOT	Poly(3,4-EthyleneDiOxyThiophene)
PID	Proportional Integral Derivative
PSS	Polystyrene Sulfonic Acid
RF	Radio Frequency
RIXS	Resonant Inelastic X-ray Scattering
RPES	Resonant Photoemission Spectroscopy
RSF	Relative Sensitivity Factor
SEM	Scanning Electron Microscopy
SPH	Small Polaron Hopping
TCM	Transparent Conducting Material
TCO	Transparent Conducting Oxide
TEY	Total Electron Yield
TFT	Thin Film Transistor
TTFT	Transparent Thin Film Transistor
UHV	Ultra High Vacuum
UPS	Ultraviolet Photoelectron Spectroscopy
UV-Vis	UltraViolet-Visible
VBM	Valence Band Maximum
VBO	Valence Band Offset
WF	Work Function
XAS	X-ray Absorption Spectroscopy
XMCD	X-ray Magnetic Circular Dichroism
XPS	X-ray Photoelectron Spectroscopy
XRD	X-Ray Diffraction
XRR	X-Ray Reflectivity

Symbols

a	Amorphous
c	Number of hopping sites
e	Charge of the electron
h	Planck’s constant
k	Initial energy level of the photoelectron
k_b	Boltzmann’s constant
l	Length
n	Refractive index
n_c	Bulk carrier concentration
n_s	Sheet carrier concentration
q	Elementary charge
s	Second
t	Thickness
w	Width
A	Absorption
B	Magnetic field
E	Energy value
E_a^2	Resolution of the analyser
E_{cl}	Core level
E_f	Fermi Level
E_{fs}	Final state of an electron
E_g	Band gap
E_{is}	Initial state of an electron
E_m^2	Minimum resolvable peak width

E_n^2	Natural linewidth energy distribution of electrons at that energy level
E_{pass}	Pass energy of photoelectron analyser
E_{vac}	Vacuum Level
E_x^2	Width of the photon line
E_{BE}	Binding energy of an electron
E_{CBM}	Energetic value of the Conduction Band Minimum
E_{KE}	Kinetic energy of an electron
E_{VBM}	Energetic value of the Valence Band Maximum
F	Figure of Merit
I	Current
K	Kelvin
L	Litres
Pa	Pascal
S	Siemens
SB	Seebeck Effect
T	Transmittance/Temperature
T_{av}	Average transmittance between 1.5 eV and 3 eV
R	Reflectance
R_{av}	Average reflectance between 1.5 eV and 3 eV
R_0	Path of an electron through photoelectron analyser
R_s	Sheet resistance
V	Voltage
W	Watt
α	Absorption coefficient
δ	Dispersion
η	Ideality factor
μ	Hall Mobility
μS	micro Siemens
ν	frequency

Θ	Angle
Θ_c	Critical angle
ρ	Resistivity
σ	Conductivity
ϕ	Work function
ϕ_{spec}	Work function of the photoelectron analyser
ω_p	Plasma frequency
Φ	Unoccupied density of states
Ψ	Wave function
Ω	Electrical resistance

List of Figures

List of Tables

Chapter 1

Introduction

Transparent Conducting Oxides (TCOs) are a specific subset of materials which possess both high optical transparency and electrical conductivity. TCOs have outshone other Transparent Conducting Materials (TCMs) not due to their superior performance but because of more practical benefits, i.e, they are easily patterned by lithography, stable in air and easily deposited over large areas [1]. One of the first reported TCOs, Indium Tin Oxide (ITO), was originally used to generate heat when deposited on aircraft windows thereby defrosting ice that built up on these screens [2]. Since then, the combination of possessing optical transparency while retaining a high conductivity have made TCOs pervasive in electronic devices, e.g, thin film solar cells, light emitting diodes, and flat panel displays [1, 3].

An important part of conventional electronic devices is based on having the availability of both p and n-type counterparts [4]. The focus of TCO research has moved to now designing a p-type. The original difficulty for TCO research lay in the unorthodox set of properties required for such materials: both high electrical conductivity (tending towards metals) and optical transparency (tending towards insulators) is a rarity in one material. The additional criteria of p-type conduction brought further complications due to fact the valence band of oxides are comprised of localized O 2*p* orbitals. Localized charge carriers will have a high effective mass, thereby lowering the conductivity of the material significantly. Only in 1997 was a p-type material of both high optical transparency and conductivity found [5]. Chapter 2 will outline the width and breadth of the transparent conducting materials that have been engineered since then; with a focus on materials that are industrially relevant. With such a wide range of TCMs a performance rating parameter is needed within the literature was required. A discussion on the appropriate use of the Figure of Merit, which is the performance rating parameter of choice within the literature will be included. The goal of this discussion is to provide an accurate picture of where chromium based p-type TCOs fit in the larger field, which will be the materials that will be focus of this thesis. Chromium based TCOs have been some of the newest discovered in the field [6].

The technology behind conventional semiconductor materials such as silicon and germanium relies on both p-type and n-type doping to be possible in the same parent material [7]. The ideal solution would be the possibility of p-type doping the best performing n-type oxides, e.g, In_2O_3 or ZnO: creating p-type conduction in the n-type counterparts has been difficult due to parasitic instrinsic defects that compensate the extrinsic p-type doping of the parent material [8].

Chromium (III) oxide is one of the few oxides that has shown stable p and n-type doping but suffers from relatively low electrical conductivity and mobility [9–12]. In Chapter 4, spectroscopic studies of p-type $Cr_{2-x}Mg_xO_3$ will provide insight into the electronic structure of the valence band and the origin of the low mobility of holes within this oxide.

Despite the fact that bipolar doping of the Cr_2O_3 lattice could lead to the “invisible circuit” proposed by Thomas in 1997 [13], a more tangible application for p-type oxides is the role they have found in laboratory devices. The incorporation of p-type $Cr_{2-x}Mg_xO_3$ films into prototype devices such as thin film solar cells and transparent diodes will be discussed. The valence band and conduction band offsets between $Cr_{2-x}Mg_xO_3$ in contact with other TCOs governs important properties of electronic devices. No general model for understanding how two oxides put into contact will align has been developed thus far. Chapter 4 will outline an experimental method that can map the interface properties of any two materials, which will be used to investigate the interface of $Cr_{2-x}Mg_xO_3$ with ITO and ZnO.

In spite of the prevalence of n-type TCOs within electronic devices they have been used as a passive layer, e.g, as a transparent contact, until the development of the n-type TCO Indium Gallium Zinc Oxide (IGZO). The high mobility that could be achieved for IGZO deposited at room temperature enabled it to become competitive with amorphous hydrogenated silicon as an active layer in flat screen displays [3]. In contrast, p-type oxides require extremely high deposition temperatures. The analogous p-type amorphous oxide to IGZO, Rhodium Zinc Oxide, has very low conductivity so is not appropriate for many industrial applications. In Chapter 5, the electronic and structural properties of a relatively low deposition temperature TCO, Cu_xCrO_2, will be explored. Such a low deposition temperature made this TCO compatible for growth upon flexible polyimide films. Hence, it will be investigated as a large area flexible p-type TCO electrode.

Finally, one overall objective within this thesis will be to investigate the fundamental physics behind the mobility of charge carriers within chromium based p-type transparent conducting oxides in the hope that by understanding the limitation of these materials the electrical properties could be improved.

Bibliography

[1] Monica Morales-Masis et al. “Transparent Electrodes for Efficient Optoelectronics”. *Advanced Electronic Materials* 3.5 (2017).

[2] D. B. Fraser and H. D. Cook. “Highly Conductive, Transparent Films of Sputtered $In_{2-x}Sn_xO_{3-y}$”. *Journal of The Electrochemical Society* 119.10 (1972), 1368.

[3] John F Wager. “Transparent electronics”. *Science* 300.5623 (2003), 1245–1246.

[4] Marius Grundmann et al. “Transparent semiconducting oxides: materials and devices”. *phys. stat. sol. (a)* 207.6 (2010), 1437.

[5] Hiroshi Kawazoe et al. “p-type electrical conduction in transparent thin films of $CuAlO_2$”. *Nature* 389 (1997), 939.

[6] Kelvin HL Zhang et al. “P-type transparent conducting oxides”. *Journal of Physics: Condensed Matter* 28.38 (2016), 383002.

[7] Marius Grundmann et al. “Oxide bipolar electronics: materials, devices and circuits”. *Journal of Physics D: Applied Physics* 49.21 (2016), 213001.

[8] S. B. Zhang, S.-H. Wei, and Alex Zunger. “Intrinsic n-type versus p-type doping asymmetry and the defect physics of ZnO”. *Physical Review B* 63.7 (2001).

[9] Arve Holt and Per Kofstad. “Electrical conductivity and defect structure of Mg-doped Cr_2O_3”. *Solid State Ionics* 100 (1997), 201.

[10] E. Arca, K. Fleischer, and I. V. Shvets. “Magnesium, nitrogen codoped Cr_2O_3: A p-type transparent conducting oxide”. *Appl. Phys. Lett.* 99.11 (2011), 111910.

[11] Tiffany C Kaspar et al. “Defect compensation by Cr vacancies and oxygen interstitials in Ti^{4+}-doped Cr_2O_3 epitaxial thin films”. *Physical Review B* 94.15 (2016), 155409.

[12] Aoife B Kehoe et al. “Assessing the potential of Mg-doped Cr_2O_3 as a novel p-type transparent conducting oxide”. *Journal of Physics: Condensed Matter* 28.12 (2016), 125501.

[13] Gordon Thomas. “Materials science: Invisible circuits”. *Nature* 389.6654 (1997), 907.

Chapter 2

An Overview of Transparent Conducting Materials

High optical transparency in the visible light regime ($h\nu$ = 1.5–3.1 eV) is rarely found in a material that is also an electrical conductor. Figure 2.1 illustrates the electronic structure of insulators, semiconductors and metallic conductors. Most insulators are highly optically transparent due to a fundamental band gap greater than 7 eV that means no absorption of photons will occur in the visible range. Metals have no band gap but are highly conductive. However there are several ways to artificially engineer transparency and conductivity within the same material.

This chapter will outline how these properties can coexist in materials and will highlight the necessity of Transparent Conducting Materials (TCMs). The literature's current Figure of Merit (FoM) for performance rating different transparent materials will be shown to be a useful metric to compare various different TCOs. However, the FOM does not reflect the true merit of a transparent material for an industrial application. Finally, the necessity of p-type transparent conducting oxides will be reviewed. An emphasis will be placed on the numerous chromium based transparent conducting oxides that have been reported recently.

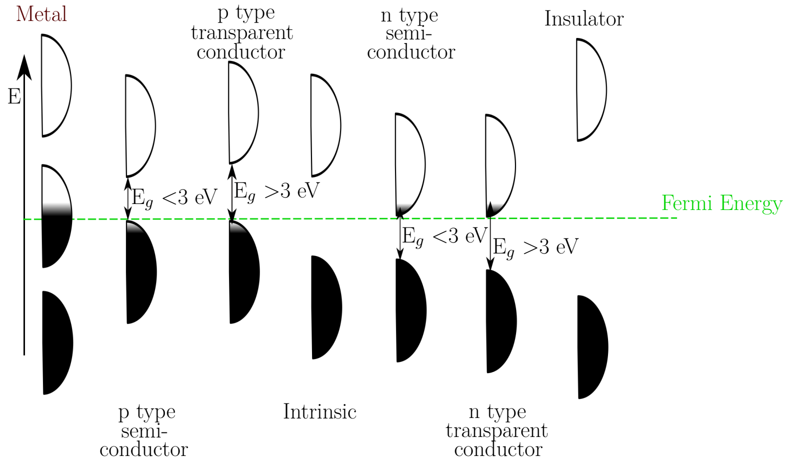

Figure 2.1: Comparison of the density of states for metals, insulators and semiconductors. Here, height represents energy while width is the density of available states at a certain energy in the material listed. The select shading of areas follows the Fermi-Dirac distribution (**black** = all states filled, white = no state filled, Green = Fermi Level).

2.1 Range of Transparent Conducting Materials

The simplest method of manufacturing a TCM is to reduce the thickness of an electrical conductor; the amount of light a material absorbs increases exponentially with thickness [1]. A single monolayer of graphene absorbs only 2.3 % of light and is considered a transparent conductor even though it possesses no band gap [2]. Alternatively, one can deposit a conductive nanowire array. Typically, these arrays are called nanowire networks. They are solution processed and then annealed to form junctions between the individual nanowires. The resulting mesh is flexible, conductive, and dispersed enough to allow penetration of light [3].

Another method of engineering a TCM is based on semiconductors which have a band gap and are poor conductors of electricity. Semiconductors can have their electronic properties altered through either intrinsic or extrinsic doping. Extrinsic, also called substitutional, doping involves replacement of bulk atoms with different elements. In a bulk sample small amounts of atoms, 10^{14} to 10^{20} cm^{-3} (up to 0.1 %), are replaced by higher (n-type) or lower (p-type) number of valence electrons. Substitutional doping is well researched for silicon. Neighbouring

Table 2.1: Comparing four concepts to achieve transparent electrodes: conducting oxides, organic conducting polymers, two-dimensional materials, metal nanowire networks

	Transparent Conducting Oxides (n-type)	Metal Nanowire Networks	Two-dimensional Materials	Organic Conducting Polymers
Electronic Band Structure	Doped semiconductor with Fermi level within the conducting band Optical Band gap <4 eV	Metallic conduction Small diameter and space between nanowires gives rise to transparency	Dirac Cone, Zero Band Gap Transparency arises from low absorption with atomic monolayer	HOMO-LUMO >3eV . Charge Transfer Complex:
Range of Materials	ITO, AZO, FTO, IGZO, IZO, ZTO	Ag, Cu, Au, Ni, Zn, C	Graphene	PEDOT:PSS, PPS, PT, PPY, PANI, PAC, PPV
Sheet Resistance	1-100 Ω/sq.	500-3000 Ω/sq.	500-3000 Ω/sq.	500-3000 Ω/sq.
Deposition	Magnetron Sputtering (RF, DC) [4] Spray Pyrolysis Atomic Layer Deposition Chemical Vapour Deposition Spin Coating	Drop casting [5] Spray Coating [5] Nanoimprinted Wire Meshes [6]	Chemical Vapour Deposition [7] Mechanical Exfoliation [8] Ultrasoniation + Dropcasting [8]	Spin Coating [9]
Industrial Uptake	Widely used most devices that require an transparent electrode	Prototype Devices	Prototype Devices	Prototype Devices
Limitations	Cost (Indium) [10] No industrial p-type counterpart	Stability in air Cost (Ag)	Difficult to Upscale [11] High resistance in practical devices [11]	Stability [12]

elements on the periodic table e.g., boron, phosphorous, and arsenic are substituted for silicon atoms. Since phosphorus/arsenic have five valence electrons when coordinated within the lattice of silicon atoms the extra valence electron is loosely bound. This creates donor levels that lie just below the conduction band. Thermal energy at room temperature is usually sufficient to promote the donor electrons into the conduction band.

However, bulk silicon, in an undoped state, has an optical band gap of 1.14 eV which means it will not be optically transparent [13, 14]. If the optical band gap is larger than 3.1 eV no absorption of light will occur within the visible regime and it will be transparent to the human eye. This is illustrated in Figure 2.1. Intrinsically doped cadmium oxide (CdO) was the first transparent conducting oxide reported in 1907 [15]. CdO had a visible transmission of greater than 60 % (between photon energies of 1.5-3.1 eV) and possesses a low sheet resistance of 30-60 Ω/□, performing well as a n-type Transparent Conducting Oxide (TCO) film [16]. However, the toxicity of cadmium limited widespread applicability within industry. A solid solution of In_2O_3 and SnO_2 (ITO) produces films that can have greater than 90 % transparency and sheet resistance as low as 10 Ω/□ [17].

Organic transparent conductors are another subset of doped materials that do not absorb light below the threshold of 3.1 eV. Organic conductors are composed of carbon atoms forming the polymer backbone. Where semiconductors like silicon are substitutional doped, the conductivity of organic conductors is linked to the intrinsic mobility of the carbon polymer chain but improved by oxidising or reducing the material. Organic conductors are printable over a large area at a relatively low cost. The most successful organic conductor has been poly(3,4-ethylenedioxythiophene) doped with polystyrene sulfonic acid (PEDOT:PSS). Recently, the lowest value of the conductivity for PEDOT:PSS (50 Ω/□) is achieved when treated by sulphuric acid [18].

2.2 Figure of Merit

As outlined above there are three or four methods of engineering a TCM. Within each of these subsets there is a high frequency of newly reported or refined materials. With an expanding field of new TCMs a performance rating has been sought: this has often fallen to the Figure of Merit (FoM). It would seem intuitive to define the FoM as weighting the transmittance versus electrical sheet resistance. The transmittance is the ratio of light incident on the material versus the light that passes through the material. The definition of electrical sheet resistance can be derived from the bulk resistivity, ρ , of a three dimensional sample:

$$R_{\text{3D}} = \frac{\rho * \text{l}}{\text{w*t}} \tag{2.1}$$

where l is the length, w is the width and t the thickness of the sample. If uniform thickness of a thin is assumed the resistivity, ρ, the thin film resistance can be written as:

$$R_{\text{thin film}} = \frac{R_s * \text{l}}{\text{w}} \tag{2.2}$$

Sheet resistance is the measurements of thin films which are considered two dimensional objects. Sheet resistance measurements were carried out with a linear four point probe geometry.

The thickness of our thin films can be precisely determined by X-ray Reflectivity (XRR), outlined in section 3.10. Therefore the resistivity of the sample can be calculated from the sheet resistance, R_s as:

$$\rho = R_s * \text{t} \tag{2.3}$$

Resistivity has the standard unit Ωm. This would make the unit of sheet resistance Ω. The sheet resistance is conventionally defined as ohm per square (Ω/□) which is dimensionally the same. The naming convention represents an “aspect ratio": if the sheet resistance of a thin film is 10 Ω it has an actual resistance of 10 Ω, regardless the size of the square.

In fact directly weighting sheet resistance versus transmittance was the original suggestion by Fraser and Cook for a FoM:

$$F_{\text{Fraser, Cook}} = \frac{T}{R_s} = \sigma t e^{-\alpha t} \tag{2.4}$$

where T is the transmittance and R_S is the sheet resistance, α is the absorption coefficient and t is the thickness of the material [19]. The absorption coefficient (α) describes the extent to which the radiant flux of a light beam is reduced as it passes through a specific material. It was noted by Haacke shortly after that this definition weights too heavily in favour of electrical conductance [20]. The maximum FoM would occur at a thickness where the optical transmission would be only 37 %. Such a transmittance is too low for most transparent conductor applications. Haacke suggested an improvement on the FoM:

$$F_{\text{Haacke}} = \frac{T^x}{R_s} = \sigma t e^{-x\alpha t} \tag{2.5}$$

Haacke chose empirically the value of x to be ten so that the maximum FoM would occur at ninety percent transmission, which is the ideal optical transparency required for most electro-optical devices. This is readily used in many review papers for silver nanowires networks and transparent electrodes [21]. However, when compared to the previous $F_{\text{Fraser, Cook}}$ the maximum of F_{Haacke} occurs at a reduced thickness and as the sheet resistance is a function of the thickness:

$$R_s = \frac{\rho}{t} \tag{2.6}$$

where ρ is the resistivity of the film: this unfairly weights the performance of materials that are highly conductive materials at very low thicknesses, like silver nanowire networks. Several papers subsequently suggested alternative FoMs but the most notable is the uptake of the FoM developed by Jain and Kulshreshtha but popularised by Gordon in a Material Research Society Bulletin [22, 23]. This FoM weights the electrical conductivity against the absorption coefficient, both bulk material properties:

$$F_{\text{Gordon}} = \frac{\sigma}{\alpha} = -\frac{t}{\rho}.\frac{1}{\ln(T_{av} + R_{av})} = -\frac{1}{R_s \ln(T_{av} + R_{av})} \tag{2.7}$$

where ρ is the film resistivity, t is the thickness, T_{av} and R_{av} are the average reflectance and transmittance between 1.5-3.1 eV [23].

To acquire the absorption coefficient (α) of a thin film the transmittance (T) and reflectance (R) spectra of the material is taken by UV-Vis spectroscopy. The absorptance of a material is then be related to the transmittance and reflectance by the following relation:

$$T + R + A = 1 \tag{2.8}$$

Utilising the Beer Lambert law the absorption coefficient can then be approximately related to T and R by the following equation:

$$\alpha = \frac{-ln(T + R)}{t} \tag{2.9}$$

where t is the thickness of the thin film being analysed. The thickness of a thin film was measured precisely by X-Ray Reflectivity (XRR).

$\mathrm{F}_{\text{Gordon}}$ is theoretically independent of thickness if the microstructure of the film does not depend on thickness. However, the original paper cautioned to choose thin films of constant thickness when comparing different materials due to the fact that many transparent conducting materials have morphologies that varying with thickness e.g., polycrystalline thin films.

It should be noted a single value of FoM is unique to a single absorption coefficient to conductivity ratio. However, it is not unique to one value of transmittance or sheet resistance for a material. Figure 2.2 illustrates the range of R_s vs transmission and reflectance values that will give the same value of FoM. A single

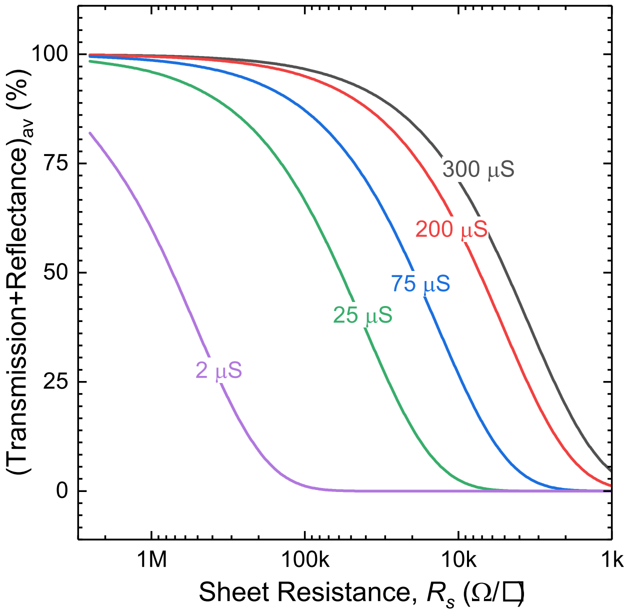

Figure 2.2: Plot showing the range of R_s vs transmission ratios that will give the same value figure of merit. A range of values of the FoM are plotted (2-300 μS).

material can traverse a range of a sheet resistance, transmittance and reflectance values but maintain a single value of the FoM. Ideally a comparison between various TCM should be made only when you can compare the bulk values of DC electrical conductivity and absorption coefficient. However, many papers only provide one value of sheet resistance and one value transmittance, no reflectance measurement. If reflectance measurements are not performed (which occurs frequently in the literature) the thickness independence of $\mathrm{F_{Gordon}}$ is negated and the FoM is altered to:

$$F_{\mathrm{Gordon}} = \frac{\sigma}{\alpha} \approxeq \frac{t}{\rho} . \frac{1}{\ln(T_{av})} \tag{2.10}$$

The reflectance losses can be detrimental to the performance of a TCM and should be included in the FoM . However, these reflectance losses could be alleviated when embedded into a real device with an overlayer like a metal contact and so the use of equation 2.10 could be argued to be justified.

However, to illustrate the dependence of the modified FoM on film thickness, figure 2.3 shows the modelled transmission of films of n-type ZnO on glass, for

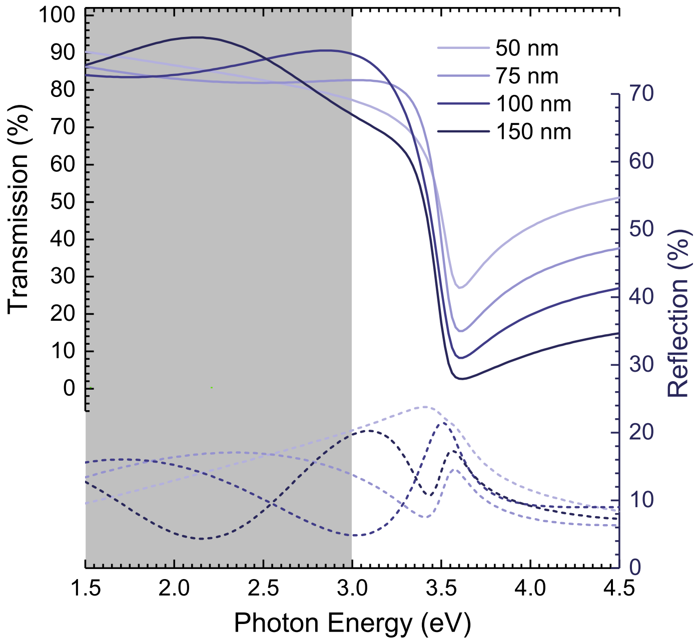

Figure 2.3: Modelled transmission and reflection data of ZnO thin films on glass. The grey spectral region was used to calculate the average transmission and reflection.

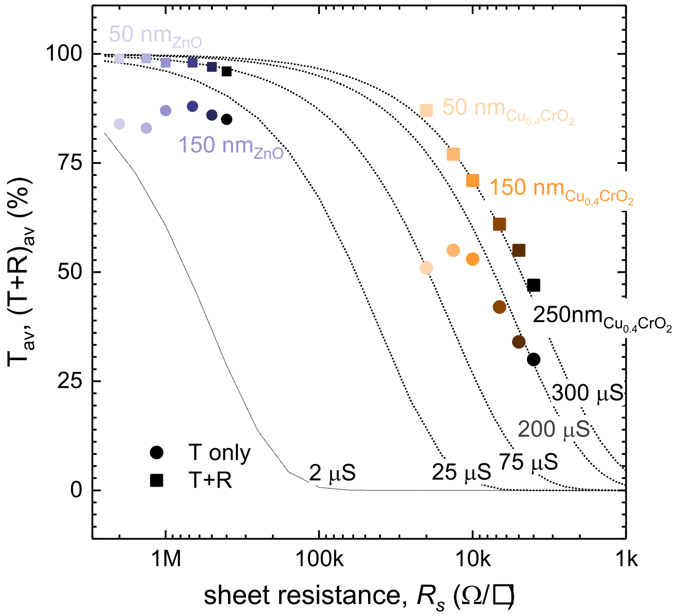

Figure 2.4: Figure of merit of ZnO and Cu$_{0.4}$CrO$_2$ thin films of varying thickness using average transmission and reflectance T+R (■) versus only average transmission T (●)[15, 24–32].

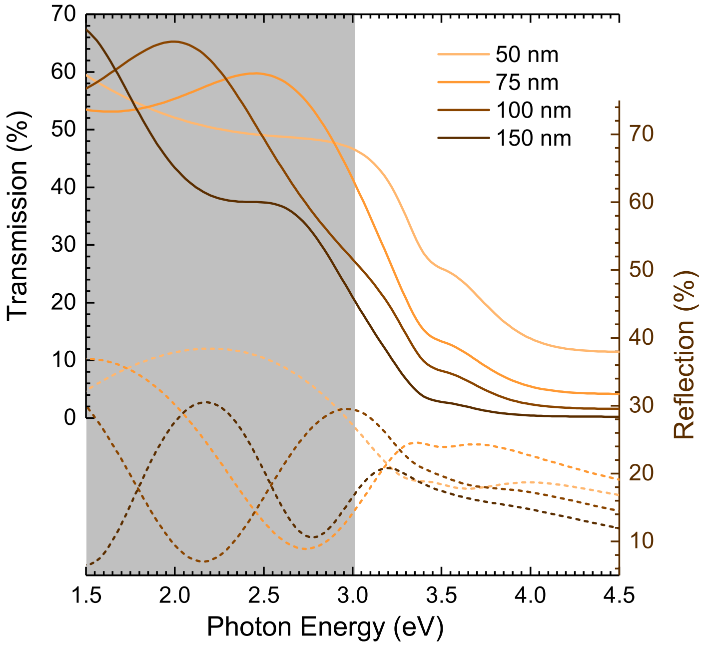

Figure 2.5: Modelled transmission and reflection data of $Cu_{0.4}CrO_2$ thin films on glass. The grey spectral region was used to calculate the average transmission and reflection.

thicknesses between 50 and 150 nm.

The low amplitude of the Fabry-Pérot interference fringes results in a minimal change in the average transmission as a function of thickness. . These Fabry-Pérot interference fringes arise from two films of differing refractive index with thicknesses on the order of the wavelength of visible light causing interference fringes. The amplitude these fringes will vary with film thickness and the difference between the refractive indices. Figure 2.4 plots the FoM calculated from equations 2.7 and 2.10. If equation 2.7 is used the value of the FoM is constant as a function of thickness, as expected. However, an order magnitude change in the value of the FoM is seen if using $\ln T_{av}$ within the thickness range of 50 to 150 nm. The small change in the average transmission impacts the FoM for equation 2.10 strongly due to the fact that intrinsically doped ZnO has a high sheet resistance.

Across all materials the magnitude of this effect over a thickness range will not be constant as it depends on the refractive index. The reflectance and transmission spectra are modelled for p-type $Cu_{0.4}CrO_2$ thin films of thickness 50 nm to 150 nm upon glass in figure 2.5. The reflectance at 50 nm reaches a maximum of 30 %. Above a thickness of 150 nm the occurrence of several Fabry-Pérot oscillations keeps the value of the average reflectance value more stable. Even though the magnitude of the effect is larger for p-type $Cu_{0.4}CrO_2$, the FoM calculated with just the average transmission ranges from a value of 75 μS and 200 μS between the thickness range of 50-250 nm. This is a smaller change than the ZnO films due to the fact that the value of the FoM for $Cu_{0.4}CrO_2$ is dominated by the low sheet resistance, within the k$\Omega/\square$ range.

These simulations illustrate that caution should be used when rating the merit of a particular TCO against the FoM's of other TCOs from the literature if reflectance measurements have not been performed.

2.3 Applications

Normally, the specific requirements of a material for an application extend beyond the absorbance to conductivity ratio. ITO was the industry standard TCM until the rising cost of indium warranted a replacement. Despite many viable alternative n-type oxides researched e.g., zinc oxide doped with aluminium (AZO) and tin oxide doped with fluorine (FTO) [33] none have replaced ITO entirely. ITO has a set of characteristics that extend beyond high FoM and mobility such as the ability to be precisely etched into patterns and resistance to degradation via moisture or air [34].

Recent trends have pushed for lower sheet resistance, increased mechanical flexibility and reduced cost. Areas where ITO is not the optimum material, leading to alternative TCMs becoming viable [21]. Typical devices requiring materials that are transparent yet also electrical conductors include touch-screens, smart windows, solar cells, and Organic Light Emitting Diodes (OLEDs). Each application has a set of requirements that has to be met [35].

2.3.1 Thin Film Transparent Transistors

The FoM can indicate suitable candidates for Thin Film Transistors (TFTs) but crucial parameters for TFTs are not considered by the FoM alone. Additional requirements for TFTs are not extensive but quite restrictive. Carrier mobilities well above 1 $cm^2V^{-1}s^{-1}$ are essential to be competitive with hydrogenated amorphous silicon based electronics. Secondly, the carrier density should be highly controllable between the values of 10^{18} cm^{-3} and 10^{19} cm^{-3}.

Individual n-channel transistors made of n-type TCOs are already commercially available [36]. The initial vision was to have the capabilities to manufacture fully transparent devices with conventional Complementary Metal-Oxide-Semiconductor (CMOS) technology [37]. Hence considerable research focus is dedicated to p-channel TCOs for Transparent Thin Film Transistors (TTFT). Section 2.4 provides a review of the progress in this area. Despite the not yet commercially realised TTFTs, p-type TCOs have found a multitude of uses within other laboratory devices; a few of which will be outlined below.

2.3.2 Solar Cells

Transparent conductors have a multitude of applications within the industry of solar energy generation. The largest of these applications is to serve as low emittance windows. For solar cells, it is paramount that the selected TCM has a low contact resistance to both the electrodes and active layers. It must be possible to manufacture the material uniformly over large areas. Chemical and environmental stability of the TCM may be a factor to extend the operational lifetime of the solar cell [38]. Within this area, a specific application for p-type transparent conductors is as an Anode Buffer Layer (ABL) in thin film solar cells/OLEDs. ABL maximises hole extraction/injection by having a valence band structure well aligned with a high work function contact and active layer(s) [39].

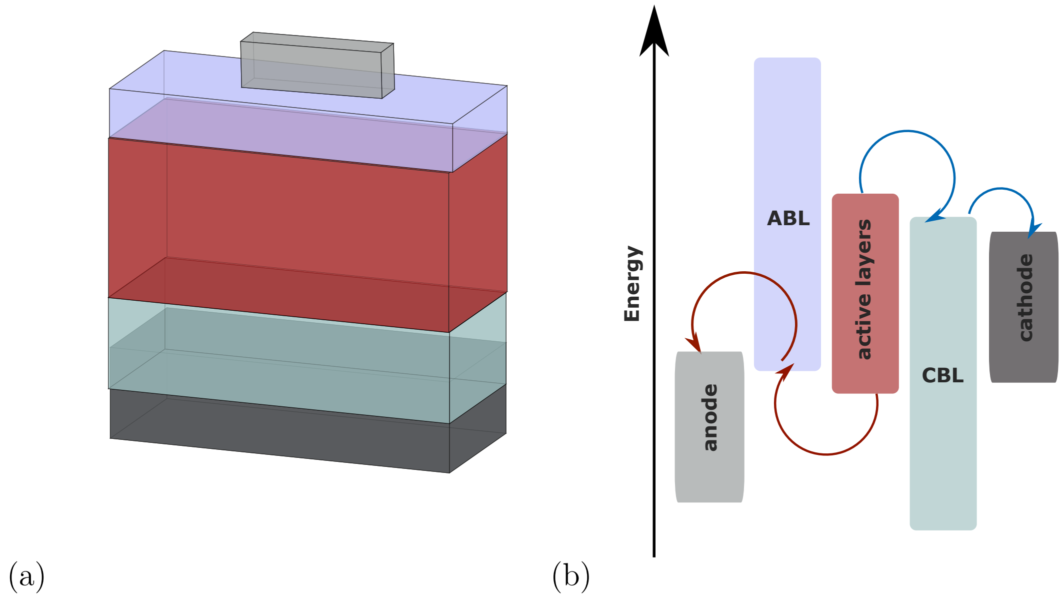

Figure 2.6: (a) Geometry for the component layers in a thin film solar cell (b) Energy band diagram; ABL = Anode Buffer Layer and CBL = Cathode Buffer Layer. The red arrow indicates the extraction of holes from the cell while blue arrows indicate the extraction of holes.

Simultaneously, it should create a barrier for electrons from the active layer to reduce device shunting. This is realised by the creation of a large conduction band offset. The requirements vary for each device. If we take the specific example of bilayer hetero-junction solar cells; the front contact is the anode. As the anode electrode (which is typically composed of ITO/FTO) is the front contact the ABL needs to also have high transparency to maximise light reaching the active layer. To date the most commonly used ABL in these types of solar cells are polymers like PEDOT:PSS, or metal oxides MoO_3, V_2O_5, WO_3, Cr_2O_3, and NiO [40, 41].

The development of new materials for each of the above applications is crucial. Subsequent to the development of the material is optimising the alignment of the constituent materials of a device. Most devices are composed of numerous interfaces: each interface can be optimised by changing the deposition conditions or carrier concentration to maximise the performance of the device, e.g., the efficiency of a solar cell. No general theoretical model exists to accurately predict the energy band alignment of two surfaces such as Anderson's rule [42]. Experimental methods developed have been much more reliable at aligning the interface of two oxide layers in a device [43]. Section 3.2 will outline the experimental method of such measurements. The following sections will first outline which p-type materials are of relevance to industry presently.

2.4 p-type Transparent Conducting Oxides

Due to the widespread use of n-type TCOs in optoelectronic devices and other niche applications an analogous p-type TCO was sought. Ninety years since the first report of a TCO, thin films of nickel oxide were reported as the first *p*-type TCO with low transparency of less than 50 % in the visible spectral range [44, 45]. Since then a range of TCOs have been developed with varying FoMs (see figure 2.7). Unfortunately, *p*-type conductors have suffered from low transparency and low carrier mobility.

2.4.1 Mobility in Metal Oxides

$$\sigma = n_e q_e \mu_e + n_h q_h \mu_h \tag{2.11}$$

The total electrical conductivity is the sum of the conductivities of the valence and conduction band carriers, which are holes and electrons, respectively. It can be expressed as where n_e, q_e, and μ_e are the electron's concentration, charge and mobility, and n_h, q_h, and μ_h are the hole's concentration, charge and mobility, respectively. The FoM of a TCO can be linked to the conductivity via the sheet resistance R$_s$.

$$R_s = \frac{1}{t * (n_e q_e \mu_e + n_h q_h \mu_h)} \tag{2.12}$$

where t is the thickness of the material being analused. However, the mobility and carrier concentration of a TCO can vary between two differing materials and not be reflected in the FoM. It is important to characterise the sheet resistance (R$_s$), concentration (n) and mobility (μ) of the majority carriers of a TCO to understand what applications a TCO is applicable for. The FoM for a TCO does not solely contain all this information. This characterisation of these three quantities will be done in this work for both $Cr_{2-x}Mg_xO_3$ and $CuCrO_2$by measuring the valence band structure. How the mobility and carrier concentration can be linked to the band structure will be discussed below:

The mobility is a quantity that directly relates the drift velocity ν_d of holes to the applied electric field E across the material, i.e. $\nu_d = \mu E$. The hole density (holes/volume) in the valence band is obtained by integrating $g(E)f(E)dE$ (density of states × probability of occupancy of states) from the bottom to top of the valence band.

$$n_h = \int_{\infty}^{E_{vb}} g(E)f(E)dE \tag{2.13}$$

where

$$g(E) = \frac{\sqrt{2}m_h^*}{\pi^2\hbar^3}(E_{vb} - E)^{\frac{1}{2}} \tag{2.14}$$

and

$$f(E) \approx \exp\left(-\frac{E - E_f}{k_b T}\right) \tag{2.15}$$

if we assume that $E - E_f \gg k_b T$. The number of mobile charge carriers can be obtained by performing the integration of Equation 2.13 resulting in the equation

$$n_h = N_v \text{exp}\left(-\frac{E_f - E_{vb}}{k_b T}\right) \tag{2.16}$$

where

$$N_v = 2\left(\frac{m_h^* k_b T}{2\hbar^2}\right)^{\frac{3}{2}} \tag{2.17}$$

N_v is the effective density of states for the edge of the valence band. The effective mass, m_h^*, is directly related the dispersion within the valence band. Low dispersion of the valence band will give a high effective mass resulting in the low mobility of the charge carriers. Metal oxides have a valence band that is largely composed of localised $2p$ oxygen orbitals. This will lead to a low mobility if the

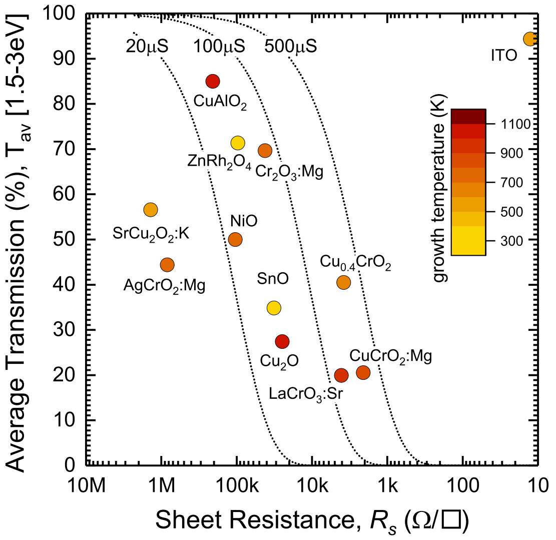

Figure 2.7: Comparison of the average transmission and sheet resistance from the literature data of a range of p-type TCOs. The reported literature data have been adjusted to account for varying thickness between samples and the average transmission was taken over an energy range of 1.5-3 eV. The film thickness chosen to compare TCOs was 150 nm to avoid underestimating the transparency due to the possibility of a broad Fabry Pérot interference fringe at lower film thickness. Dotted lines of constant figure of merit are included[15, 24–32]

majority carriers are holes, like p-type metal oxides.

Cu_2O was reported as the first high mobility p-type oxide (100 cmV^{-1}s^{-1}) with a band gap of 2.1 eV but readily oxidises in air to CuO which has both low mobility and transmission. If the transparency and stability could be improved Cu_2O would be one of the optimum candidate materials for devices.

The strategic development of an improved p-type TCO was sought by chemical modulation of the valence band. The delafossite $CuAlO_2$ was designed to create delocalisation of the valence band. Delafossites have the formula ABO_2 where the A cation site (usually copper for *p*-type TCOs) is linearly coordinated to oxygen octahedra within which the B cation sits. This linear coordination of copper and oxygen leads to increased hybdrization of the O 2*p* and Cu 3*d* electrons lowering the oxygen character of the valence band, creating a more dispersed valence band. $CuAlO_2$ showed low *p*-type conductivity of 1 Scm^{-1} at room temperature but reasonable transparency [46]. This finding led to the outline of a design rule for *p*-type TCOs requiring the presence of Cu^{+1} and motivated the study of a range of Cu-based materials such as $CuBO_2$ where B = boron [47], scandium [48], chromium [25], gallium [49], yttrium [50], indium [51], lanthanum [52]. Delafossites made significant improvements for p-type transparent conductors but

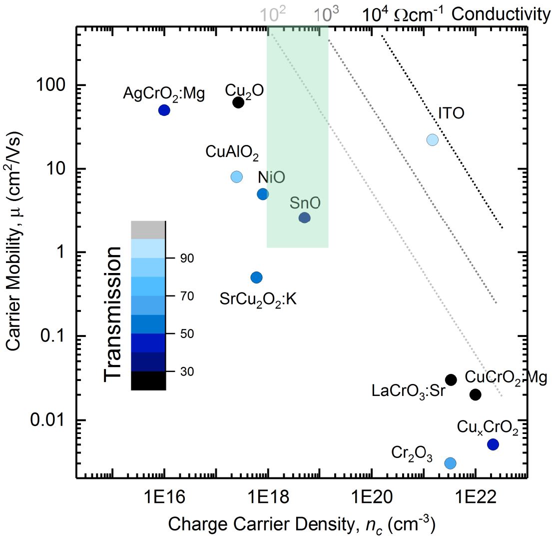

Figure 2.8: Carrier mobility, μ versus carrier density, n_c, for a set of transparent conducting oxides. An inset with a transparency scale is included. The average transparency each material is quantified in the colour of the data point. The transparency of the transparent conducting oxides is included as it is important to reflect the trade off that occurs for improved mobility over reduced transmission. The mobilities of $Cr_{2-x}Mg_xO_3$, $LaCrO_3$ and Cu_xCrO_2 are estimated using a small polaron model with the Seebeck effect [25, 26, 30–32, 53, 56, 57]. The shaded area indicates the optimum region for transparent thin film applications.

compared to their n-type counterparts had orders of magnitude lower conductivities and reduced transparency. Furthermore, the ionization levels of thermally activated copper vacancy acceptor states would make degenerate conductivity impossible [53]. $CuCrO_2$:Mg showed much lower thermally activated carriers compared with other delafossites but had a much lower charge carrier mobility [25, 54, 55]. In fact, it is often reported as the highest performance p-type TCO due to a large FoM even though the Hall mobility could only be measured by the AC Hall effect. These findings suggest that $CuCrO_2$ has an improve conductivity in a doped and undoped state due to the presence of the Cr 3*d* states within the valence band but also resulted in a lower mobility of the charge carriers compared with other cuprous delafossites.

Following this Cr_2O_3 itself was reported as a p-type transparent conductor when doped with magnesium. $Cr_{2-x}Mg_xO_3$ was thought to be nitrogen doped when the addition of an ammonium precursor improved the optical transparency of the $Cr_{2-x}Mg_xO_3$. Near edge absorption spectroscopy showed that the nitrogen wasn't incorporated into the Cr_2O_3 lattice in large quantities. The ammonium precursor may be specific to spray pyrolysis to aid a reaction mechanism that reduces the present of parasitic defects, increasing optical transparency. Nitrogen detection by spectroscopy in small quantities is difficult due to it's low atomic mass; a quantity below 10^{14} cm^{-3} could be present in all deposition techniques when growing $Cr_{2-x}Mg_xO_3$ films due to a nitrogen rich atmosphere [58]. The mobility of the charge carriers being below the measurable limit for the AC and DC Hall effect in $Cr_{2-x}Mg_xO_3$ was attributed to the poor crystallinity grown via spray pyrolysis. Later studies showed that the hole mobility of epitaxial $Cr_{2-x}Mg_xO_3$ was not measurable: a lower limit for the hole mobility of 10^{-4} $\mathrm{cm}^2\mathrm{V}^{-1}\mathrm{s}^{-1}$ was estimated by the Seebeck effect assuming a small polaron hopping conducting mechanism [32].

Chromium oxide fits a lot of the industrial criteria: processable by magnetron sputtering, composed of earth abundant non-toxic elements and of high chemical stability. Bipolar doping (both p and n-type dopable) of the chromium oxide lattice is also possible [59], which is key to conventional semiconducting processes [60]. Bipolar doping of an oxide is a rare property only found in two other transparent oxides: zinc oxide and tin oxide [61, 62]

The leading oxide for p-channel TTFTs is tin oxide (SnO). As seen in figure 2.8 SnO has the optimum carrier concentration and mobility (shaded region for TTFTs. Large drawbacks for tin oxide is high leakage current in prototype TFTs and these devices are highly unstable at atmosphere [29].

2.4.2 Deposition Temperature

With an increasing range of p-type materials available the deposition temperature has emerged as an important criteria. Excessive temperatures can hamper incorporation into devices. The initial p-type oxide materials: NiO, delafossites and Cu_2O all require high deposition temperatures to be highly conductive [25].

p-type SnO was the first highly conductive transparent material with a reported deposition temperature less than 400 K [63], but the n-type amorphous

$InGaZnO_4$ (IGZO) demonstrates high mobilities of greater than 10 $cm^2V^{-1}s^{-1}$ with a high visible transparency, when deposited at room temperature. Previous amorphous semiconductors, such as hydrogenated amorphous silicon, have limited carrier mobility due to the highly directional nature of p-orbitals. a-IGZO has a conduction band composed of s-orbitals, which results in a conduction pathway insensitive to a lack of crystalline order [64]. Based on these promising findings an analogous amorphous p-type was designed $ZnRh_2O_4$ [65]. Even though it achieves room temperature conductivity, it was a poorly conducting material with an immeasurable Hall mobility. Lowering the deposition temperature while retaining high conductivity is a crucial barrier to p-type materials being incorporated into devices.

2.4.3 Alternatives to p-type Oxides

A high mobility transparent p-type oxide, deposited at low temperature, may never become reality. As a result of poorly performing p-type oxides the concept of chemical valence band modification has been extended to the replacement of oxygen for other chalcogenide atoms. LaCuOS was one of the first materials discovered to be p-type possessing a large optical band gap of 3.1 eV. Unfortunately, conductivity when acceptor doped with Sr was low (0.26 Scm^{-1}) [66]. Replacement of sulphur for selenium (LaCuOSe) increased the conductivity of the lattice, especially when doped with Mg producing a degenerate p-type material with conductivity 10^2 Scm^{-1} [67]. Increased conductivity in LaCuOSe arose from increased hybridization of Cu 3*d* orbital with Se 4*p* compared with S 3*p* but at the expense of transparency [68]. The most promising material has been BaCuTeF thin films exhibiting maximum conductivity of 167 Scm^{-1}, mobility of 8 $cm^2V^{-1}s^{-1}$ and band gap of 3 eV [69].

The movement away from chalcogenides (Group 6 elements) towards pnictogens (Group 5 elements) has also been explored. Cu_3N is a metastable compound that that has direct band gap of 1.0 eV and conductivities of 10^3 Scm^{-1}. It has been identified as having shallow n-type and p-type defects, ideal for fabrication of p-n junctions. Cu_3N possessing such a low band gap would not regard it as a transparent semiconductor, but likely a competitor for silicon and germanium in solar cells. MCuP (M = Ca, Sr, Ba) compounds have been calculated to have disperse valence band maximums. The only experimental synthesis as of yet is the bulk powder of CaCuP showing a conductivity value of 10^3 Scm^{-1} and the onset of optical absorption at 2.7 eV. No mobility measurements could be made from the bulk pressed pellet [70].

The most promising TCM to date has been Copper Iodide (CuI). A degenerate p-type conduction of CuI thin film is achieved at the iodine-rich growth condition, allowing for a record high room-temperature conductivity of 156 Scm^{-1} for as-deposited CuI and $\approx$ 283 Scm^{-1} for I-doped CuI. At the same time, the films appear clear and exhibit a high transmission of 60–85% in the visible spectral range. The realization of such simultaneously high conductivity and transparency boosts the figure of merit of a p-type TC: its value jumps from 200 to 17,00 μS [71].

The exploration of replacing oxygen with other elements has produced progress towards a higher mobility transparent conductor. Yet, the initial field of p-type TCOs was spurred by the success of ITO. ITO is easily processable via DC magnetron sputtering with low/medium deposition temperature,contains non-toxic elements and most importantly is stable in air [34]. Ternary/quaternary compounds would complicate large area deposition. Sulphur, selenium, tellurium, fluorine and phosphorus all require toxic gases or compounds to process. Replacement of the anion with anything other than oxygen often makes the TCM highly unstable in air. For example, the excellent electrical and optical properties of CuI degrade significantly after several hours in ambient conductions [71]. Hence, this thesis explores the limits and physical origin of the mobility limitation of two promising p-type oxides: a low temperature highly conductive material (Cu_xCrO_2) and a highly transparent low conductivity material that can be bipolar doped ($Cr_{2-x}Mg_xO_3$).

Bibliography

[1] HJ Trodahl. “Optical absorption in thin films”. *Journal of Physics E: Scientific Instruments* 17.1 (1984), 27.

[2] A. B. Kuzmenko et al. “Universal Optical Conductance of Graphite”. *Physical Review Letters* 100.11 (2008).

[3] Sukanta De et al. “Silver Nanowire Networks as Flexible, Transparent, Conducting Films: Extremely High DC to Optical Conductivity Ratios”. *ACS Nano* 3.7 (2009), 1767.

[4] Spyros Diplas et al. “An in situ XPS study of growth of ITO on amorphous hydrogenated Si: Initial stages of heterojunction formation upon processing of ITO/a-Si: H based solar cell structures”. *physica status solidi (a)* 212.1 (2015), 47–50.

[5] Dong Yun Choi et al. “Annealing-free, flexible silver nanowire–polymer composite electrodes via a continuous two-step spray-coating method”. *Nanoscale* 5.3 (2013), 977–983.

[6] Melinda Mohl et al. “Self-assembled large scale metal alloy grid patterns as flexible transparent conductive layers”. *Scientific reports* 5 (2015), srep13710.

[7] Jingxue Yu et al. “Synthesis of high quality two-dimensional materials via chemical vapor deposition”. *Chemical Science* 6.12 (2015), 6705–6716.

[8] Hai Li et al. “Mechanical Exfoliation and Characterization of Single-and Few-Layer Nanosheets of WSe_2, TaS_2, and $TaSe_2$”. *Small* 9.11 (2013), 1974–1981.

[9] Yonghee Kim et al. “Controlled electro-spray deposition of highly conductive PEDOT: PSS films”. *Solar Energy Materials and Solar Cells* 98 (2012), 39–45.

[10] Lei Zhang et al. “Correlated metals as transparent conductors”. *Nature materials* 15.2 (2016), 204–210.

[11] Francesco Bonaccorso et al. “Production and processing of graphene and 2d crystals”. *Materials today* 15.12 (2012), 564–589.

[12] MP De Jong, LJ Van Ijzendoorn, and MJA De Voigt. “Stability of the interface between indium-tin-oxide and poly (3, 4-ethylenedioxythiophene)/poly (styrenesulfonate) in polymer light-emitting diodes”. *Applied Physics Letters* 77.14 (2000), 2255–2257.

[13] Guido Masetti, Maurizio Severi, and Sandro Solmi. “Modeling of carrier mobility against carrier concentration in arsenic-, phosphorus-, and boron-doped silicon”. *IEEE Transactions on electron devices* 30.7 (1983), 764–769.

[14] S.M. Sze. *Physics of Semconductors.* Ed. by S.M. Sze. Wiley-Interscience, 1969.

[15] K. Badeker. “Cadmium Oxide”. *Ann. Phys. (Leipzig)* 22 (1907), 749.

[16] RR Mehta and SF Vogel. “Sputtered cadmium oxide and indium oxide/tin oxide films as transparent electrodes to cadmium sulfide”. *Journal of The Electrochemical Society* 119.6 (1972), 752–756.

[17] Radhouane Bel Hadj Tahar et al. “Tin doped indium oxide thin films: Electrical properties”. *Journal of Applied Physics* 83.5 (1998), 2631–2645.

[18] Zhimeng Yu et al. “PEDOT: PSS films with metallic conductivity through a treatment with common organic solutions of organic salts and their application as a transparent electrode of polymer solar cells”. *ACS applied materials & interfaces* 8.18 (2016), 11629–11638.

[19] D. B. Fraser and H. D. Cook. “Highly Conductive, Transparent Films of Sputtered $In_{2-x}Sn_xO_{3-y}$”. *Journal of The Electrochemical Society* 119.10 (1972), 1368.

[20] G. Haacke. “New figure of merit for transparent conductors”. *Journal of Applied Physics* 47.9 (1976), 4086.

[21] Klaus Ellmer. “Past achievements and future challenges in the development of optically transparent electrodes”. *Nature Photonics* 6 (2012), 809–817.

[22] Vinod K. Jain and Arun P. Kulshreshtha. “Indium-Tin-Oxide transparent conducting coatings on silicon solar cells and their figure of merit”. *Solar Energy Materials* 4.2 (1981), 151–158.

[23] Roy G. Gordon. “Criteria for Choosing Transparent Conductors”. *MRS Bulletin* 25.08 (2000), 52.

[24] Arpun R. Nagaraja et al. “Experimental Characterization of a Theoretically Designed Candidate p-Type Transparent Conducting Oxide: Li-Doped Cr_2MnO_4”. *Chem. Mater.* 26.15 (2014), 4598.

[25] R Nagarajan et al. “p-Type conductivity in the delafossite structure”. *International Journal of Inorganic Materials* 3.3 (2001), 265.

[26] A.P. Young and C.M. Schwartz. “Electrical conductivity and thermoelectric power of Cu_2O”. *Journal of Physics and Chemistry of Solids* 30.2 (1969), 249–252.

[27] Y. Park et al. “Work function of indium tin oxide transparent conductor measured by photoelectron spectroscopy”. *Applied Physics Letters* 68.19 (1996), 2699.

[28] S. B. Zhang, S.-H. Wei, and Alex Zunger. “Intrinsic n-type versus p-type doping asymmetry and the defect physics of ZnO”. *Physical Review B* 63.7 (2001).

[29] CW Zhong et al. “Stability of High performance p-type SnO TFTs”. *Physical and Failure Analysis of Integrated Circuits (IPFA), 2015 IEEE 22nd International Symposium on the.* IEEE. 2015, 84–87.

[30] Renhuai Wei et al. “Facile chemical solution synthesis of p-type delafossite Ag-based transparent conducting $AgCrO_2$ films in an open condition”. *Journal of Materials Chemistry C* 5.8 (2017), 1885–1892.

[31] Atsushi Kudo et al. “$SrCu_2O_2$: a p-type conductive oxide with wide band gap”. *Applied Physics Letters* 73.2 (1998), 220–222.

[32] L. Farrell et al. “Conducting mechanism in the epitaxial p-type transparent conducting oxide Cr_2O_3:Mg”. *Phys. Rev. B* 91.12 (2015), 125202.

[33] Tadatsugu Minami. “New n-Type Transparent Conducting Oxides”. *MRS Bulletin* 25.08 (2000), 38.

[34] D.S. Ginley. *Handbook of Transparent Conductors.* 1st edn. Springer, 2010.

[35] Monica Morales-Masis et al. “Transparent Electrodes for Efficient Optoelectronics”. *Advanced Electronic Materials* 3.5 (2017).

[36] Michael L Chabinyc and Alberto Salleo. “Materials requirements and fabrication of active matrix arrays of organic thin-film transistors for displays”. *Chemistry of materials* 16.23 (2004), 4509–4521.

[37] Gordon Thomas. “Materials science: Invisible circuits”. *Nature* 389.6654 (1997), 907.

[38] Claes G. Granqvist. “Transparent conductors as solar energy materials: A panoramic review”. *Solar Energy Materials and Solar Cells* 91.17 (2007), 1529.

[39] Sandro Lattante. “Electron and hole transport layers: their use in inverted bulk heterojunction polymer solar cells”. *Electronics* 3.1 (2014), 132–164.

[40] Riccardo Po et al. “The role of buffer layers in polymer solar cells”. *Energy Environ. Sci.* 4.2 (2011), 285.

[41] Pingli Qin et al. “Organic solar cells with p-type amorphous chromium oxide thin film as hole-transporting layer”. *Thin Solid Films* 519.13 (2011), 4334.

[42] RL Anderson. “Germanium-gallium arsenide heterojunctions [letter to the editor]”. *IBM Journal of Research and Development* 4.3 (1960), 283–287.

[43] J. R. Waldrop. “Measurement of semiconductor heterojunction band discontinuities by x-ray photoemission spectroscopy”. *J. Vac. Sci. Technol. A* 3.3 (1985), 835.

[44] Marek Guziewicz et al. “Electrical and optical properties of NiO films deposited by magnetron sputtering.” *Optica Applicata* 41.2 (2011).

[45] H. Sato et al. “Transparent conducting p-type NiO thin films prepared by magnetron sputtering”. *Thin Solid Films* 236 (1993), 27.

[46] Hiroshi Kawazoe et al. “p-type electrical conduction in transparent thin films of $CuAlO_2$”. *Nature* 389 (1997), 939.

[47] Michael Snure and Ashutosh Tiwari. “$CuBO_2$ A p-type transparent oxide”. *Applied physics letters* 91.9 (2007), 092123.

[48] H Hiraga et al. “Excitonic characteristics in direct wide-band-gap $CuScO_2$ epitaxial thin films”. *Applied Physics Letters* 95.21 (2009), 211908.

[49] Takahisa Omata et al. “Wurtzite $CuGaO_2$: a new direct and narrow band gap oxide semiconductor applicable as a solar cell absorber”. *Journal of the American Chemical Society* 136.9 (2014), 3378–3381.

[50] M Younsi and S Manaa. “Synthesis and Characterization of Rich Delafossite $CuYO_{2+x}$ Application for Solar Energy Conversion”. *Energy Procedia* 36 (2013), 638–641.

[51] Roland Gillen and John Robertson. “Band structure calculations of $CuAlO_2$, $CuGaO_2$, $CuInO_2$, and $CuCrO_2$ by screened exchange”. *Physical Review B* 84.3 (2011), 035125.

[52] Yuhsuke Takahashi, Hiroaki Matsushita, and Akinori Katsui. “Synthesis and Characterization of Delafossite $CuLaO_2$ for Thermoelectric Application”. *Materials science forum.* Vol. 534. Trans Tech Publ. 2007, 1081–1084.

[53] Janet Tate et al. “Origin of p-type conduction in single-crystal $CuAlO_2$”. *Physical review B* 8.16 (2009), 165206.

[54] M O Sullivan et al. “Magnetoresistance of $CuCrO_2$ -based delafossite films”. *Journal of Physics: Conference Series* 200.5 (2010), 052021.

[55] T. Yokobori et al. “Electronic structure of the hole-doped delafossite oxides $CuCr_{1-x}Mg_xO_2$”. *Phys. Rev. B* 87.19 (2013), 195124.

[56] Kelvin H. L. Zhang et al. “Perovskite Sr-Doped $LaCrO_3$ as a New p-Type Transparent Conducting Oxide”. *Advanced Materials* (2015), 5191.

[57] T. Kamiya et al. “Electrical Properties and Structure of p-Type Amorphous Oxide Semiconductor $x.ZnO.Rh_2O_3$”. *Advanced Functional Materials* 15.6 (2005), 968.

[58] Elisabetta Arca et al. “Effect of Chemical Precursors On the Optical and Electrical Properties of p-Type Transparent Conducting Cr_2O_3:(Mg,N)”. *The Journal of Physical Chemistry C* 117.42 (2013), 21901–21907.

[59] Tiffany C Kaspar et al. “Defect compensation by Cr vacancies and oxygen interstitials in Ti^{4+}-doped Cr_2O_3 epitaxial thin films”. *Physical Review B* 94.15 (2016), 155409.

[60] Marius Grundmann et al. “Oxide bipolar electronics: materials, devices and circuits”. *Journal of Physics D: Applied Physics* 49.21 (2016), 213001.

[61] NF Quackenbush et al. “Origin of the bipolar doping behavior of SnO from X-ray spectroscopy and density functional theory”. *Chemistry of Materials* 25.15 (2013), 3114–3123.

[62] David P Norton et al. “ZnO: growth, doping & processing”. *Materials today* 7.6 (2004), 34–40.

[63] Sara Trost et al. “Room-temperature solution processed SnO_x as an electron extraction layer for inverted organic solar cells with superior thermal stability”. *Journal of Materials Chemistry* 22.32 (2012), 16224–16229.

[64] Toshio Kamiya and Hideo Hosono. “Electronic Structures and Device Applications of Transparent Oxide Semiconductors: What Is the Real Merit of Oxide Semiconductors?” *Int. J. Appl. Ceram. Technol.* 2.4 (2005), 285.

[65] S. Narushima et al. “A p-Type Amorphous Oxide Semiconductor and Room Temperature Fabrication of Amorphous Oxide p-n Heterojunction Diodes”. *Advanced Materials* 15.17 (2003), 1409.

[66] K Ueda et al. “Transparent p-type semiconductor: LaCuOS layered oxysulfide”. *Applied Physics Letters* 77.17 (2000), 2701–2703.

[67] Hidenori Hiramatsu et al. “Heavy hole doping of epitaxial thin films of a wide gap p-type semiconductor, LaCuOSe, and analysis of the effective mass”. *Applied physics letters* 91.1 (2007), 012104.

[68] David O Scanlon et al. “Understanding doping anomalies in degenerate p-type semiconductor LaCuOSe”. *Journal of Materials Chemistry C* 2.17 (2014), 3429–3438.

[69] Janet Tate et al. “Chalcogen-based transparent conductors”. *Thin Solid Films* 516.17 (2008), 5795–5799.

[70] Benjamin AD Williamson et al. “Engineering Valence Band Dispersion for High Mobility p-Type Semiconductors”. *Chemistry of Materials* 29.6 (2016), 2402–2413.

[71] Chang Yang et al. “Room-temperature synthesized copper iodide thin film as degenerate p-type transparent conductor with a boosted figure of merit”. *Proceedings of the National Academy of Sciences* 113.46 (2016), 12929–12933.

Chapter 3

Methodology

A material's intrinsic physical and electronic properties will govern it's applicability to a specific device. Hence, one focus of this thesis is to understand the electronic properties of two p-type Transparent Conducting Oxides (TCOs) using Resonant Photoemission Spectroscopy (RPES) and X-ray Photoemission Spectroscopy (XPS). The methodology of these spectroscopic techniques will be described in the following chapter. After, a suitable application has been identified often the device interface properties are not considered: a spectroscopic method will be utilised in this work to investigate the band alignment of p-type TCOs with other materials. The *p*-type materials grown for this thesis were all chromium based oxides grown with varying structures: nanocrystalline, polycrystalline and epitaxial. The deposition techniques for the growth of the TCO films will also be outlined. This will be followed by the various material characterisation techniques used in this work.

3.1 Photoelectron Spectroscopy

In 1916, Einstein was awarded the Nobel Prize in physics for the photoelectric effect. The photoelectric effect describes the emission of electrons or other free charge carriers when light is shone on a material. Electrons emitted in this manner are called photoelectrons.

Classical electromagnetic theory would expect that any alteration in the intensity of light would induce changes in the kinetic energy of the electrons emitted from the metal. While below a threshold intensity light source would show a time lag between the initial shining of its light and the subsequent emission of an electron. However, the experimental results did not produce either of the two predictions made by classical theory.

The only parameter that affected the emittance of electrons was the incident photons being above a threshold frequency. Below that threshold, no electrons are emitted from the material irrespective of the light intensity or the length of time of exposure to the light. To rationalise the fact that light can eject electrons even if the intensity of light is low, Einstein proposed that light is not a wave, but a collection of discrete wave packets (photons) each with a quantised energy. This linked with Max Planck's previous discovery of the relation ($E = hf$) linking energy (E) and frequency (f) based on the quantization of energy. The factor h is named the Planck constant.

This led Siegbhan to develop a new experimental technique based on photoemission of electrons to study the electronic structure of materials [1]. When a light beam is directed to the sample surface the energy of the photon is adsorbed by an electron within an atom, causing the subsequent emission of that electron. The emitted electron is referred to as a photoelectron. To emit core electrons you need to have a threshold photon energy which will lie in the x-ray regime. This technique is named X-ray Photoelectron Spectroscopy (XPS). If the photon energy is in the ultraviolet spectral range, the technique is called Ultraviolet Photoelectron Spectroscopy (UPS). However, UPS is limited to studying valence band electrons but with much higher energy resolution. The photoelectron ejected has a kinetic energy (E_{KE}) that is related to it's binding energy (E_{BE}) by the following formula:

$$E_{\mathrm{BE}} = h\nu - E_{\mathrm{KE}} \tag{3.1}$$

where the binding energy is the energy required to liberate an electron from an atom, molecule or material. These two quantities, the incident photon energy and kinetic energy of the emitted electron should be all that is needed to find the binding energy. However, the sample is contacted to the spectrometer. As the fermi level of the sample aligns with the spectrometer the above equation should now be modified to:

$$E_{\mathrm{BE}} = h\nu - E_{\mathrm{KE}} - \phi_{\mathrm{spec}} \tag{3.2}$$

where ϕ_{spec} is the work function of the detector. Without this assumption it would be necessary to have knowledge of the work function of any sample being analysed by photoelectron spectroscopy. However in any photoemission experiment, the basic excitation process involves the absorption of a photon of energy. The absorption of a photon ($h\nu$) interacts with an N-electron system which has an initial wavefunction Ψ_{is}(N) with a total energy of the system given by E_{is}(N) and produces a final state wavefunction described by Ψ_{fs}(N-1). The conservation of energy stipulates that:

$$E_{\mathrm{is}}(N) + h\nu = E_{\mathrm{fs}}(N-1,k) + E_{\mathrm{kin}} \tag{3.3}$$

k denotes the initial energy level of the photoelectron. Koopman's theorem (Equation 3.4) assumes the simplest case, that the binding energy (E_{BE}) of the electron will be the negative value of the energy of the respective electron's one electron orbital energy [2]:

$$E^{v}_{\mathrm{BE}}(k) = E_{\mathrm{fs}}(N-1,k) - E_{\mathrm{is}}(N) = -\epsilon_k \tag{3.4}$$

where $-\epsilon_k$ is equal to the negative of the orbital energy of the electron liberated by the photoemission process. This is assumed, in Koopman's theorem, to be equal to the binding energy of the electron. In practice to calculate the binding energy of a emission line in a spectra: a sum rule can be derived which averages the binding energy of all peaks associated with primary excitation of one core level, multiplied by their intensities I_k. This includes satellite features such as shake up peaks [3]. The shake up peak appears at energies characteristic of the excited states for an element with respect to the state measured by the zero loss intensity. Some of the photon energy is used to excite the ion out of the zero loss state whilst at the same instant ejecting the photoelectron with the remaining photon energy. Similarly, shake-off events, where more than one electron is ejected at the time of photo-ionization, may result in broad structures to high binding energies in a spectrum [4].

If Koopman's were to hold true the binding energy, ϵ_k would be equal to the centroid of the spectral peak region:

$$-\epsilon_k = \frac{\Sigma_k I_k E^v_{\mathrm{BE}}(k)}{\Sigma_k I_k} \tag{3.5}$$

This assumes the one electron orbital is unaffected by the photoabsorption process. In reality, this does not describe the situation. Orbital relaxation and electron-electron correlation are added as correction terms:

$$E^v_{\mathrm{BE}}(k) = -\epsilon_k + \Delta\epsilon_{\mathrm{relax}} + \Delta\epsilon_{\mathrm{correlation}} \tag{3.6}$$

due to the fact that Koopman's theorem assumes that the photoabsoprtion process is instantaneous and no changes in core levels can occur on this time scale. This assumption is often not correct and is accounted for in the orbital relaxation ($\Delta\epsilon_{\mathrm{relax}}$) term. The $\Delta\epsilon_{\mathrm{correlation}}$ term deals with the collective electron-electron interactions in the material which is also neglected in Koopman's theorem. It is very important in Mott-Hubbard insulators of which Cr_2O_3 is one. A Mott Hubbard insulator is a class of material that should conduct electricity under conventional band theories bu alas is an insulator due to electron-electron interations [5]. Inclusion of the relaxation correction term into the calculations lowers the core-level binding energy and gives better agreement with experimental data.

However, even the relaxation and correlation corrections to the Koopman approximation only treats the final state of the atom, which is not necessarily true. The initial states are treated by the sudden approximation assuming that the photoabsorption process is rapid. Therefore the other (N-1) electrons emerge from the photoabsorption process with the same final and initial states [3].

In theory a photoemission spectra consists of sharp peaks which experience broadening due to their finite lifetime. Heisenberg's uncertainty principle dictates a certain amount of minimum broadening. This finite lifetime of the core excited system is given by a Lorentzian distribution [6]: the core hole lifetime as well as the instrumental resolution will further broaden spectra. The instrumental broadening is typically described by a Gaussian distribution. The measured peak width (E_m^2) will be convolution of all of these broadening effects:

$$E_m^2 = E_x^2 + E_n^2 + E_a^2 \tag{3.7}$$

where E_x^2 is the width of the photon line, E_n^2 is the natural line energy distribution of electrons at that energy level and E_a^2 is the energy resolution of the analyser [4].

3.1.1 Scientia Omicron Photoelectron Spectrometer

Laboratory XPS measurements were carried out on a Scienta Omicron Multiprobe XP system (see figure 3.1) with a concentric hemispherical (EA125) analyser. The x-ray source is composed of a thoriated tungsten filament which emits electrons, accelerated by a high voltage typically 10 - 15 kV, which are directed at an anode. The anode, in our case, is composed of aluminium. By bombarding the anode with high kinetic energy electrons emitted from the tungsten filament, producing x-rays lines. The x-rays are monochromated by a quartz crystal x-ray mirror that, by using Braggs' law, selects the Kα line at 1486.67 eV. The x-ray mirror also absorbs unwanted radiation. The XPS system is equipped with three chambers: load lock, analysis and preparation. The load-lock allows quick entry of samples into the system. The preparation chamber is equipped with a

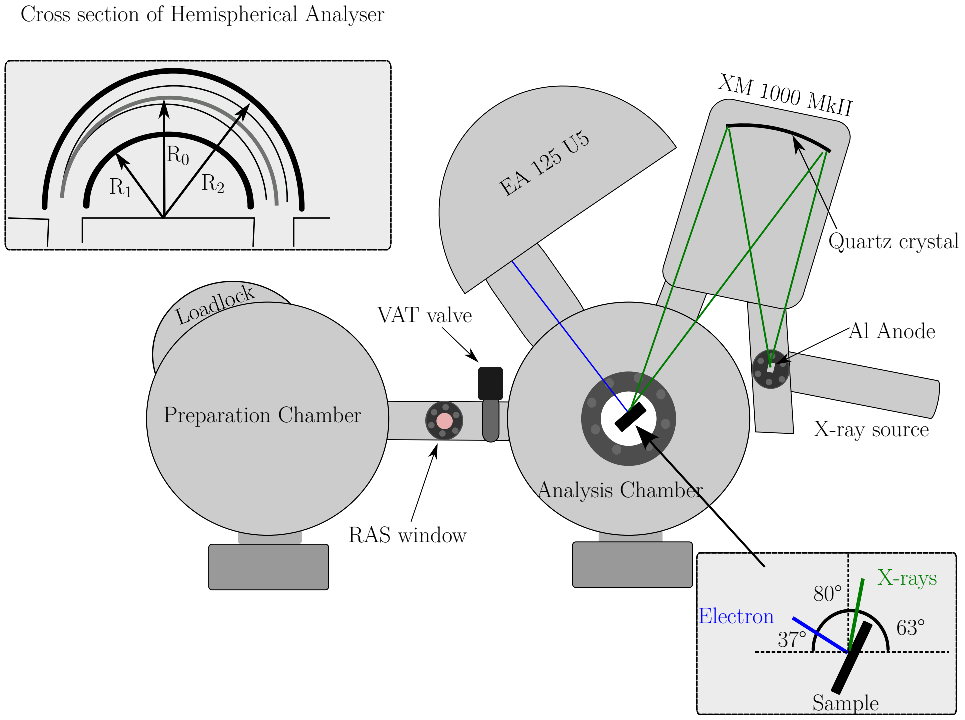

Figure 3.1: Schematic of the Scientia Omicron Multiprobe XP: Analysis chamber has an Ultra-Violet lamp (HIS 12 VUV source) mounted but not pictured. Bottom right inset illustrates how the sample is orientated within the analysis chamber. Top left inset shows a cross section of the electron's path through the hemispherical analyser

4-grid SPECTA Low Energy Electron Diffractometer (LEED) with a thoriated tungsten filament and ISE 5 sputtering source, fitting with an argon gas line, for sample preparation. A Mini Electron Cyclotron Resonance (ECR) Plasma Source is fitted to the preparation chamber which can be used for reactive sputtering, oxide growth and oxygen cleaning. A strain relieved window is fitted onto the XPS preparation chamber that allows *in-situ* optical measurements to be made.

Ultraviolet Photoelectron Spectroscopy

Ultraviolet Photoelectron Spectroscopy (UPS) was originally designed to analyse the photoelectron spectra of free molecules in a gaseous phase. It is composed of a photon source from a discharge lamp, most commonly helium filled, which illuminates the sample [He I $h\nu = 21.2$ eV, and He II $h\nu = 40.8$ eV]. UPS is limited to the valence band spectral region due to it's low energy photon source but achieves much higher resolution that XPS cannot match. The improved resolution of UPS is due to the very narrow line width of the Helium I (≈ 0.006) and larger photon flux, which allows operation of the analyser at lower pass energies. The analysis chamber is fitted with an HIS 13 VUV source.

Due to the improved resolution of UPS the secondary cut off is sharper than with XPS meaning it can be determined with a smaller error. As a result work function measurements are most commonly made by UPS instead of XPS. The analysis chamber is fitted with a mu-metal lining which screens stray magnetic fields that induce changes in the kinetic energy of the low energy photoelectrons produced in UPS.

Photoelectron Analyser

The photoelectron analyser is composed of two concentric hemispheres with a path that can be traced between the two hemispheres of radius R_0. The outer hemisphere has a negative potential and conversely the inner side is positive. An average potential, V, exists between the outer and inner hemisphere. The placement of the entrance and exit analyser slits is along R_0. An electron travelling inside the analyser is subject to a centripetal electrostatic force, F_{ce} and a centrifugal, F_c force equal to:

$$F_{ce} = \frac{eV}{\left(\frac{1}{R_{\text{inner}}} - \frac{1}{R_{\text{outer}}}\right) R_0^2} \tag{3.8}$$

$$F_c = \frac{E_{\text{kinetic}}}{R_0^2} \tag{3.9}$$

The average potential difference between the two analysers is V and R_0 is the path of the electron through the analyser. The two forces, Equations 3.9 & 3.8 can be equated:

$$E_{\text{KE}} = \frac{e\Delta V}{\left(\frac{R_{\text{outer}}}{R_{\text{inner}}} - \frac{R_{\text{inner}}}{R_{\text{outer}}}\right)} = E_{\text{pass}} \tag{3.10}$$

The photoelectrons pass through a double lens system which focuses the electrons before they are decelerated with a defined voltage, determined by the specified pass energy. The acceptance angle, magnification and analysis area is selected by this first lens (an Einzel lens). As no change the electron energy occurs it can apply a constant magnification throughout the kinetic energy regime. The second lens changes the electrons energy to match the pass energy of the analyser. At the second lens stage the photo-electrons encounter an aperture, which focuses them onto the entrance slit and into the analyser [7].

The electron analyser was used in Constant Analyser Energy (CAE) mode: the analyser pass energy is held constant while the retarding voltage is changed thus scanning the range of kinetic energy specified. In this mode the resolution remains constant through the kinetic energy regime. However, the sample area and emission angle may vary across the kinetic energy range.

The energy resolution of the instrument (0.58 eV) is significantly larger than the natural line width of the Ag $3d_{5/2}$ peak from pure silver (0.33 eV) [8]. Therefore, the analyser resolution is calculated by measuring a silver (110) crystal using the Ag $3d_{5/2}$ peak. The silver crystal was cleaned by sputtering with argon ions and annealed at 737 K. The absolute energy scale of the XPS was also calibrated by ensuring the binding energy of 0 eV coincided with the Fermi edge of the silver crystal.

3.1.2 Spectral Acquisition

Laboratory XP spectra were acquired with the Omicron software EIS spectra. High resolution XP spectra were taken a pass energy of 20 eV, a slit width of 6 mm which is the effective slit width of both the entrance and exit slits in the dispersive direction. The step size of each scan was (0.05 eV). The dwell time varied depending on the integration time needed to obtain an adequate signal to noise ratio for a specific core level.

For UP spectra the pass energy was reduced further to 5 eV, slit width of 1 mm

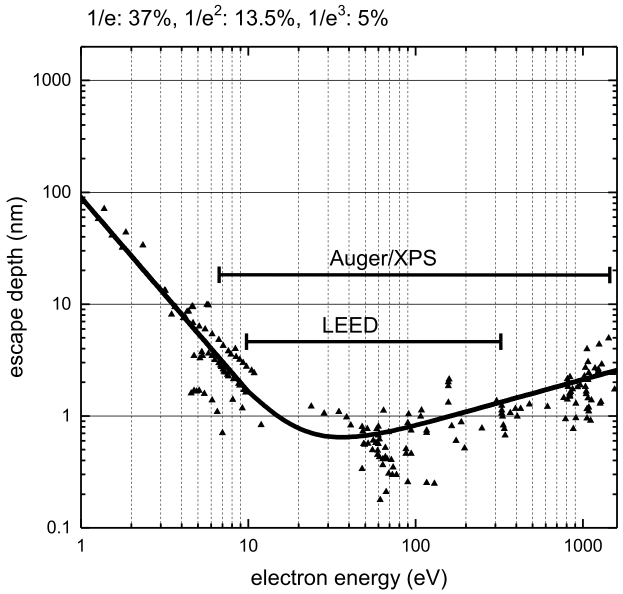

Figure 3.2: Experimental values for the minimum distance an electron can travel before undergoing an inelastic collision. This value varies as function of the electron's kinetic energy [9]

and step size 0.01 eV. All spectra were analysed with the Casa XPS program.

3.1.3 Quantification of Atomic Concentrations

Semi-quantitative analysis of the relative concentration of different elements in a material can be achieved by comparing the intensity of the relevant core level peaks. In this thesis, XPS was used to measure the doping concentration of Cu_xCrO_2 and $Cr_{2-x}Mg_xO_3$ films.

There are a number of factors that must be taken into account in order to accurately reflect the chemical composition using XPS peak intensities. In order to quantify the stoichiometry it must be assumed that the surface of a sample is homogeneous, as if the composition perpendicular to the surface within the sampling depth of the XPS is non uniform the elemental ratio cannot be defined. This is unlikely to be the case for MBE films grown at deposition temperatures of greater than 600 K. However, there may be a larger error expected with spray pyrolysis samples or deposition at room temperature.

The relative binding energies of any core level peaks being compared have to be taken into account. The electron inelastic mean free path (see figure 3.2) strongly depends on the kinetic energy. To minimise error, the core level peaks being compared should be as close as possible in binding energy. For example when quantifying the doping of $Cr_{2-x}Mg_xO_3$ the most intense peaks are the Mg 1s and Cr 2p core levels. However, the doping ratio was measured using the Mg 2s and Cr 3s as these peaks were separated by only 10 eV [9].

Other factors that have to be considered are the photo-ionisation cross-section of that core level and finally the transmission function of the analyser which determines the sensitivity of the analyser to electrons of that kinetic energy. These criteria form the basis for the Relative Sensitivity Factor (RSF) that is unique for a specific elemental core level. Using the RSF and peak area one can determine the chemical composition of a sample [**Matthew2004**].

3.2 Energy Band Alignment

A common means to describe and understand the functionality of electronic devices is the energy band diagram, in which the valence and conduction band energies are drawn as a function of position. Within this thesis photoelectron spectroscopy was used to study the formation of the interface that $Cr_{2-x}Mg_xO_3$ films made with other n-type TCOs, thereby mapping the energy band diagram of $Cr_{2-x}Mg_xO_3$ in contact with oxides. Such an experimental technique to study the energy band alignment of an interface is necessary instead of the alignment predicted using Anderson's rule [10] as it fails to predict the real alignment at the interface of two oxides. Anderson's rule is also referred to as the electron affinity rule, and is closely related to the Schottky-Mott rule for metal-semiconductor junctions [11]. Anderson's rule states that when constructing an energy band diagram, the vacuum levels of the two semiconductors on either side of the heterojunction should be aligned. The difference in two vacuum levels gives the predicted built in potential at the interface. This rule can work well for organic/inorganic interfaces but fails to predict actual band offsets in semiconductor heterojunctions [12]. Anderson's rule ignores chemical bonding that occurs with small or no vacuum separation. Interfaces states may have a large electrical polarisation or defect states/dislocations may occur at the interface. Additional complexities such as interfaces of two polycrystalline materials or different crystal structures and/or lattice constants will complicate the situation further. To date, no general model is developed to align two oxide surfaces [13].

Ultra-violet Photoelectron Spectroscopy (UPS) can provide detailed information on the valence band of a surface. Valence electrons play a role in chemical bonding and are detected when photo-emitted with a binding energy of greater than 20 eV. Figure 3.3 outlines the information that can be gathered from one valence band spectrum: the bulk energy band diagram of a material can be deduced from a UP spectrum combined with a direct measurement or literature value for the fundamental band gap. The quantity that is most useful is, E_f - E_{VBM}, the distance between the Fermi level and the valence band: a common Fermi level exists for two materials in contact and gives us a common point in the energy scale to relate energetic changes in the *n* and *p* type films of a junction.

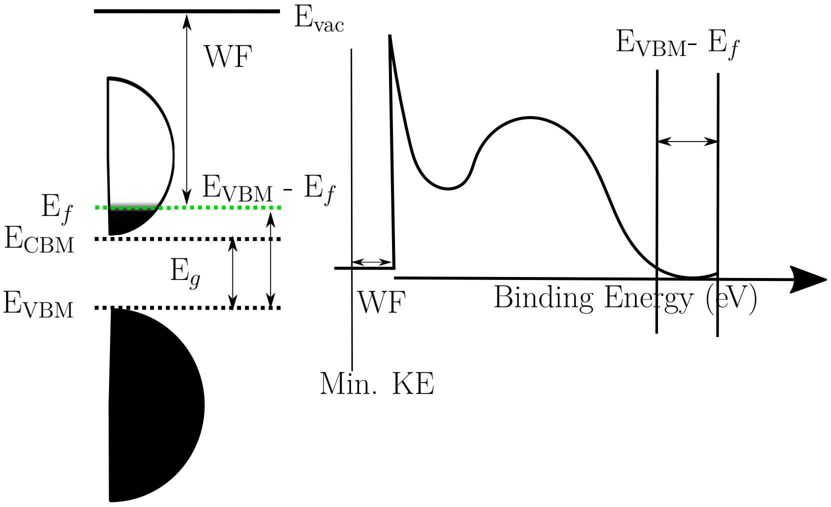

Figure 3.3: Electronic band structure and UPS spectrum. WF, E_g, E_{vac}, E_{CBM}, E_{VBM}, and E_f denote work function, band gap, vacuum level, conduction band minimum, valence band maximum, and Fermi level respectively

Photoemission experiments are a surface sensitive technique for solids. Only elastically scattered electrons from the sample carry direct information about the

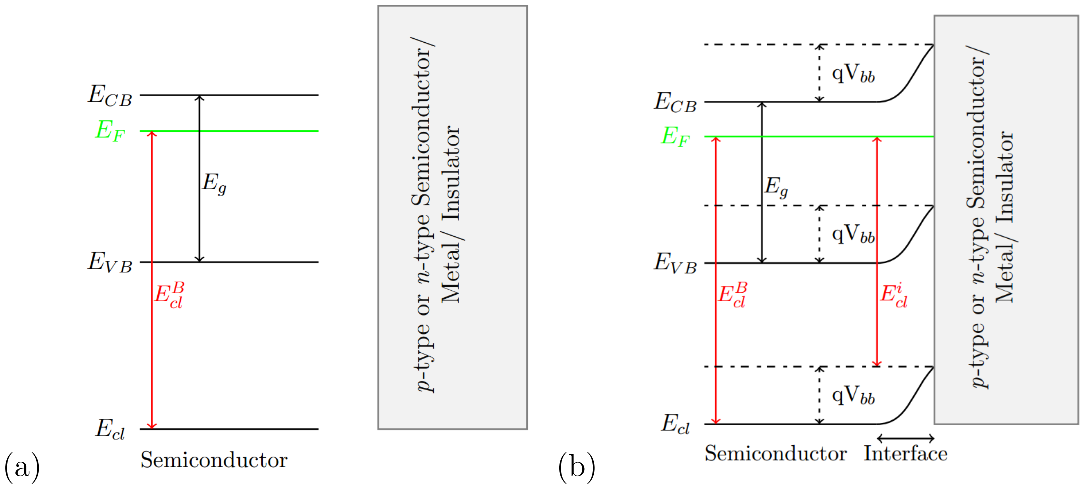

Figure 3.4: Schematic outlining the basic band alignment concept, E_{CB} = conduction band minimum, E_{VB} = Valence band maximum, E_g = Fundamental Band Gap, E_f = Fermi Energy, E_{cl} = Core level binding energy, E^B_{cl} = Core level binding energy referenced from the Fermi level E_{cl} = Core level binding energy at the interface, qV_{bb} = Built in potential at the interface (a) outlines the band structure of a n-type conductor (left) (b) Post contact the creation of a common fermi level by the transfer of charge creates a change in the position of the valence and conduction bands across the interface.

electronic structure. The average distance of an electron to undergo no inelastic scattering is given by the mean free path [9]. As seen in figure 3.2 the inelastic mean free path varies with elemental composition and the kinetic energy of the electron leaving the sample.

Therefore it is possible to design an experiment to probe just the interface properties. The interface is formed by depositing one material upon another. Precise control over the film thickness is need to probe the energy band alignment of an interface in this manner. As the interface is grown information about the relative positions of the valence band of the substrate and the deposited film can be directly obtained from the superposition of the valence bands [14]. This has been previously done for group III-V semiconductor interfaces extensively [15]. This method can be improved upon by taking core-level and valence-band photoelectron spectroscopy for the surfaces of interest. Core levels electrons are contained within atomic orbitals that do not participate in bonding. Any built in potential, $V_{\text{built-in}}$, created due to the interface of pn junction should affect the kinetic energy of the core electrons emitted. The changes in kinetic energy of the core level electrons can then give you the magnitude of the energetic change in position of the conduction and valence bands at the interface. The binding energy of a core level in a film and valence band maximum share a common reference point, the Fermi energy. The binding energy of the core levels can be related to changes in the valence band maximum by measuring the core level and valence band maximum offset for the bulk film ($E_{\mathrm{cl}} - E_{\mathrm{VBM}}$) [14, 16].

Figure 3.4 illustrates the evolution of the valence band energetic position, E_v, across the interface. It highlights how changes in the binding energy of a core level, E_{cl}, can be related to changes in E_{VBM}. Since the valence band and conduction band are related by the band gap (E_g), once E_{VBM} is mapped likewise E_{CBM} can be mapped. This assumes the band gap isn't altered at low thicknesses. Along with the work function measurements from UPS, the entire energy band diagram can be mapped.

3.3 X-ray Absorption Spectroscopy

XPS involves analysing the emission of electrons after x-ray excitation. However, another powerful spectroscopic tool is to measure the absorption of x-rays. X-ray Absorption Spectroscopy (XAS) is a a widely used technique for determining local coordination, geometry and electronic structure of materials. XAS is carried out experimentally by selecting photon energies near at and above the threshold of promoting a core electron. The absorption threshold is determined by the transition probability given by Fermi's Golden Rule [17]:

$$\mu \propto |\left\langle \mathrm{final} \right| H^{'} \left| \mathrm{initial} \right\rangle|^2 \Phi \propto |M|^2 \Phi \tag{3.11}$$

where M is the matrix element of the perturbation between the final and initial state, and Φ is the unoccupied density of states (DOS). The matrix element is non zero if the orbital quantum number differs by 1 from the initial state ($\left| \mathrm{initial} \right\rangle$) and the spin is conserved. The absorption edge is named based on the core electron

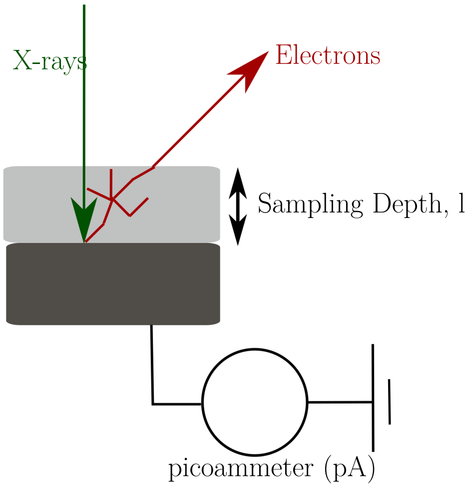

Figure 3.5: Total electron yield x-ray absorption spectroscopic detection method

being promoted. The principle quantum numbers n=1, 2 and 3 are called the K, L and M edges. The excitation from a $2s$ or $2p$ orbital will be an L edge [18].

3.3.1 Total Electron Yield

Instead of directly measuring the absorbed x-rays, the electrons (photo, secondary and Auger electrons), created by the absorbed x-rays through excitations of core electrons to unoccupied states above the Fermi level, are detected. The decay of electrons from these unstable states results in the emission of a photon of energy equivalent to the energy difference between the core level and excited state. The Total Electron Yield (TEY) cascade involves several scattering events and originates from an average depth, the electron sampling depth, l [18]. The XAS intensity for TEY is:

$$I_e = I_0 \mu l \tag{3.12}$$

I_e/I_0 is the net current flowing into the sample required to neutralize the charge resulting from the emission of electrons: constituting the TEY measurement. The electron sample depth is governed by the mean free path of electrons, figure 3.2, which makes the TEY measurements surface sensitive.

XAS measures the unoccupied density of states and is both element and site specific. XAS measurements can distinguish between the different binding energies of specific elements, as well as different bonding sites for the same element. Within this work, XAS will be used to analyse whether magnesium doping of Cr_2O_3 affects the local coordination and bonding of the Cr_2O_3 lattice. It will be used in a similar manner to probe copper deficient Cu_xCrO_2 films, by varying the copper concentration within the films it is hoped the changes in the electronic structure can be observed in the Cu and Cr L edges.

3.4 Resonant Photoemission Spectroscopy

The conductivity of a p-type TCO is governed by the valence band electronic structure. The valence electrons occupy states within the band structure which can be probed by taking valence band spectra using photoemission or optical spectroscopy. The absorption of a photon by a valence electron in a material and the subsequent emission of that electron is called the direct photoemission process and probes the occupied states within a valence band (see figure 3.6 (b)). However, for p-type TCO materials the interest is in studying the unoccupied states within the valence band and also the element within the valence band that these unoccupied states are associated with.

An experimental method of identifying the elemental character of certain features in the valence band spectra is to employ Resonant Photoemission Spectroscopy (RPES). Photoemission resonance, like XAS, starts with the promotion of an electron from a core level (of energy E_{cl}) to an unoccupied state (of energy E_u). The creation of a core hole (of energy E_c) by the absorption process results in the emission of an Auger electron from the valence band. This two step process is outlined below [17]:

$$E_{\mathrm{cl}} \xrightarrow{\mathrm{XAS}} E_u - E_c \xrightarrow{\mathrm{AE}} E_{\mathrm{KE}} - E_{\mathrm{VB}} \tag{3.13}$$

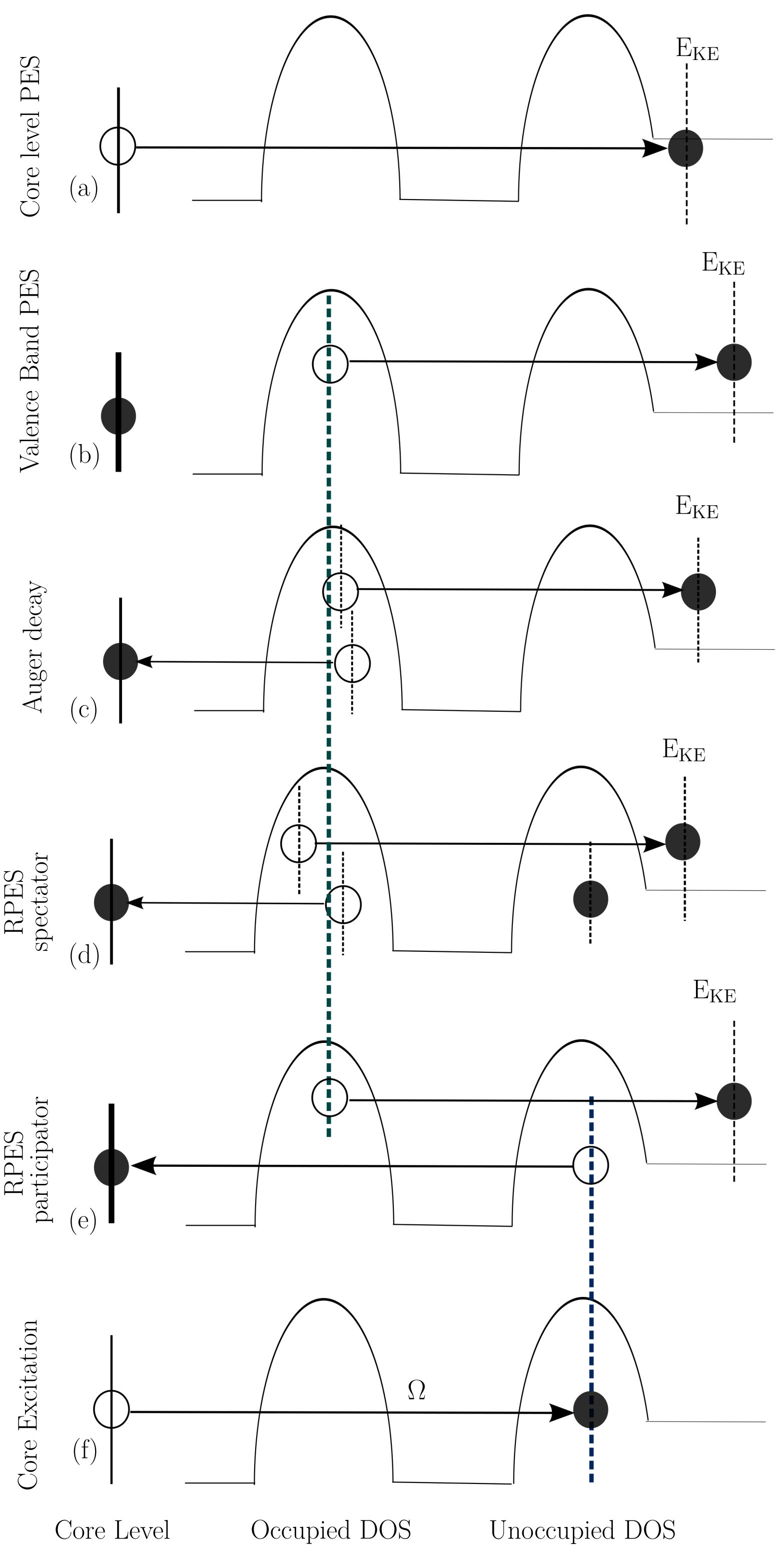

Figure 3.6: (a) Core level photoemission, (b) Valence band photoemission, (c) Auger Emission, (d) Resonant photoemission where the excited core electron participates in the decay. This yields a final state that is identical to the final state in a normal valence band photoemission experiment ,(e) Spectator decay is shown where the originally excited electron spectates the Auger decay of another electron from the occupied levels, (f) Core level excitation process to the empty Density Of States (DOS).

where AE denotes the emission of an Auger Electron. As the initial absorption process requires some unoccupied states within the valence band, RPES can directly probe the position of holes in our p-type oxide films. The initial absorption process is also governed by selection rules allowing us to gather information on not just the position of holes within the valence band, but also which elemental state, e.g., Cr 3*d* or Cu 3*d* the charge carriers are associated with.

Practically, RPES is carried out by varying the incident photon energy across a particular absorption edge. As the RPES process leads to the same final state as the direct photoemission of valence electrons it increases the intensity of a spectral feature within the valence band (see figure 3.6) [17]. Observation of photoemission resonances imply the presence of localized holes, hence it will be used in this thesis to study the electronic structure of $Cr_{2-x}Mg_xO_3$ and Cu_xCrO_2 p-type oxides [19].

3.5 Synchrotron Radiation

The techniques of XAS and RPES require access to a range of photon energies which is beyond the fixed photon energy available in a laboratory XPS. To accommodate these experiments, large cyclic particle accelerators have been built to accelerate an electron around a fixed closed loop path called synchrotron. Synchrotron radiation is emitted when charged particles (electrons) moving at relativistic speeds change momentum. Electrons will radiate electromagnetic radiation in a narrow beam in the direction that they were travelling. The electromagnetic radiation emitted will be a wide spectrum spanning the microwave to hard x-ray regime. It has been employed by spectroscopists as a useful tool. The first synchrotron source was opened in 1981 in England [20]. Third generation synchrotron sources are the most common currently available sources for spectroscopic studies of which MAX II, contained within MAX-lab, is one [21].

D1011 beamline

X-ray Absorption Spectroscopy (XAS), X-ray Photoemission Spectroscopy (XPS) and Resonant Photoemission Spectroscopy (RPES) were carried out at the D1011 beamline, MAX II, MAX-lab, Sweden. Beamline D1011 is situated off a bending magnet covering the energy range 30 to 1500 eV. The monochromator is a modified SX-700 monochromator (1220 l/mm gratings) with plane-elliptical focusing mirror [22]. Two experimental stations are available off the beamline D1011, both designed for spectroscopy. The front end-station contains a Scienta SES-200 hemispherical electron spectrometer and a Microchannel Plate Detector (MCP), for total electron yield x-ray absorption measurements. There is no refocusing optics after the exit slit of the beamline and the front chamber. This creates a large illumination spot size of 2 mm in diameter. The exit slit governs the energy resolution of the beamline. The back endstation allows magnetic measurements like X-ray Magnetic Circular Dichroism (XMCD) and XAS. However, all XAS measurements contained within this work were taken on the front endstation due to the reference total yield mesh on the back station containing some chromium metal, interfering with measurements on chromium oxides.

All photoemission spectra were normalised by the ring current. The valence band spectra at photon energies of 40-100 eV were taken with a photon flux between 10^{11}-10^{12} ph/s incident on the sample. The binding energies in valence band spectra were aligned to the Fermi edge taken of a piece of tantalum foil in contact with the sample.

All absorption spectra were taken in Total Electron Yield (TEY) mode by measuring the drain current as a function of incident photon energy. The beam line transfer function was measured by a reference total electron yield measurement on a clean gold mesh.

Deposition Techniques

The deposition techniques which the materials studied within this work were synthesised by will be outlined below.

3.6 Molecular Beam Epitaxy

Epitaxy refers to the growth of a crystalline overlayer upon a lattice matched substrate. Molecular Beam Epitaxy (MBE) is a deposition method that produces highly crystalline thin films. The growth occurs by a process of two or more thermal molecular beams directed towards a crystalline substrate under High/Ultra-High Vacuum [23]. The molecules land on the crystalline substrate surface, condense and build up systematically to create thin films of material.

The MBE system used to grow samples for this work is manufactured by DCA Instruments (model M600), see figure 3.7 for a detailed schematic of the chamber. The system consists of two chambers separated by a gate valve. The smaller chamber operates at a typical pressure of 7×10^{-5} Pa is used for loading the samples into the main chamber (9×10^{-7} Pa operating pressure). This chamber contains a transfer arm with a specially designed transfer cup. The samples are held by a custom design sample holder. The vacuum of the MBE is maintained by oil-free turbomolecular and scroll pumps. The main chamber, see figure 3.7, contains a four pocket e-beam evaporator and a separate single pocket e-beam evaporator allowing for co-deposition. Each evaporation source has a pneumatically controlled shutter to allow precise stopping and starting of layer growth. There is also a pneumatically controlled main shutter to shield the substrate from all evaporation sources simultaneously. An INFICON IC/5 deposition rate controller is used in conjunction with quartz crystal balances to montior the growth rate for the e-beam evaporator. The temperature of the sample holder is controlled by a EUROTHERM 2408 controller used in conjunction with a direct-current (DC) power supply and a C-type thermocouple (W/Rh).

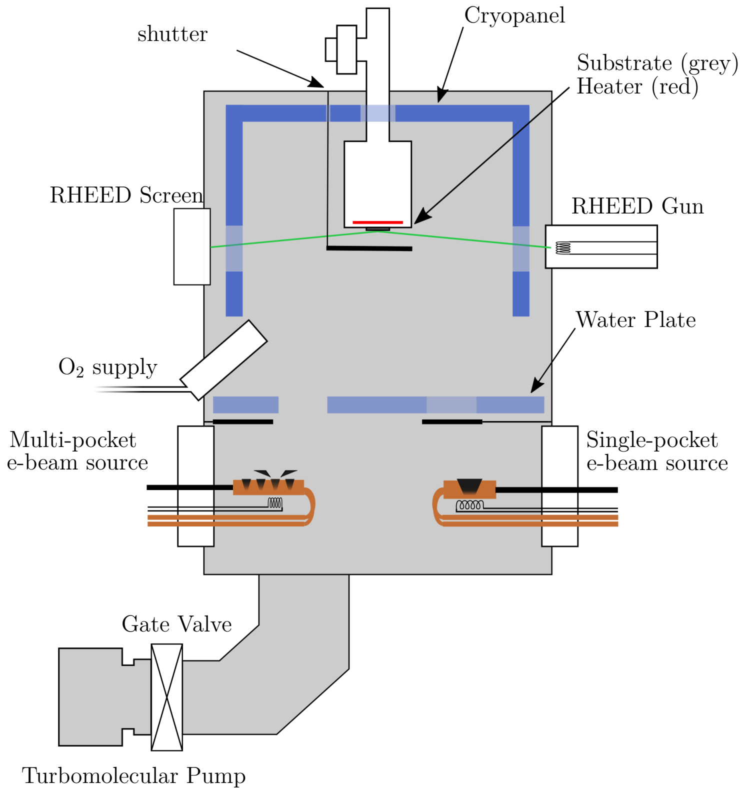

Figure 3.7: Schematic of DCA Instruments Molecular Beam Epitaxy (MBE) chamber, model number M600

The heater is a Pyrolytic Boron Nitride (PBN) and Pyrolytic Graphite (PG) heater element (PBN/PG/PBN).

During growth of oxides it is necessary to introduce an oxygen partial pressure. This is done by using a leak valve attached to the main chamber. To induce greater reactivity during oxide growth an Oxford Scientific OSPrey Plasma Source is used to generate atomic oxygen. This is called plasma assisted molecular beam epitaxy.

Growth of Cr_2O_3 and $Cr_{2-x}Mg_xO_3$

Cr_2O_3 pieces were e-beam evaporated at an oxygen partial pressure 6×10^{-3} Pa with the substrate temperature maintained at 723 K. The growth rate was approximately 0.2 Å/s. The doping was achieved by controlling the supplied power to a second e-beam evaporator loaded with MgO. The materials used in this study for the growth were Cr_2O_3 (99.9 % purity) and MgO pellets (99.95 %) supplied by Kurt J. Lesker. The crystal monitors are calibrated by cross-checking the actual

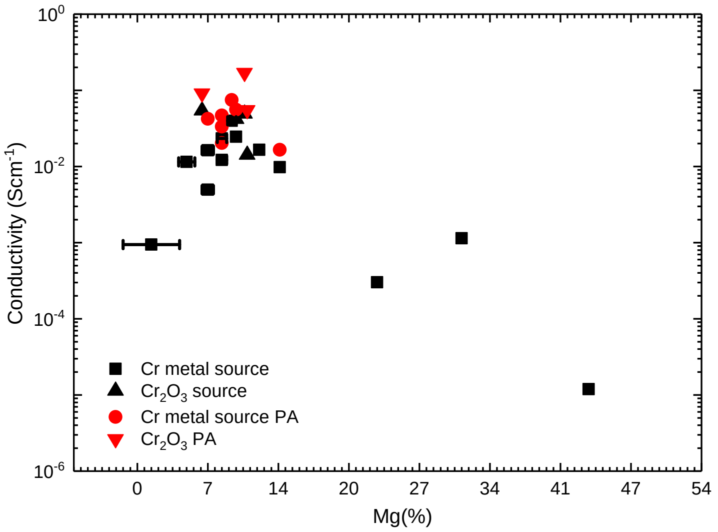

Figure 3.8: Conductivity vs magnesium concentration incoporated into the Cr_2O_3 lattice. Square symbols (■) represent samples grown from chromium metal source while triangles (▲) indicate those grown from the ceramic chromium oxide source. Circles (●) indicate chromium metal source samples post-annealed and inverted triangles (▼) are post-annealed samples grown from the ceramic chromium oxide source.

thickness of the deposited film by x-ray reflectivity (Section 3.10).

$Cr_{2-x}Mg_xO_3$ films could be grown immediately as optimum doping of the Cr_2O_3 lattice had already been developed for the MBE system [24]. Figure 3.8 shows the optimum conductivity of $Cr_{2-x}Mg_xO_3$ to be between 8-10 % magnesium doping. All concentrations in figure 3.8 were measured via x-ray photoelectron spectroscopy *ex-situ*.

3.7 Magnetron Sputtering

MBE produces thin films of high quality crystalline material with precise control over the thickness. These films are useful for fundamental studies of the basic properties of p-type TCOs. Other more industrially relevant deposition techniques have been explored also.

Magnetron sputtering has become the process of choice for the deposition of ITO and a wide range of other industrial material coatings. In the basic sputtering process a cathode (metal/ceramic target composed of the desired deposition material) is bombarded by ions. The anode is the chamber body, which includes the sample. These ions are generated in a discharge plasma in front of the cathode. The bombardment process causes the removal or sputtering of target atoms, which may then condense into a thin film upon a substrate. Secondary electrons are also emitted from the target surface as a result of the ion bombardment; these electrons play an important role in sustaining the plasma. The magnetron assistes the plasma discharge by making use of the fact that a magnetic field configured parallel to the target surface can constrain the motion of secondary electrons to the vicinity of the target.

The magnetron sputtering system has both Direct Current (DC) and Radio Frequency (RF) mode available. DC sputtering operates on the principle that the cathode attracts cations (positive ions) from the plasma, while the anode attracts anions (the electrons). Two relatively high-field regions, the sheaths, separate the plasma body from the anode and the cathode. If an insulating target is required for a specific material growth a DC discharge would be unsustainable as no current can flow through a dielectric, so you get a build up of ions at the surface of the target which hinder the sputtering process.

RF sputtering operates by applying a RF voltage, as the alternating applied voltage changes sign the current density to the electrode alternates between J_{ion} (ion bombardment) and -qz (electron bombardment). The effect of the applied voltage and current density at the cathode is illustrated in figure 3.9 (a) and (b). However, the net current averaged over one period is not equal to zero as there is a disparity in the mobilities of ions versus electrons. In order to achieve zero net current over each RF cycle blocking capacitor self-biases because of the negative charge accumulating. This creates a secondary DC field which offsets the applied AC field. This is illustrated in figure 3.9 (c) and (d). The discharge time for the capacitor leads to an extended ion bombardment period, where sputtering of the target occurs, followed by electron bombardment for a short time but at with a high current during which the external blocking capacitor is self-biased again [25].

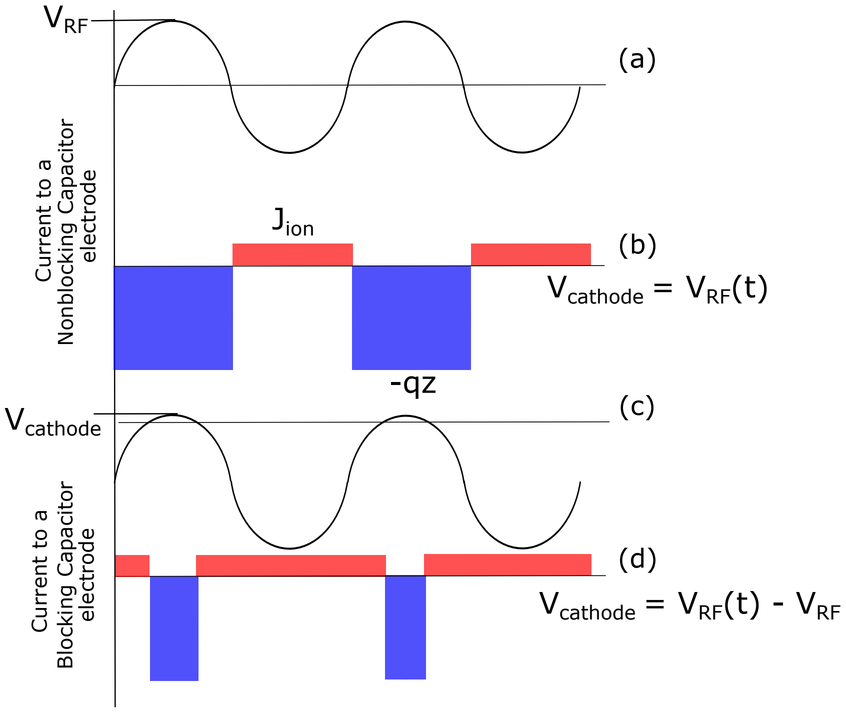

Figure 3.9: Radio frequency discharge model in magnetron sputtering

3.7.1 Deposition Chamber

A schematic of the chamber used in this thesis is given in figure 3.10. The magnetrons in this system are manufactured by AJA International and contain a fixed balanced magnetic array. The balanced magnetic array strongly confines the plasma to the target region giving lower deposition rates than an unbalanced magnetron. It would be difficult to deposit over large areas with uniform density using a balanced magnetic array but for small area deposition this configuration suffices [26].

The surface area of the targets loaded were 20.27 cm^2. The thickness for metallic targets was 0.64 cm. Ceramic targets were 0.32 cm thick with a bonded 0.32 cm copper backing to insure they were not electrically isolated from the chamber. Furthermore, the copper backing is water cooled and acts a heat sink for the ceramic target. The sample stage has a boraelectric heater incorporated which allows deposition temperatures up to 1173 K. The sample temperature was monitored by a thermocouple (Type K) upon the surface of the heater, secured

Figure 3.10: Schematic of the Magnetron Sputtering System. Magnetron A320-XP is perpendicular to the sample with a working distance of 13 cm from the substrate surface. The working distance between the sample and Magnetron A320-LA = 11cm. Magnetron A320-LA is placed at a 50° angle with respect to the sample surface. The boraelectric heater is situated beneath the sample holder.

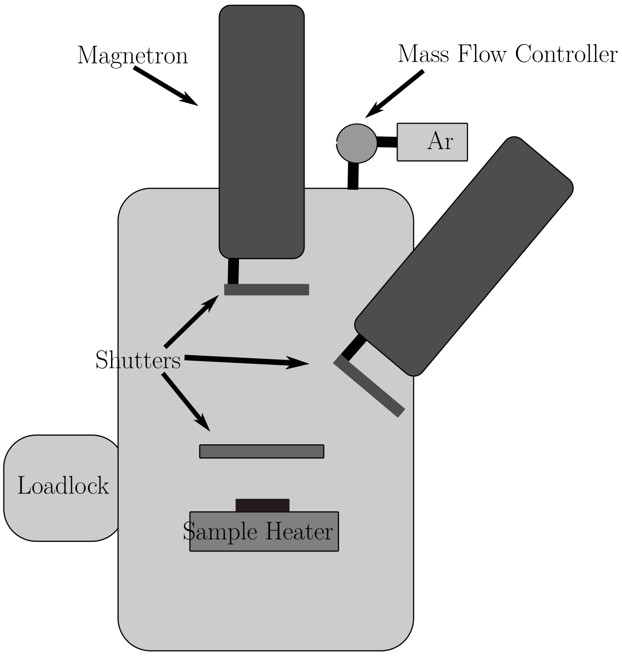

in placed by tantalum foil.

The base pressure of the system was $5{\times}10^{-5}$ Pa. The sputtering gas was controlled by a STEC IMC mass flow controller (SEC-4400MC-UC). For this work, argon was soley used as a sputtering gas but reactive sputtering of targets is also a possibility for the system.

Growth of $Cr_{2-x}Mg_xO_3$

A ceramic target of Cr_2O_3 doped with 8 % magnesium (Purity: 99.9 %) was supplied by Kurt J. Lesker. The ignition of a plasma occurred at 1 Pa. The pressure of the argon gas during deposition was 0.5 Pa at 150 W. The target was pre-sputtered for a period of 5 minutes before deposition began at the same argon pressure and RF power. Pre-sputtering removes any adsorbates or oxdisation on the target surface that may have occurred in the interim, providing a consistent starting point for growth each time.

Growth of ZnO

A ceramic target of ZnO (Purity: 99.9 %) was supplied by Kurt J. Lesker. The ignition of a plasma occurred at 1 Pa. The pressure of the argon gas during deposition was 0.5 Pa at 50 W. The target was pre-sputtered for a period of 5 minutes before deposition began at the same argon pressure and RF power. The deposition temperature was fixed at 993 K.

3.8 Spray Pyrolysis

Spray pyrolysis is the third deposition technique used within this thesis to grow p-type TCO films. It is used within this work to deposit Cu_xCrO_2 films. Spray pyrolysis is a process in which a thin film of material is deposited by spraying a precursor solution through an air atomiser onto a heated surface. The chemical reactants are selected such that everything other than the desired products are volatile at the surface temperature of the substrate.

3.8.1 Deposition Chamber

Our spray pyrolysis setup was a confined environment (Abbess 18" Cube), employing an air blast atomizer nozzle (PNR Air assisted ultrasonic atomizer, model MAD 0331 B1BA) placed at above a hot plate. Air and nitrogen was used as carrier gas, and mass flow controllers was used to regulate the flow. The oxygen concentration inside the chamber was monitored using an oxygen sensor (Sensortechnics, model XYA1) placed at a distance of 35 cm away from the nozzle. For the liquid delivery, a peristaltic pump (Watson Marlow Pumps Peristaltic 520S) has been used.

Copper acetylacetonate (0.012 M) and chromium acetylacetonate (0.03 M) precursors were dissolved in methanol. The solution was sprayed at a rate of 1.67 ml min^{-1} with an air blast nozzle (PNR, model 0331) using a mixture of compressed air/nitrogen (5 %/95 %) controlled with a mass flow controller

(Vogtlin, model red-y). The gas pressure was held constant at 17 L min^{-1}. This was sprayed from a distance of 30 cm above a hot plate. Two substrates were used for this work: glass microscope sildes (Fisher brand, thickness 0.8-1 mm) and polyimide (DuPont Kapton) film. The polyimide film rested upon microscope glass slides which lay on the hot plate surface. Heater surface temperature readings during spraying were taken using a type K thermocouple (chromel vs. alumel) welded to the top of the hot plate. The temperature was Proportional Integral Derivative (PID) controlled during spray conditions within 10 K. The surface temperature at the substrate may systematically differ.

Material Characterisation

All as grown materials required analysis of their structural, electronic and optical properties before any spectroscopic in depth analysis could occur.

3.9 X-ray Diffraction

X-Ray Diffraction (XRD) is a technique to analyse crystalline material. In 1912, Von Laue discovered that crystalline substances act as diffraction gratings to incident waves that have a comparable spacing to the planes in a crystal lattice [27]. The diffracted x-rays in a crystalline material constructively interfere when conditions that satisfy Bragg's law are met:

$$n\lambda = d \sin\theta \tag{3.14}$$

where n is an integer, θ the Bragg angle, λ the wavelength of the incident beam and d the spacing between diffraction planes. The directions of possible diffractions depend on the size and shape of the unit cell of the material. The intensities of the diffracted waves depend on the kind and arrangement of atoms in the crystal structure. Structural information such as the unit cell dimensions, crystallite size, disorder and strain can be obtained from the diffraction patterns.

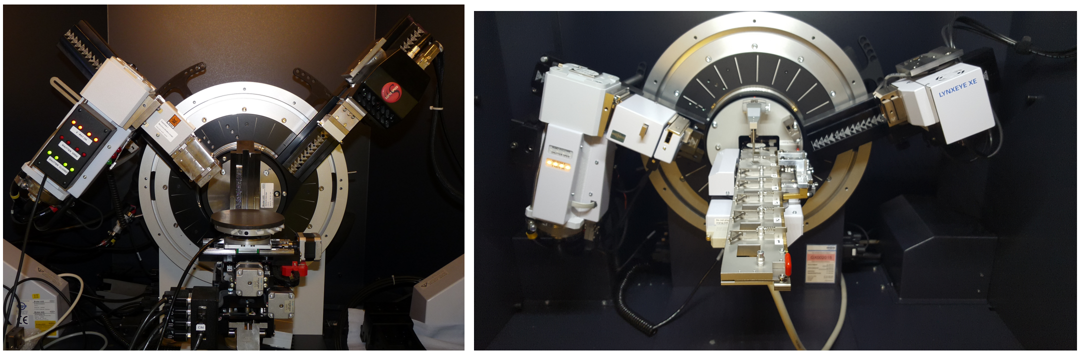

Figure 3.11: (a) High resolution x-ray Diffraction, Bruker D8 Discover (b) Powder x-ray Diffraction, Bruker D8 Advance

XRD patterns have been measured with a Bruker D8 Discover, figure 3.11 (a) using a monochromated Cu-Kα source for epitaxial thin films and grazing incidence measurements. Nanocrystalline films were measured using a Bruker D8 Advance which contains a Mo-Kα source.

3.10 X-ray Reflectivity

The growth rates for all deposition techniques like MBE and magnetron can be monitored *in-situ* with quartz crystal oscillators. The growth rate of the crystal monitors is calibrated by cross referencing the thickness of the film by X-Ray Reflectivity (XRR) which gives high precision value for the thickness of thin films. Thin films can only be measured by XRR if less than 150 nm in thickness with a low surface and substrate roughness.

XRR is based upon the measurement of reflected x-rays from a film surface. Any incident electromagnetic waves upon surfaces are refracted, diffusely, and specularly reflected. Studying the light reflected or transmitted by a thin film reveals information on the thickness, roughness and density of the material interacting with the light. When the thickness of the film is a multiple of a half-wavelength of the light, the two reflected waves reinforce each other, increasing the reflection and reducing the transmission. If the electromagnetic waves are within the x-rays photon energy regime the refractive index can be written as:

$$n = 1 - \delta - i\beta \tag{3.15}$$

where δ is the dispersion term and β term. The real part of the refrative index (1-δ) in the high-frequency limit of the Drude model is given as:

$$n = 1 - \omega_p^2/\omega^2 \tag{3.16}$$

where ω and ω_p are the x-ray photon and plasma frequency, respectively. The incident x-rays have a photon energy well above the plasma frequency of materials hence the real part of the refractive index will have values slightly below 1. At grazing incidence there will be total external reflection of the x-ray wave. The critical angle (θ_c) can be calculated from Snell's law.:

$$\theta_c = \arcsin \frac{n_{\text{film}}}{n_{\text{air}}} \tag{3.17}$$

where n_{film} and n_{air} are refractive indexes of the film and air respectively. At the critical angle some proportion of the incident x-rays propagate along the surface. Above the critical angle some x-rays penetrate into the material by refraction.

These sharp changes in reflected intensity allow the precise determination of the critical angle. The refractive index of the film can then be determined, which is directly proportional to ρ the film density ($n_{\text{film}} - 1 \propto \rho$). Diffuse reflection of the x-rays increases with surface roughness, which reduces the intensity of the oscillations. Increased surface/interface roughness reduces the coherence length of reflected x-rays, which causes a damping of oscillations. These effects can be quantified and values for film thickness, surface, interface roughness and density are produced [28, 29].

The measurement and quantification of the resultant interference pattern that X-ray Reflectivity (XRR) from thin films is outlined in figure 3.12. A sample XRR spectra is given in figure 3.12. 150 nm is the upper limit of the film thickness that

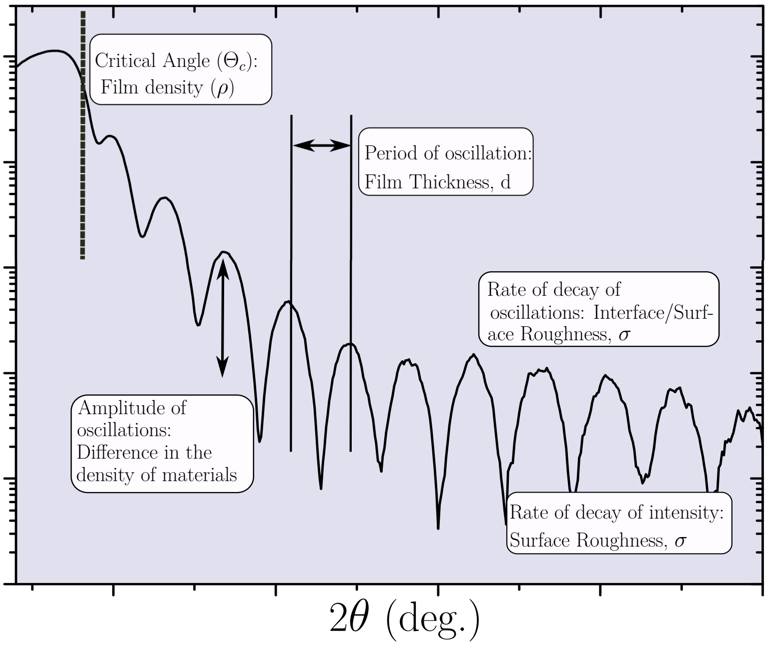

Figure 3.12: X-ray reflectivity of a thin film of iron grown upon MgO (001) outlining the information that is provided

can be quantified on the Bruker D8 Discover due to limitations in the resolution and coherence length of x-rays [29, 30].

3.11 Electrical Measurements

Quantifying the electrical properties of a TCO is crucial to optimise it's performance. The sheet resistance of all TCOs were measured by four point probe system (described below). When combined with the thickness value determined by XRR, the resistivity was quantified. The sheet resistance versus temperature was measured to give an estimate of activation energy of charge carriers within the TCOs. The mobility of the TCOs was immeasurable with the Hall effect. An alternative method of quantifying the carrier mobility is described.

3.11.1 Four Point Probe Measurements

Four point probe measurements are carried out by applying a current across two contacts and measuring the induced voltage across two separate electrodes. This is illustrated in figure 3.13 (a). The separation of current and voltage electrodes eliminates the contact and lead resistance from the measured resistance. Low or high resistance samples require the application of an adjusted applied current. The re-adjustment of applied current and sense voltage is done automatically by a LabVIEW script. The applied DC current to the sample is adjusted so that power dissipation does not exceed 10 mW, while ensuring that the sense voltage does not exceed 5 V.

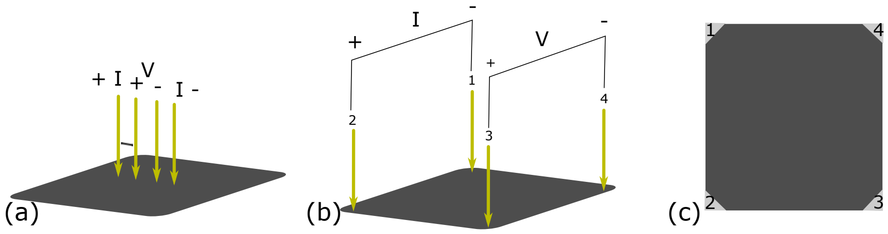

Figure 3.13: (a) Linear 4 point probe geometry (b) Van der Pauw 4 point probe geometry (c) Placement of silver contacts

It is assumed that the current travels only along the plane of the sheet not perpendicular, a valid assumption for thin film metal oxides. Practically, with a homogeneous sample with identical contacts, the sheet resistance is related to the measured resistance as:

$$R_s = \frac{\pi R}{\ln(2)} \tag{3.18}$$

This approximation relies on the assumption that the sample generates a voltage analogous to a dipole within an infinite sheet which only holds when a sample is larger than the probe distance. For a probe spacing of 2 mm the sample should be greater than 25 mm × 25 mm. The single crystal substrates use in this work (10 mm × 10 mm) have an overestimated sheet resistance by 27 % [31]. All sheet resistances have been reduced by the appropriate factor.

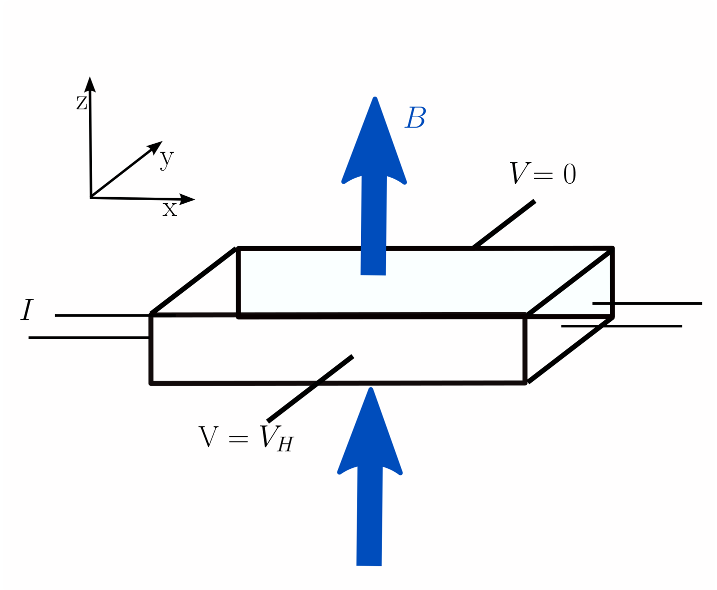

Figure 3.14: Schematic of the Hall effect measurement on a material. The coordinate system is defined in the top left.

The linear four point probe experimental setup consists of a Keithley 2400 sourcemeter. The electrodes were spring loaded gold probes supplied by CODA-PIN. Sheet resistance versus temperature measurements were carried out on the same linear point probe experimental setup. The sample was heated by a Watlow ceramic heater which varied the sample temperature between 323 K and 593 K controlled by an Omega i-Series PID controller model number CNi16D53-EI.

3.11.2 Hall Effect

The mobility of TCOs can be quantified using the Hall effect measurements. The basic physical principle underlying the Hall effect is the Lorentz force, which is the combination of the electric and magnetic forces. An electron moving perpendicular to an applied magnetic field with experience a magnetic force $(-qv \times B)$. The resulting Lorentz force is equal to $-q(E+v \times B)$ where E is the electric field, v is the particle velocity and B is the magnetic field. For an n-type semiconductor the carriers are predominately electrons of bulk density n. We assume that a constant current (I) flows along the x-axis from left to right in the presence of a z-directed magnetic field. Electrons subject to the Lorentz force initially drift away from the current direction toward the negative y-axis, resulting in an excess negative surface electrical charge on this side of the sample. This charge results in the Hall voltage, a potential drop across the two sides of the sample. This transverse voltage is the Hall voltage V_H with a magnitude of:

$$V_H = \frac{IB}{qnt} \tag{3.19}$$

where I is the current, B is the magnetic field, t is the sample thickness, and q is the elementary charge. In some cases, it is convenient to use layer or sheet density ($n_s = n_c$) instead of bulk density. Since sheet resistance involves both sheet density and mobility, one can determine the Hall mobility from the equation:

$$\mu = \frac{|V_H|}{\rho} = \frac{|V_H|}{BIR_s} \tag{3.20}$$

The sheet resistance R_s of the semiconductor can be conveniently determined by use of the van der Pauw resistivity measurement technique.

van der Pauw technique

In order to determine both the mobility and the sheet density n_s, a combination of a resistivity measurement and a Hall measurement is needed. As originally devised by van der Pauw [32], one uses an arbitrarily shaped thin film containing four very small ohmic contacts placed on the corners of the plate. A schematic of a rectangular van der Pauw configuration is shown in figure 3.13 (b).

Van der Pauw demonstrated that there are actually two characteristic resistances $R_A = V_{43}/I_{12}$ and $R_B = V_{14}/I_{23}$, associated with the corresponding terminals shown in figure 3.13 (c). To obtain the two characteristic resistances, one applies a DC current I into contact 1 and out of contact 2 and measures the voltage V_{43} from contact 4 to contact 3 [32]. R_A and R_B are related to R_s

through the van der Pauw equation:

$$e^{-\pi R_A/R_s} + e^{-\pi R_B/R_s} = 1 \tag{3.21}$$

This equation can be solved for R_s anaytically for a homogeneous square. It can be solved numerically for R_s when measuring other irregularly shaped samples. The same setup in figure 3.13 (c) can also be used for the Hall measurement. To measure the Hall voltage V_H, a current I is forced through the opposing pair of contacts 1 and 3 and the Hall voltage V_H $(= V_{24})$ is measured across the remaining pair of contacts 2 and 4. Once the Hall voltage V_H is acquired, the sheet carrier density n_s can be calculated via $n_s = IB/q|V_H|$ from the known values of I, B, and q.

3.11.3 Thermoelectric Measurements

The Hall effect failed to measure the Hall coefficient of any of the p-type TCOs discussed within this work due to that fact that the thermal voltage resulting from thermal instability was larger than the detectable Hall voltage.

Despite the lack of detectable Hall voltage from our p-type oxide films, an alternative method exists for estimating the carrier mobility within a material using the Seebeck effect. If a temperature gradient is created within a material, a potential difference will be created due to the diffusion of charge carriers. The Seebeck coefficient measured the magnitude of the potential difference that arises:

$$SB = -\frac{\Delta V}{\Delta T} = -\frac{V_{hot} - V_{cold}}{T_{hot} - T_{cold}} \tag{3.22}$$

An estimate of the Seebeck mobility can be made for the charge carriers in a thin film. For $Cr_{2-x}Mg_xO_3$ the magnesium acceptor dopes the Cr_2O_3 lattice when it replaces a chromium site [33]. Assuming a Small Polaron Model (SPH) holds for $Cr_{2-x}Mg_xO_3$, the ratio of occupied to available hopping sites (c) can be expressed as [34]:

$$c = \frac{[\mathrm{Mg}^{2+}]}{[\mathrm{Mg}^{2+}] + [\mathrm{Cr}^{3+}]} \tag{3.23}$$

The Seebeck coefficient can be directly related to the fraction of occupied carrier sites:

$$S = \pm\frac{k}{e}\ln\frac{2(1-c)}{c} \tag{3.24}$$

as the Seebeck effect is produced by charge carrier diffusion which is directly related to the fraction of carrier sites occupied. Measured c values ranged from 0.05-0.3 and were around two to three times larger than expected for the nominal magnesium/chromium ratio. Mg^{2+} would be expected to generate one charge carrier per substitution. However, the expected values are based on a very simple assumption of the number of potential available hopping sites and also assuming that a homogeneous Mg distribution does not affect the Cr coordination. For highly doped material, dephasing or the presence of compensating defects reduces the total number of available hopping sites, and a larger c is possible. Within the SPH model, c is related to the carrier concentration p by $p = Nc$, where the density of conducting sites N can be calculated using the unit cell volume of the $\mathrm{Cr_2O_3}$ lattice and the number of chromium atoms per unit cell. Using the measured conductivity and c values, the Seebeck mobility can be written as:

$$\mu = \frac{\sigma}{pe} \tag{3.25}$$

The highest Seebeck mobility for $\mathrm{Cr}_{2-x}\mathrm{Mg}_x\mathrm{O}_3$ was 1×10^{-4} $\mathrm{cm^2V^{-1}s^{-1}}$ [24]. It is likely that N is overestimated, as not every chromium site is an available hopping site, then the model is underestimating the mobility. This process was repeated for $\mathrm{CuCrO_2}$ and gave an Seebeck mobility of $6.4\times10^{-3}\mathrm{cm^2V^{-1}s^{-1}}$ [34].

3.12 UV-Vis Spectroscopy

The optical properties of all TCOs were characterised with a Perkin Elmer 650 lamba spectrophotometer which measured reflectance and transmittance of Ultra-Violet Visible (UV-Vis) from thin films. The system consists of a deuterium and tungsten-halogen lamp as sources in conjunction with a R6872 photomultiplier as the detector. The wavelength ranges from 200 nm to 850 nm. The system is a double beam and double monochromator (to separate the different wavelengths of light), ratio recording optical system. Integrated transmittance and reflectance are measured using a 150 mm integrating sphere to include the scattered transmittance and reflectance.

Bibliography

[1] Carl Nordling, Evelyn Sokolowski, and Kai Siegbahn. “Precision method for obtaining absolute values of atomic binding energies”. *Physical Review* 105.5 (1957), 1676.

[2] T Koopmans. “Über die Zuordnung von Wellenfunktionen und Eigenwerten zu den Einzelnen Elektronen Eines Atoms”. *Physica* 1.1-6 (1934), 104–113.

[3] CS Fadley. “X-ray photoelectron spectroscopy: Progress and perspectives”. *Journal of Electron Spectroscopy and Related Phenomena* 178 (2010), 2–32.

[4] C. S. Fadley. *Electron Spectroscopy: Theory, Techniques and Applications.* Ed. by C. R. Brundle and A. D. Baker. Vol. 2. Academic Press, 1978.

[5] N. F. Mott. “Conduction in non-crystalline materials”. *Philos. Mag.* 19 (1969), 835.

[6] Sunjic Doniach and M Sunjic. “Many-electron singularity in X-ray photoemission and X-ray line spectra from metals”. *Journal of Physics C: Solid State Physics* 3.2 (1970), 285.

[7] Y.M. Cross and J.E. Castle. “The relationship between transmission efficiencies in the FRR and fat modes of an electron spectrometer”. *Journal of Electron Spectroscopy and Related Phenomena* 22.1 (1981), 53.

[8] L Kövér, J Tóth, and A Itoh. “An experimental method for resolution calibration of electron spectrometers”. *Acta Physica Hungarica* 65.2 (1989), 217–223.

[9] M Pl Seah and WA Dench. “Quantitative electron spectroscopy of surfaces: A standard data base for electron inelastic mean free paths in solids”. *Surface and interface analysis* 1.1 (1979), 2–11.

[10] RL Anderson. “Germanium-gallium arsenide heterojunctions [letter to the editor]”. *IBM Journal of Research and Development* 4.3 (1960), 283–287.

[11] John Bardeen. “Surface states and rectification at a metal semi-conductor contact”. *Physical Review* 71.10 (1947), 717.

[12] Martin A Green, Anita Ho-Baillie, and Henry J Snaith. “The emergence of perovskite solar cells”. *Nature Photonics* 8.7 (2014), 506–514.

[13] J.F. Wager. “Transparent electronics: Schottky barrier and heterojunction considerations”. *Thin Solid Films* 516.8 (2008), 1755.

[14] E. A. Kraut et al. “Semiconductor core level to valence band maximum binding energy differences”. *Phys. Rev. B* 28 (4 1983), 1965.

[15] A. Klein et al. “Band lineup between CdS and ultra high vacuum-cleaved $CuInS_2$ single crystals”. *Applied Physics Letters* 70.10 (1997), 1299.

[16] J. R. Waldrop. “Measurement of semiconductor heterojunction band discontinuities by x-ray photoemission spectroscopy”. *J. Vac. Sci. Technol. A* 3.3 (1985), 835.

[17] Frank De Groot and Akio Kotani. *Core level spectroscopy of solids*. CRC press, 2008.

[18] Joachim Stöhr. *NEXAFS spectroscopy*. Vol. 25. Springer Science & Business Media, 2013.

[19] T Takahashi et al. “Evidence from angle-resolved resonant photoemission for oxygen-2p nature of the Fermi-liquid states in $Bi_2CaSr_2Cu_2O_8$”. *Nature* 334.6184 (1988), 691–692.

[20] DMP Holland. “The Daresbury synchrotron radiation source”. *Physica Scripta* 36.1 (1987), 22.

[21] Donald H Bilderback, Pascal Elleaume, and Edgar Weckert. “Review of third and next generation synchrotron light sources”. *Journal of Physics B: Atomic, molecular and optical physics* 38.9 (2005), S773.

[22] Ralf Nyholm et al. “A soft X-ray monochromator for the MAX synchrotron radiation facility”. *Nuclear Instruments and Methods in Physics Research Section A: Accelerators, Spectrometers, Detectors and Associated Equipment* 246.1-3 (1986), 267–271.

[23] Alfred Y Cho. “How molecular beam epitaxy (MBE) began and its projection into the future”. *Journal of Crystal Growth* 201 (1999), 1–7.

[24] L. Farrell et al. “Conducting mechanism in the epitaxial p-type transparent conducting oxide Cr_2O_3:Mg”. *Phys. Rev. B* 91.12 (2015), 125202.

[25] Donald Smith. *Thin-film deposition: principles and practice.* McGraw Hill Professional, 1995.

[26] PJ Kelly and RD Arnell. “Magnetron sputtering: a review of recent developments and applications”. *Vacuum* 56.3 (2000), 159–172.

[27] W Friedrich et al. “Sitzungsberichte der Königlich Bayerischen Akademie der Wissenschaften”. *Mathematische-Physische Klasse* 42 (1912), 303–322.

[28] A Braslau et al. “Surface roughness of water measured by x-ray reflectivity”. *Physical review letters* 54.2 (1985), 114.

[29] Lyman G Parratt. “Surface studies of solids by total reflection of x-rays”. *Physical review* 95.2 (1954), 359.

[30] Metin Tolan. *X-ray scattering from soft-matter thin films: materials science and basic research.* Springer, 1999.

[31] FM Smits. “Measurement of sheet resistivities with the four-point probe”. *Bell Labs Technical Journal* 37.3 (1958), 711–718.

[32] I. J. van der Pauw. “A method of measuring specific resistivity and hall effect of discs of arbitrary shape”. *Philips Res. Repts.* 13 (1958), 1.

[33] Aoife B Kehoe et al. “Assessing the potential of Mg-doped Cr_2O_3 as a novel p-type transparent conducting oxide”. *Journal of Physics: Condensed Matter* 28.12 (2016), 125501.

[34] Leo Farrell et al. “Synthesis of nanocrystalline Cu deficient $CuCrO_2$: a high figure of merit p-type transparent semiconductor”. *J. Mater. Chem. C* 4.1 (2016), 126.

Chapter 4

Investigating the Electronic Band Structure $Cr_{2-x}Mg_xO_3$ and it's applicability in Electronic Devices

Cr_2O_3 has been recently reported as demonstrating p-type conductivity when doped extrinsically with magnesium, nickel or lithium [1–4]. The first half of this chapter focuses on understanding the electronic properties of $Cr_{2-x}Mg_xO_3$ films using several spectroscopic techniques: X-ray Absorption Spectoscopy (XAS), X-ray Photoelectron Spectroscopy (XPS) and Resonant Photoemission Spectroscopy (RPES). The studies within this chapter will focus on the lack of dispersion of the Cr 3*d* states within the valence band as a function of increasing long range crystalline order.

An important aspect of the semiconducting industry has been reliant on the materials silicon and germanium having the ability to be both p and n-type doped. Although Cr_2O_3 can be bipolar doped, allowing for the manufacture of a homo-junction, the n-type counterparts such as $Cr_{2-x}Ti_xO_3$ have been of extremely low conductivity. Titanium specifically as a dopant is difficult to incorporate with a fixed oxidation state of 4+ [5].

However, without the properties of the n-type counterpart optimised, the p-type $Cr_{2-x}Mg_xO_3$ will be investigated for applications where high mobility of the charge carriers within the oxide is not vital importance. One of these applications is as a selective contact to aid extraction holes from the active layer towards the anode within a solar cell. The Valence Band Offset (VBO) and Conduction Band Offset (CBO) created at the interface between the selective contact and anode govern how effective the selective contact is at aiding this process. But the VBO and CBO predicted by Anderson's rule often significantly differs from the real alignment at the interface of two oxides. Instead the band alignment of novel oxides will be investigated experimentally by photoemission spectroscopy, the methodology of which is outlined in Section 3.2.

4.1 Doping of Cr_2O_3

Stoichiometric Cr_2O_3 is an insulator with some reports of intrinsic p-type conduction [6]. Cr_2O_3 adopts a corundum structure: a hexagonal close packed array of oxide anions with 2/3 of the octahedral holes occupied by chromium. Conventional electronic band structure models would predict Cr_2O_3 to be an electrical conductor with no band gap whereas in reality it behaves as a Mott-Hubbard insulator with a band gap [7, 8] The optical, electrical and magnetic properties of the corundum structure are highly correlated to the c/a lattice ratio and cation-cation distances [9]. Cr_2O_3 has a reported optical gap of 3.4 eV [10]. However, it has been well reported that sub band gap transitions exist below 3.4 eV indicating that the fundamental gap between the conduction and valence band is less than this value [8]. Theoretical calculations concerning the fundamental band gap will be elaborated on in Section 4.6.5.

Most promisingly, extrinsic doping of Cr_2O_3 with magnesium and nickel has produced high FoM p-type TCOs [3, 4]. The basis of this work arose from promising results from spray pyrolysis $Cr_{2-x}Mg_xO_3$ films which showed poor crystallinity but produced conductivities as high as 0.11 Scm^{-1}. The mobility of the films was unquantifiable but this was initially believed to be caused by the poor crystalline quality [11].

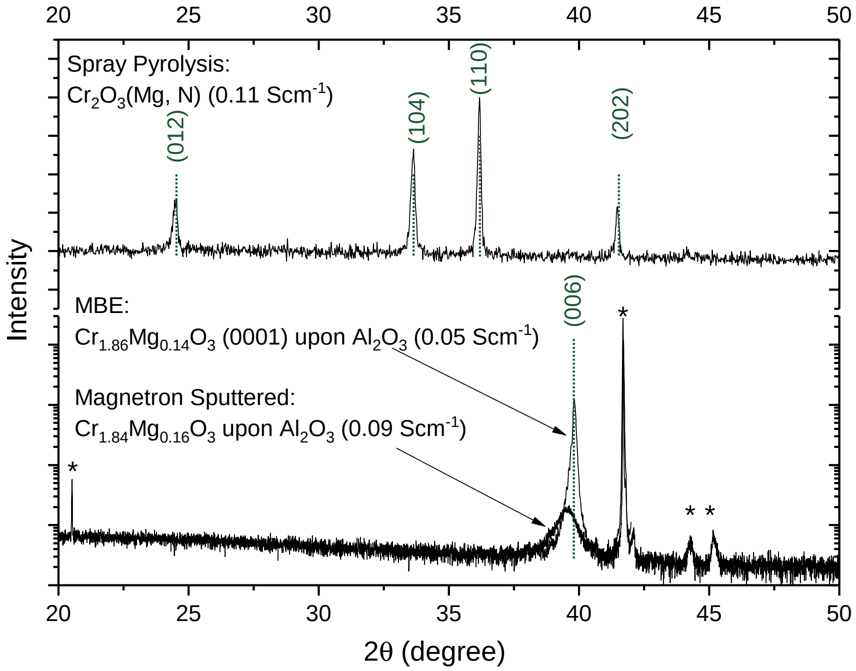

Figure 4.1: X-ray diffraction of $Cr_{2-x}Mg_xO_3$ films grown by spray pyrolysis, magnetron sputtering and molecular beam epitaxy. The top panel plots data for the highest quality spray pyrolysis films with a conductivity of 0.1 Scm^{-1} obtained from Grazing Incidence X-ray Diffraction (GIXRD). The diffraction lines observed are consistent with an eskolaite phase. The lower panel shows the data for epitaxially grown $Cr_{2-x}Mg_xO_3$(0.05 Scm^{-1}) and magnetron sputtered $Cr_{2-x}Mg_xO_3$(0.09 Scm^{-1}) taken by a symmetric $\theta/2\theta$ scan. Diffraction lines originating from the substrate (Al_2O_3) and the sample holder have been marked with an asterisk (*)

The development of the growth of $Cr_{2-x}Mg_xO_3$ films by MBE produced epitaxial films that improved the conductivity of the films by a factor of two but the mobility of the charge carriers could still not be measured by the Hall effect.

A review of the literature uncovered a trend: Cu_xCrO_2, $CuCrO_2$:Mg, $LaCrO_3$:Sr and $Cr_{2-x}Mg_xO_3$ all had very low mobilities [12], that could only be estimated by the Seebeck Effect (see Section 3.11.3) [13]. Only $CuCrO_2$:Mg was measurable by the AC Hall effect [14]. All chromium containing metal oxides have similar properties of reasonable conductivity (0.01 to 100 Scm^{-1}), very high carrier concentrations, but a very low mobility (see figure 2.8).

Hence, the electronic structure of the valence band of $Cr_{2-x}Mg_xO_3$ was probed by XPS and RPES to provide insight into the origin of the low mobility of chromium based oxides. First, the local coordination was analysed by XAS, characterising how the magnesium doping of the Cr_2O_3 lattice affects the absorption and core level spectra.

4.2 Local Coordination

4.2.1 Surface Preparation

XAS measurements require synchrotron radiation and hence unavoidable *ex-situ* transfer of samples. Surface carbon would in particular obscure the measurement of the valence band, so preparation of the surface was required. The Cr_2O_3 and $Cr_{2-x}Mg_xO_3$ films were sputtered with argon ions with a beam energy of 1 keV (the minimum energy available) at 4×10^{-4} Pa at grazing incidence to remove carbon while reducing the possible of inducing any disorder. This was repeated in 4 minute intervals until a surface sensitive XP spectrum ($h\nu = 380$ eV) of the C 1s core level region showed no carbon present. The $Cr_{2-x}Mg_xO_3$ samples were oxygen annealed at 600 K in an oxygen partial pressure of 1×10^{-3} Pa to restore the surface stoichiometry as oxygen may have been preferentially sputtered.

The Cr $L_{2,3}$ edge of epitaxial Cr_2O_3 thin films grown on Al_2O_3 was measured for comparison with the $Cr_{2-x}Mg_xO_3$ film. Figure 4.2 (a) shows the spectral features of $Cr_{2-x}Mg_xO_3$ and Cr_2O_3 which are very similar. Large changes have previously been seen in the Cr $L_{2,3}$ edge in the material $LaCrO_3$ when it was strontium doped. On substituting La by Sr the intensity of the Cr^{3+} features decreases and new features consistent the Cr^{4+} species can be observed [15]. In the case of $Cr_{2-x}Mg_xO_3$ films the splitting of the L_2 and L_3 edges has the same energetic value as the Cr_2O_3 lattice, indicating no large changes in the splitting of the 3d orbitals has changed with magnesium doping [16]. The only changes observed in a sample with 8 % substitutional magnesium doping of the Cr_2O_3 lattice was an increase in intensity of spectral feature A in the Cr L_3 edge.

Figure 4.2 (b) shows the Mg K edge of the $Cr_{2-x}Mg_xO_3$ films. The nominal

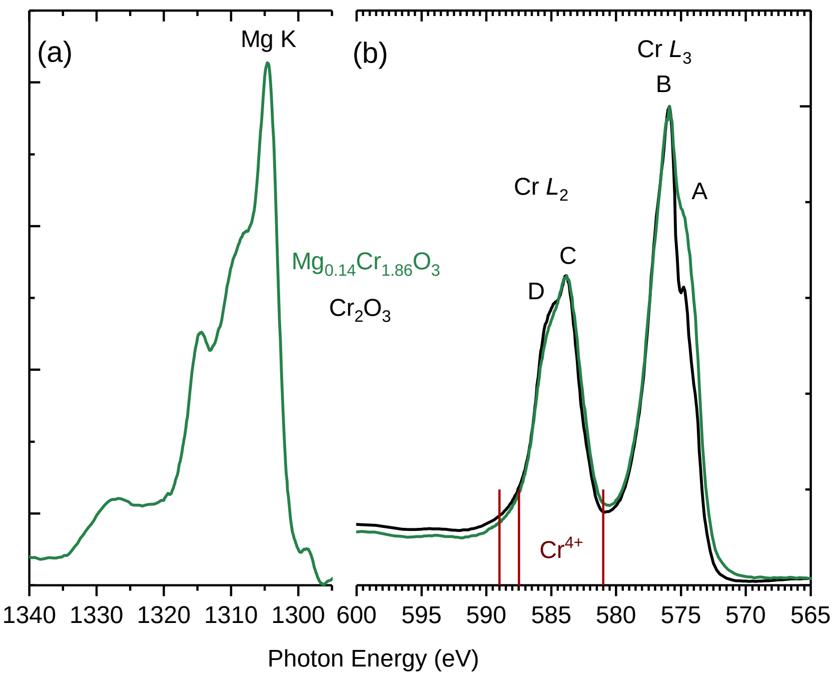

Figure 4.2: (a) X-ray absorption spectra of the Cr $L_{2,3}$-edge of Cr_2O_3 and $Cr_{2-x}Mg_xO_3$ (b) Mg K edge of $Cr_{2-x}Mg_xO_3$. The position of the Cr4+ absorption features would be expected at are denoted.

oxidation state of magnesium would be 2+. However, the Mg K edge is found at a higher energy with different spectral features when compared with the Mg K edge of bulk magnesium oxide. This is due to that fact that the magnesium is incorporated into the Cr_2O_3. Kehoe et al. has investigated the role of magnesium doping within chromium oxide and calculated the most thermodynamically likely defect was a magnesium ion replacing a chromium site [17]. This correlates with the higher Mg K edge energy seen in figure 4.2 (b) when compared to MgO as it has previously been attributed to the presence of distorted Mg-O_6 octahedron [18]. However, more detailed analysis of the Mg K edge would required modelling of the absorption spectra of magnesium within the Cr_2O_3 lattice. The core level photoemission spectra of $Cr_{2-x}Mg_xO_3$ and Cr_2O_3 also shows changes associated with doping of the lattice.

4.3 Cr 2p Core Level of $Cr_{2-x}Mg_xO_3$ Films

Multiplet splitting of the Cr 2p core level gave a unique opportunity to probe changes in the Cr 3d electrons in the valence band with doping.

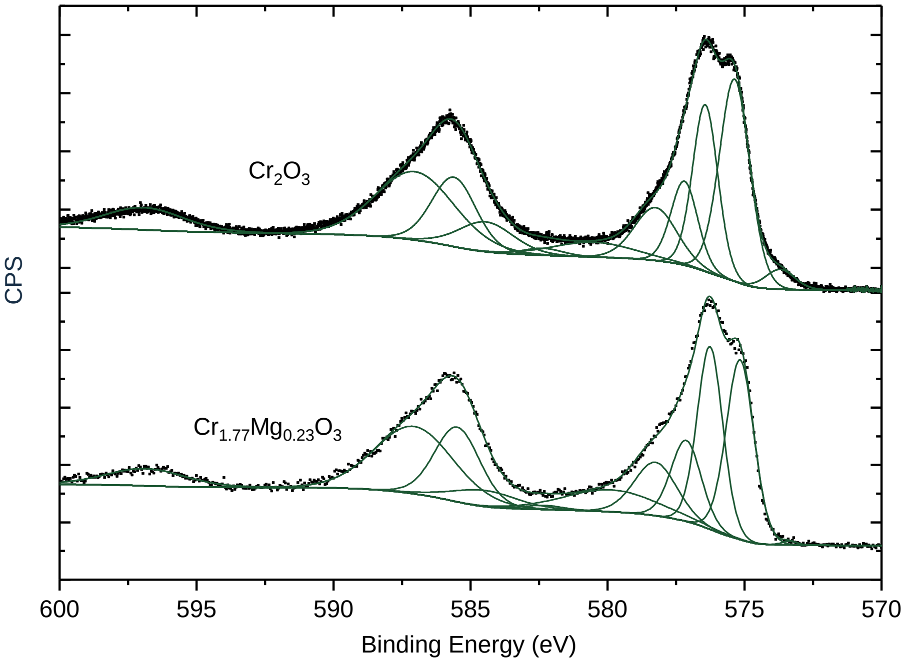

Figure 4.3: XP spectra of the Cr 2p core level of (a) Cr_2O_3(0001) on Al_2O_3 and (b) $Cr_{1.77}Mg_{0.23}O_3$(0001) on Al_2O_3

The Cr 2$p_{3/2}$ and 2$p_{1/2}$ peaks are non trivial to fit due to the fact that they broadened and show multiplet splitting due to the interaction of the 2p core hole with the unpaired 3d electrons in the valence band. In fact, the direct photoemission of the 2p core level does not appear within the 2p spectral regime [19]. Furthermore, the final state of the Cr 2$p_{3/2}$ and 2$p_{1/2}$ peaks are screened by a charge transfer from the polarizable oxygen ligands.

Biesinger et al. reported an empirical fitting of Cr 2p peak for Cr_2O_3 powder and bulk eskolaite [21]. However this model did not produce a sufficient fit to the core level for thin films of Cr_2O_3(0001) and $Cr_{2-x}Mg_xO_3$(0001) upon Al_2O_3.

Chambers and Droubay reproduced the shape of the Cr 2p core level with an atomic multiplet calculation using the program CTM4XAS. Over 100 multiplets

Table 4.1: Fitting parameters for the Cr 2*p* of Cr_2O_3. All peaks were fitted with a peak shape that is the product of 70 % Gaussain, 30 % Lorentzian

	Peak Position (eV)	FWHM (eV)	Area (%)
Cr 2*p* Peak 1	574.15	0.90	1
Cr 2*p* Peak 2	575.25	1.1	17.5
Cr 2*p* Peak 3	576.35	1.1	14.85
Cr 2*p* Peak 4	577.20	1.25	8.85
Cr 2*p* Peak 5	578.35	1.82	8.70
Cr 2*p* Peak 6	580	4.0	6.75
Cr 2*p* Peak 7	582.42	1.66	0.48
Cr 2*p* Peak 8	584.55	2.75	4.92
Cr 2*p* Peak 9	585.48	1.96	12.80
Cr $2p_{3/2}$ Satellite Peak	587.70	3.4	14.75
Cr $2p_{1/2}$ Satellite Peak	596.76	3.8	7.4

Table 4.2: Fitting parameters for the Cr 2*p* of $Cr_{2-x}Mg_xO_3$. All peaks were fitted with a peak shape that is the product of 70 % Gaussain, 30 % Lorentzian

	Peak Position (eV)	FWHM (eV)	Area (%)
Cr 2*p* Peak 1	574.2	1	0.20
Cr 2*p* Peak 2	575.17	1.2	17.58
Cr 2*p* Peak 3	576.24	1.1	17.37
Cr 2*p* Peak 4	577.12	1.25	8.91
Cr 2*p* Peak 5	578.25	1.82	8.66
Cr 2*p* Peak 6	580	4.0	7.13
Cr 2*p* Peak 7	582.42	1.66	0.48
Cr 2*p* Peak 8	584.55	2.75	4.92
Cr 2*p* Peak 9	585.48	1.96	12.80
Cr $2p_{3/2}$ Satellite Peak	587.70	3.4	14.75
Cr $2p_{1/2}$ Satellite Peak	596.76	3.8	7.37

are produced for the Cr 2*p* peak. 10 multiplets were selected with the highest probability and broadened with a Gaussian. In the case that two multiplets had identical positions only one representative transition was selected. Unfortunately, the CTM4XAS multiplet code does not give the detailed angular momentum character of each final state. Therefore the origin of the transition that gives rise to each individual multiplet is still unidentified [22].

Experimental fitting of the Cr 2*p* core level was improved upon by Ünveren et al. when the satellite contributions were included. A combination of the results from these two papers provided detailed fitting parameters for the Cr 2*p* peak.

The Full Width Half Maximum (FWHM), peak position and area for each peak that was fit to the experimentally observed Cr 2p core level in $Cr_{2-x}Mg_xO_3$ is contained in Table 4.2. The intensity, binding energy and peak position of each peak in unchanged by the magnesium doping of the film within the Cr 2p core level with one exception. The peak at the low binding energy side (BE = 575.15 eV) of the Cr $2p_{3/2}$ intensity is reduced in $Cr_{2-x}Mg_xO_3$ when compared with Cr_2O_3. This has previously been observed across at the CrN metal insulator transition and also within the delafossite $CuCrO_2$ when magnesium doped. It has been attributed to the screening effects of mobile carriers [23]. This indicates a large amount of charge carriers move around the Cr 3d sites, within the $Cr_{2-x}Mg_xO_3$ films.

4.4 Valence Band of $Cr_{2-x}Mg_xO_3$ Films

The concept of engineering high mobility TCOs is founded on creating dispersion within the valence band. Studies of the composition of the valence band would provide insight whether magnesium doping of the Cr_2O_3 creates such dispersion. However, unlike core level XPS, the valence band spectra provides non selective elemental sampling. Figure 4.5 shows the valence band spectra of $Cr_{1.76}Mg_{0.24}O_3$ and Cr_2O_3 films, both deposited upon polycrystalline ITO. The doping of the Cr_2O_3 lattice with magnesium has not introduced any visible spectral changes in the density of states within the valence band. The only observable change is that from insulating Cr_2O_3 to conductive $Cr_{1.76}Mg_{0.24}O_3$ there is a shift of the entire valence band upwards so the E_f-E_{VBM} value is reduced from 0.7 eV to 0 eV, consistent with the p-type character of $Cr_{2-x}Mg_xO_3$ films. Even though no visible changes are observed in the density of states within the valence band the magnesium doping may still cause delocalisation of the charge carriers.

Resonant Photoemission Spectroscopy (RPES) can be used to probe the elemental composition of the valence band: changes in the delocalisation of the charge carriers should be reflected in a dispersion of the Cr 3d states within the

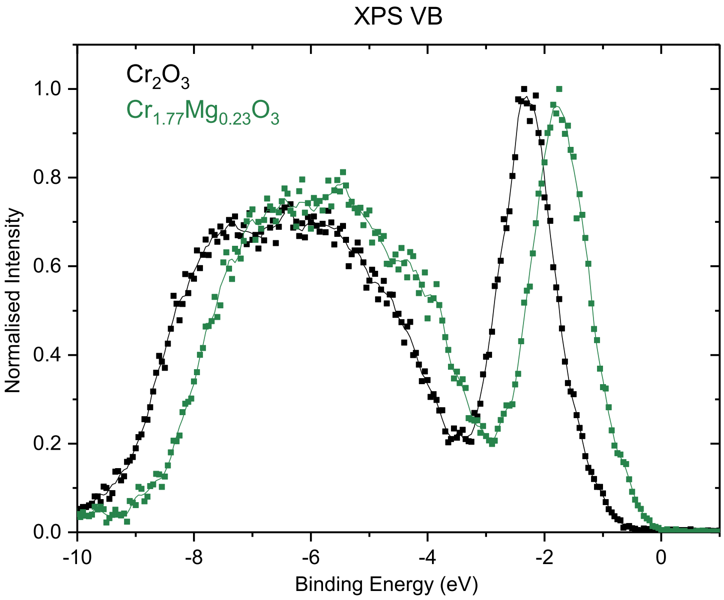

Figure 4.4: Comparison of the density of states of Cr_2O_3 and $Cr_{1.76}Mg_{0.24}O_3$. Both films are deposited upon ITO to circumvent the insulating nature of the undoped Cr_2O_3 film. The samples were grown and analysis without breaking vacuum.

valence band. The full theory behind RPES is contained in Section 3.4. If we have a tunable photon energy, we can generate a second excitation process, separate from the direct photoemission of an electron. The process is outlined for a $3p \rightarrow 3d$ transition:

- Direct Photoemission: $3d^n + h\nu \rightarrow 3d^{n-1} + e^{-1}$
- Resonant Photoemission: $3d^n + h\nu \rightarrow 3p^{5}\curvearrowright 3d^{n+1} \rightarrow 3p^6 3d^{n-1} + e^{-1}$

the $\curvearrowright$ arrow indicates the promotion of a core electron to an unoccupied states. Direct and resonant photoemission results in the same final state, but the process leading to that emission is quite different. The experiment requires measuring the same valence band spectra collected below, at and above the photon energies associated with an absorption edge. Any increase in intensity of states within the valence band while scanning across that absorption edge would indicate that final states associated with the second RPES process has occurred.

For the $Cr_{2-x}Mg_xO_3$ films the photon energies associated with the Cr $3p$ absorption edge will be scanned. Any increase in intensity of a specific feature

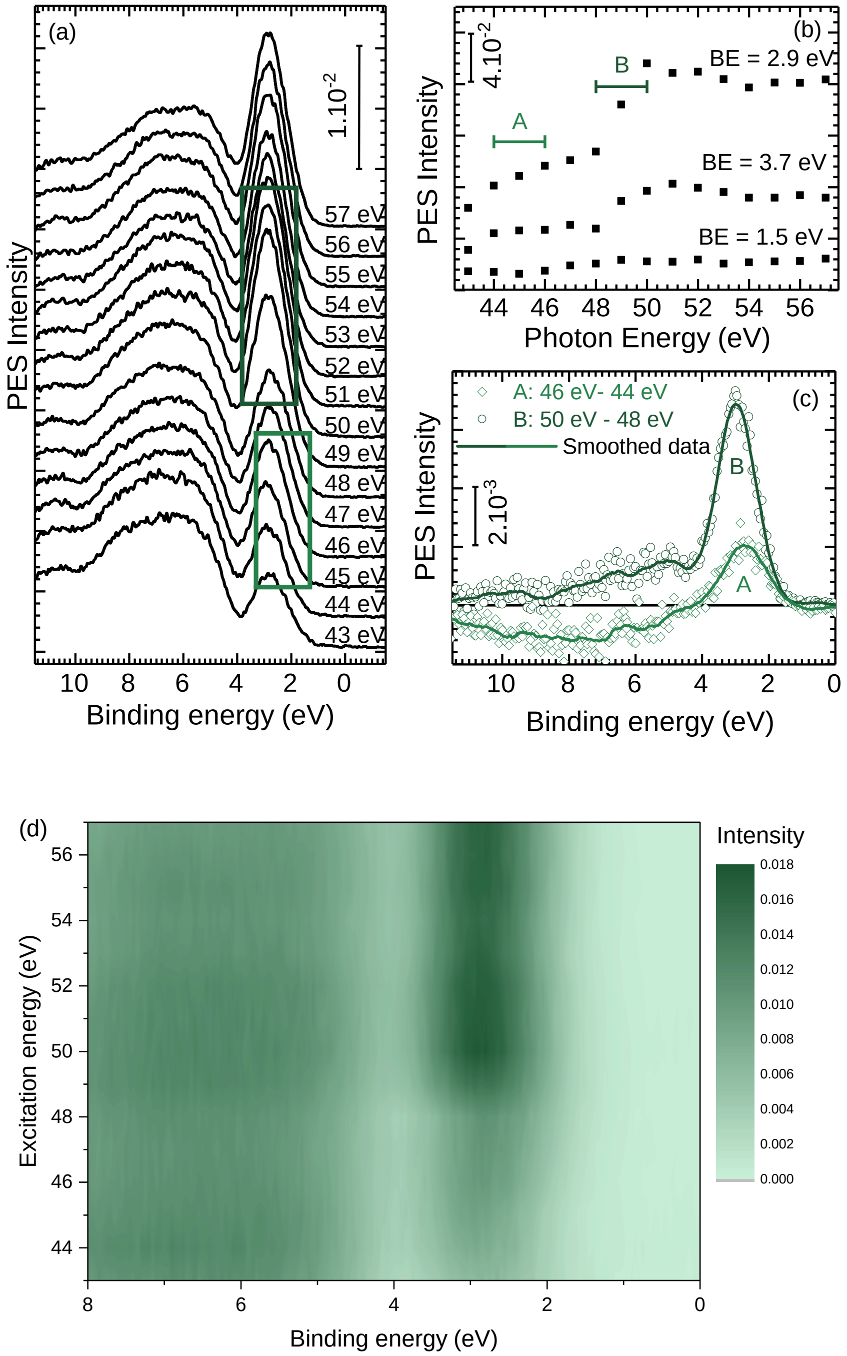
Chromium 3p-3d Resonance in $Cr_{2-x}Mg_xO_3$

Figure 4.5: (a) Valence band spectra of the $Cr_{1.86}Mg_{0.12}O_3$ film over the excitation energies 43 eV to 57 eV. The dark green box in (a) indicates the region where resonant behaviour over 48-50 eV is observed. The light green box indicates the lower resonance over 44-46 eV. (b) PES intensity for selected binding energies as a function of incident photon energy. (c) Differences between the spectra at 50 eV and 48 eV (○) reveal the strong Cr resonance around 3 eV and an increase of PES intensity of 0.7 %. The spectral difference between 46 and 44 eV (⋄) shows the onset of that resonance with an increase in PES intensity of 0.2 %. The negative differential signal in the 4-8 eV range is caused from going off-resonance to the oxygen p-states (d) Smoothed 2D plot mapping intensity of the valence band while scanning across the excitation energies of the Cr 3p absorption edge

within the valence band, as the photon energy is varied, would indicate an increase, in our case, of Cr $3d^{n-1}$ electrons emitted by photoemission through the intermediate resonant process.

Fig. 4.5 (a) plots the valence band photoemission intensity at a given binding energy as a function of photon energy expected to be resonant to the $3p$-$3d$ transition. The top of the valence band shows two separate resonances: a weak spectral response at 44-46 eV at a binding energy of 2.7 eV and a stronger resonant behaviour at 48-50 eV at a slightly higher binding energy of 3 eV.

The expected $3p$-$3d$ spectrum can be modelled using CTM4XAS software, to see if the origin of this double peak feature can be pinpointed [24]. For the atomic multiplet calculation the value of the crystal field parameter, 10 D_q, was chosen to be 2.03 eV; a value derived from the optical $2T_g$ – $2A_g$ transition observed in the pure epitaxially grown Cr_2O_3 films. This crystal field splitting is broadly consistent with that observed from pure single crystals of Cr_2O_3 where it was found to be 2.08 eV [25]. Although a trigonal distortion away from O_h to C_3 symmetry is present in the corundum lattice, the effect of such distortion on optical spectra is very small and various cluster and multiplet calculations effectively ignore this distortion as a result [26, 27].

The Cr $2p$ and $3p$ XPS, $L_{3,2}$ and $M_{3,2}$ XAS are all best modelled taking into account charge transfer multiplets, as shown in Section 4.3. A model for such charge transfer parameters has been previously put forward by Matsubara et al. [28] who successfully modelled Cr_2O_3 XAS, $2p$ XPS and $2p$-$3d$ Resonant Inelastic X-ray Scattering (RIXS) data. These same charge transfer energies are used in the present modelling. The $L_{3,2}$ XAS and $2p$ XPS are modelled with core hole lifetimes for the L_3 $2p_{3/2}$ hole of 0.32 eV and the L_2 $2p_{1/2}$ hole of 0.76 eV as recommended by Campbell and Papp [29], with an instrumental broadening of 0.1 eV and 0.3 eV respectively. Our model reproduces the expected spectral features seen in the Cr $2p$ and $3p$ XPS and $L_{3,2}$ XAS. Figure 4.6 shows a plot of the $M_{3,2}$ absorption edge. This edge and $3p$ XPS are modelled with core hole

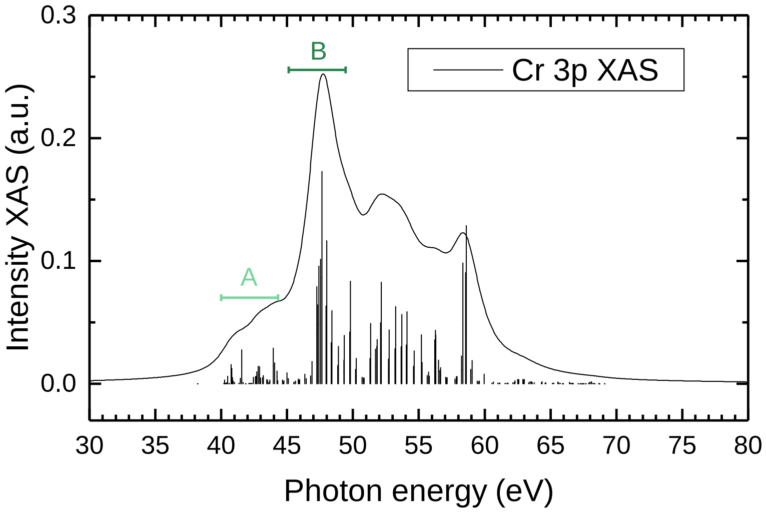

Figure 4.6: Cr $M_{3,2}$ XAS spectrum with the distribution of intensities as obtained in a charge transfer atomic multiplet calculation. Feature A: 40-45 eV is due to a dominant transition to a low spin XAS final state of $2p^5\ 3d^4$ (t_{2g}^4). The more intense feature B at higher excitation energies (49-55 eV) is the much more strongly allowed high spin XAS final state of $2p^5\ 3d^4$ ($t_{2g}^3e_g^1$).

lifetimes of 1.2 eV for the $M_{3,2}/3p$ holes and similar instrumental broadening. In figure 4.6, two features A and B are present in the $3p$ XAS spectra. Feature A, at the lower excitation energies of 40-45 eV, originates from a transition to a low spin XAS final state of $2p^53d^4$ (t_{2g}^4). The more intense feature, B, at higher excitation energies (49-55 eV) is the much more strongly allowed high spin XAS final state of $2p^53d^4$ ($t_{2g}^3e_g^1$) as previously remarked by both Li, Liu, and Henrich and Bertel et al. [30, 31]. In the case of the $M_{3,2}$ edge the atomic multiplet nature of the transitions dominate the intensity profile interlinked with the density and intensity of the allowed transitions to the given XAS final states. Although these are the XAS final states, they are the intermediate state in the $3p$-$3d$ resonant process and thus govern at what excitation energy the observed RPES feature occurs at and also how intense that feature will be. The origin of the features A and B in Fig. 4.5 in the $Cr_{2-x}Mg_xO_3$ film across the $3p$-$3d$ resonance can be linked to a difference in energy between the high and low spin states (t_{2g}^4) and ($t_{2g}^3e_g^1$) which are the intermediate states for RPES.

Ideally, RPES would now be carried out on Cr_2O_3 films to track the change in Cr_2O_3 3*d* states with magnesium doping. However photoemission studies, particularly RPES, require conductive films. Instead of making a direct comparison with an undoped Cr_2O_3 film a comparison will be made with conductive samples of crystalline $CuCrO_2$ and nanocrystalline Cu_xCrO_2 films in Chapter 5. This comparison as well as the screening of the pre-peak within the Cr 2*p* core level would indicate that there is a localisation of the holes within the Cr 3*d* states, leading to a low mobility, conductive TCO.

4.5 Investigating the Role of $Cr_{2-x}Mg_xO_3$ within Devices

Despite the localisation of holes upon the Cr 3*d* states and the resultant low mobility of charge carriers within $Cr_{2-x}Mg_xO_3$ films, the rarity of transparent conductive *p*-type materials means the exploration within niche applications where low mobility is not a limitation is necessary. One of these applications as discussed in Section 2.3.2 is as an Anode Buffer Layer (ABL) in solar cells, specifically in this instance organic solar cells.

4.5.1 Anode of a Bilayer Heterojunction Organic Solar Cell

Organic solar cells are cheap and facile to manufacture. An organic heterojunction solar cell is composed of two active layers (acceptor and donor) enclosed by an electrode either side [32]. The cathode is composed of a metal. The anode in this solar cell is usually composed of either ITO or FTO upon glass. Selective contacts can improve the efficiency of these solar cells substantially. Typically PEDOT:PSS, MoO_3 or NiO are deposited upon the anode to act as an anode buffer layer [33]. The role of ABLs are complex but a high work function p-type metal oxide usually performs well [34]. The concept of an anode buffer layer aids hole transport towards the anode from the organic layer while blocking the flow of electrons in this direction. Cr_2O_3 was seen to be another successful ABL for a particular cell (see figure 4.7) [35]. However, it did not out perform MoO_3. With the report of $Cr_{2-x}Mg_xO_3$ as a higher work function more conductive candidate compared with Cr_2O_3 it was thought that it could improve the efficiency of these simple solar cells further. Previous investigations had showed that 5 nm of Cr_2O_3 doubled the efficiency (0.16% → 0.35%) of the solar cell in figure 4.7 but resulted in the cell possessing a large series resistance (2220 Ω).

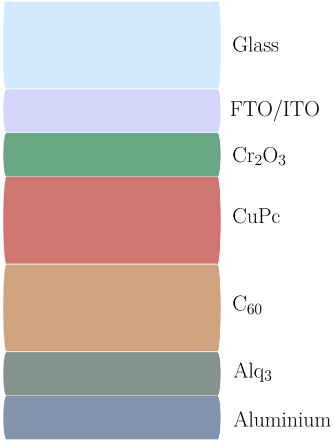

Figure 4.7: Schematic of an organic bilayer heterojunction solar cell FTO/ITO is the anode and aluminium is the cathode. The active layers of the device are Copper (II) Phthalocyanine (CuPc) and Fullerenes (C_{60}). The anode buffer layer is placed between the active layer and anode.

However, 5 nm $Cr_{2-x}Mg_xO_3$ when grown at the same thickness changed the efficiency from 0.16 % → 0.45 %. At the same time the series resistance of the cell was decreased by a factor of approximately five times compared with a solar cell with a buffer layer of undoped Cr_2O_3 of the same thickness. A larger improvement would have been expected due to the dramatic decrease in series resistance. The anode in this case was FTO upon glass. These organic solar cells have been synthesised and measured in the unpublished work of Mullarkey et al.

For this type of cell ITO or FTO can be used interchangeably. An anode buffer layer may perform differently due to the differing band alignment. Mapping the band alignment of the ITO-$Cr_{2-x}Mg_xO_3$ interface will give an indication if the combination of ITO-$Cr_{2-x}Mg_xO_3$ could improved the performance of the solar cell over an FTO-$Cr_{2-x}Mg_xO_3$ anode.

4.6 Band Alignment of the ITO and $Cr_{2-x}Mg_xO_3$ Interface

To map the energy band alignment of an interface requires *in-situ* transfer of samples. Surface properties are immediately modified by adsorbates. From kinetic gas theory one monolayer adsorption occurs for a gas exposure of one Langmuir, which corresponds to one second of exposure to 1×10^{-4} Pa. Any contact with air immediately leads to adsorption layers of hydrocarbons and water. Such exposure does not only affect the work function but can also modify the Band Bending (BB) at the surface [36].

4.6.1 Design of an Ultra High Vacuum Transfer System

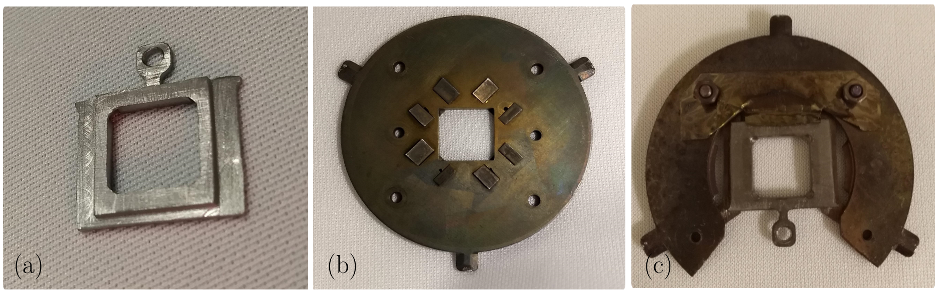

Figure 4.8: (a) Custom XPS sample based on the Omicron design. It has been designed so the back of the substrate will be exposed to the radiative heater which replicates the exact conditions that samples are deposited in the MBE routinely. (b) An unmodified MBE sample holder. (c) Modified MBE which is capable of holding an custom XPS sample holder.

To transfer samples without breaking vacuum required a universal sample holder that is compatible with both the deposition system and the XPS. The deposition system chosen for band alignment was the MBE. The MBE allows precise control of the thickness. The Scientia Omciron XPS has an inflexible sample transfer mechanism. Therefore, the MBE sample holder was modified to

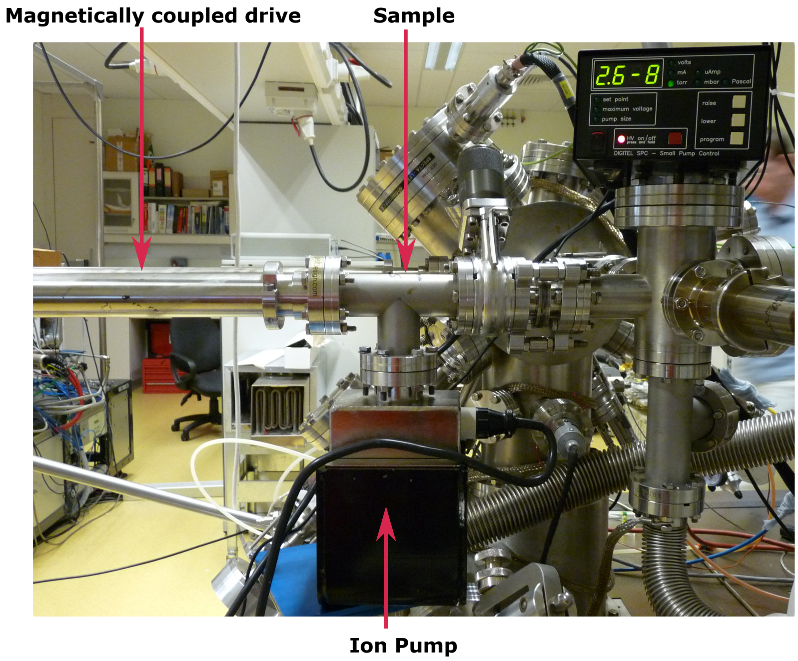

Figure 4.9: Ultra high vacuum sample transfer system attached to the load lock of the XPS system. A Gamma Vacuum Titan Ion pump model 20S (pumping rate 20L/s). The pressure of the transfer system is measured by ion pump controller (top right: $2.6{\times}10^{-8}$ Torr). The sample is held during transfer by the SPECS mechanism which holds an Omicron sample plate. The SPECS mechanism is magnetically coupled to the rotation of the linear drive. A VAT valve (Mini UHV Series 010) seals the transfer system while the load lock is vented to atmosphere, for movement between vacuum chambers.

be capable of holding an XPS sample plate (see figure 4.8 (c)).

To move the sample between chambers a linear and rotary magnetically coupled transfer arm (UHV Design Ltd.) with a SPECS Transfer Tool SH2/12 ISR holds the XPS sample holder. The vacuum of the transfer arm is maintained by a Gamma Vacuum Titan Ion Pump. A UHV compatible valve seals the transfer system, allowing the loadlock of the MBE or XPS to be vented while keeping the sample under vacuum ($\approxeq 2{\times}10^{-6}$ Pa). The pressure within the transfer system's chamber is monitored via the ion pump controller.

4.6.2 Changes in $Cr_{2-x}Mg_xO_3$ with Air Exposure

The necessity of the *in-situ* transfer system was illustrated by depositing 30 nm of $Cr_{2-x}Mg_xO_3$ upon an $Al_2O_3(0001)$ substrate by MBE. The sample was trans-

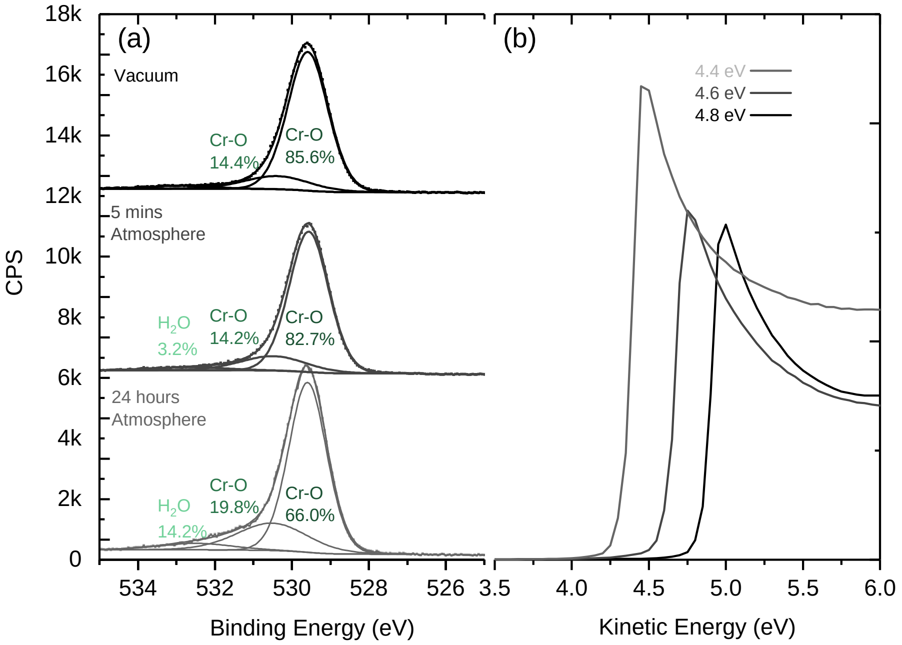

Figure 4.10: O 1*s* changes of $Cr_{2-x}Mg_xO_3$with air exposure

ferred with the UHV transfer system to the XPS. The valence band and core levels were measured via XPS and the work function via UPS. Subsequently, the sample was exposed to atmosphere for 5 mins and re-measured. This was repeated for 24 hours of air exposure at atmosphere. The work function of $Cr_{2-x}Mg_xO_3$ decreases from 4.8 eV to 4.4 eV (figure 4.10 (b)).

The decreasing work function was linked to a change in the O 1*s* core level peak (see figure 4.10 (a)). The O 1*s* peak in bulk $Cr_{2-x}Mg_xO_3$ contains two components at 529.6 eV and 530.5 eV. The binding energy of a third component at 532.7 eV within the O 1*s* peak indicates the presence of water adsorbed on the surface [21]. Water is known to be an electron donor and likely induces the decrease in the work function [37]. To have reliable energy band alignment measurements the presence of these containments must be kept to a minimum by not breaking vacuum when moving a sample from the deposition chamber to the XPS.

Even though this a effect is not ideal for the experimental band alignment of a sample it is a property sought after for gas sensing [38].

4.6.3 Characterisation of ITO

Commercial ITO was supplied from SOLEMS with a carrier concentration of 2.4×10^{21} cm^{-3} and an electron mobility of 52 $cm^2V^{-1}s^{-1}$ measured by Hall effect. Surface preparation was required ahead of band alignment as the ITO is prepared *ex-situ* and loaded into the XPS. The film was sonicated in both acetone and isopropanol for 15 mins in each solvent. The ITO film was heated in vacuum to 623 K for 1 hour to aid removal of any surface adsorbed species. The XP spectra showed carbon was reduced to negligible quantities after this cycle of annealing (see figure 4.11). The In 3*d* peak was fitted using the Casa XPS program. A Shirley background was used and all components were fitted with a Gaussian/Lorentzian (25 %/75 %) product formula. The indium components were modified by an exponential blend, due to the metallic nature of the film.

A fit of the In $3d_{5/2}$ peak cannot be obtained without the second component of In_{II}. In_{I} falls at the expected reference binding energy, 444.8 eV, for ITO. The In_{II} component is well reported as existing in ITO film but the origin is contentious [39]. In_{II} (BE = 445.90 eV) was thought to correspond with amorphous ITO as it is separated for the In_{I} peak by 1.1 eV, which is the reported separation of crystalline versus amorphous indium components in ITO [40]. However, high resolution transmission electron microscopy has not revealed any amorphous regions within the ITO films when these spectral features are observed: both components are now attributed to crystalline ITO [41].

Three oxygen components are contained with the oxygen 1*s* core level in the as received ITO film. O_{III} (BE= 533.1 eV) corresponds to water molecules adsorbed either on the surface or within bulk. This component is removed by vacuum annealing suggesting that the containments were surface adsorbed. The two O 1s components remaining in the vacuum annealed sample are reported in *in-situ* prepared ITO: the origin of the components O_{I} (530.50 eV) and O_{II} (531.90 eV) have previously been separately investigated by Kim et al. and Bourlange et al. It is suggested that two different types of O^{2-} ions exist within the ITO lattice. The

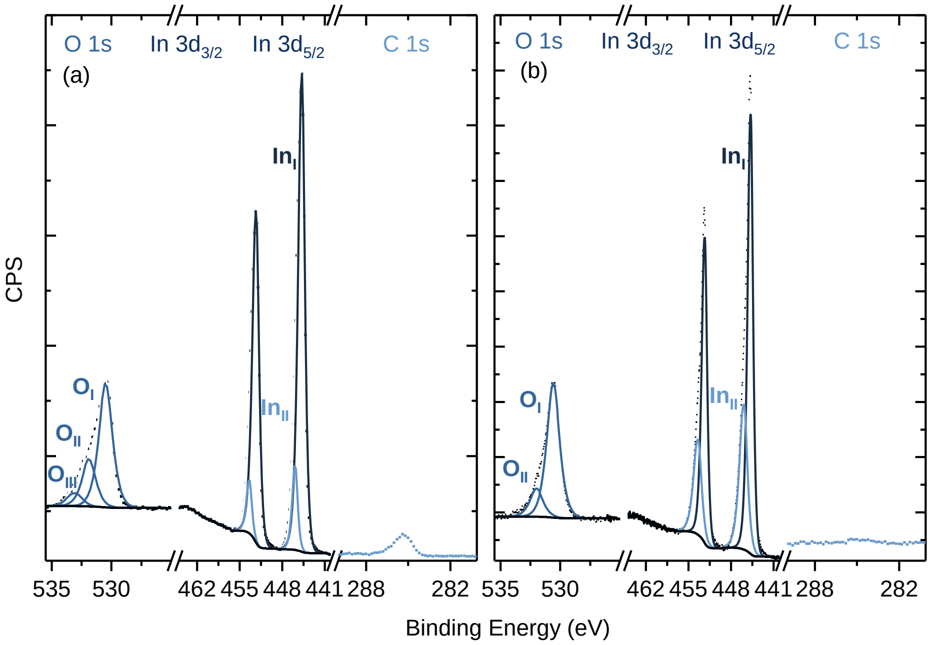

Figure 4.11: (a) In $3d$, O $1s$ and C $1s$ core level XPS peaks of the received ITO film (b) XPS of bulk ITO after vacuum annealing at 673 K for 1 hour to remove any carbon and hydroxide formation [39]

higher binding energy component O_{II} lies at oxygen deficient sites (i.e., they are bonded to In atoms without their full complement of six nearest-neighbour oxygen ions) [42, 44]. However, separately Bourlange et al. attributes the second peak to plasmon losses due to the presence of Sn atoms within the ITO lattice [43]. The origin of the doublet structure within the core level of ITO is not fully resolved however importantly for the band alignment studies it is not a feature of surface contamination.

Work Function and Valence Band

The UP spectra was taken using a sample bias of 5 V. The bias voltage is used to ensure the detection of the complete secondary electron distribution. Work function measurements are sensitive to surface reconstructions, adsorbates, surface termination etc [45]. Hence workfunction measurements should be performed on the sample that band alignment will be carried out on ideally. However, ultraviolet light has been shown to reduce the surface of ITO [46]. As this measurement

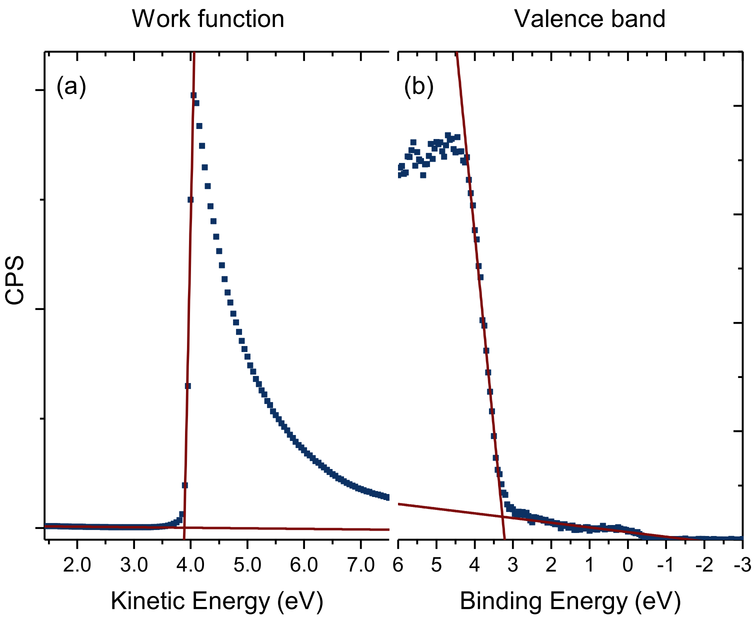

Figure 4.12: (a) UP spectra of the ITO showing the work function of the film to be 3.9+/-0.1 eV. (b) XP spectra of the valence band region. The valence band maximum lies 3.2 eV below the Fermi level.

will not be performed before any anode buffer layer is grown upon ITO in a real device this may alter the band alignment of ITO with $Cr_{2-x}Mg_xO_3$. The work function measurements were performed on a separately prepared surface. The measurement was repeated on several samples to ensure consistency.

The valence band maximum in a vacuum annealed sample lies 3.2 eV below the Fermi level (see figure 4.12 (b)). The position of the valence band maximum can be determined by a number of methods. The Kraut method fits the valence band maximum position using a broaden valence band density of states theoretical calculation to the spectra. This gives a determination of the valence band maximum position with a precision of ± 0.03-0.04 eV [47]. However, Kraut's method was most successful in the determination of valence band maximum of III-V semiconductor interfaces. Chambers and Droubay reported that in oxides the linear method may be more precise due to the complexity of modelling oxides such as $SrTiO_3$ compared with III-V semiconductors. Metal oxides can be modelled using the Kraut method but only with improved, more complex computational methods [22].

Without access to such computations for ITO the linear method was chosen. The linear method requires extrapolation of the leading edge of the valence band while also fitting a line to the background of the valence band. The point of intersection is said to be the valence band maximum. The linear method gives a precision of ≈ ± 0.1 eV. The choice of what range of the leading edge consists of a straight line is the limiting factor in the precision of the linear method.

4.6.4 Growth of $Cr_{2-x}Mg_xO_3$ upon ITO

The high deposition temperature (873 K) and large oxygen partial pressure (5.4×10^{-3} Pa) required for the ideal growth of $Cr_{2-x}Mg_xO_3$ increases the sheet resistance of ITO. The increase in the sheet resistance of ITO at elevated temperatures in a high oxyen partial pressure is likely due to oxygen as an interstitial acting as a double acceptor [48]. A high sheet resistance would increase the series resistance of the solar cell, potentially offsetting the increased efficiency due to the insertion of a hole transport layer. Lowering the oxygen partial pressure could aid in maintaining the sheet resistance of the ITO but this significantly degrades the conductivity of the $Cr_{2-x}Mg_xO_3$. Lowering the deposition temperature to 673 K for $Cr_{2-x}Mg_xO_3$ does not alter the conductivity within the error but maintains the sheet resistance of the ITO (30Ω/□). The magnesium doping was 11.7 % for the $Cr_{2-x}Mg_xO_3$ films. Doping the films with a magnesium concentration of 11-13 % gives the minimum resistivity of $Cr_{2-x}Mg_xO_3$ material in thin film form, which should keep the series resistance of the solar cell low compared with using Cr_2O_3 as a hole transport layer.

Table 4.3: Conductivity of $Cr_{2-x}Mg_xO_3$ grown upon $Al_2O_3(0001)$ as a function of temperature. The oxygen partial pressure was kept constant at 5.4×10^{-3} Pa

Deposition Temp (K)	Mg % (±0.2)	Conductivity Scm^{-1} (± 0.01)
673	9.5	0.04
773	9.8	0.04
873	9	0.03

Band alignment measurements require monitoring the evolution of at least one core level within both films across the interface. For ITO this is a straight forward choice of the In $3d_{5/2}$ and $3d_{3/2}$ peaks which will give the highest signal to noise when attenuation of the core level intensity occurs for increasing coverage of $Cr_{2-x}Mg_xO_3$.

Section 4.3 gives detailed fits for the Cr $2p$ spectra for Cr_2O_3 and $Cr_{2-x}Mg_xO_3$. However, Chambers and Droubay have shown previously that due to the strong broadening and splitting of multiplet interactions the unambiguous assignment of the binding energies is difficult as a function of thickness, particularly in the region of several monolayers when the peak is broadened significantly [22]. The Cr $3s$ peak cannot be resolved below 2 nm. For band alignment the final option is to use the Cr $3p$ peak which is intense enough at low thicknesses but has a less complex peak structure compared to the Cr $2p$ core level.

The Cr $3p$ is multiplet split like the Cr $2p$ but the quantity of this splitting differs due to the smaller radial overlap between the $3p$ and $3d$ orbitals. The peak shape due to multiplet splitting has not been resolved sufficiently and empirical fitting of the Cr $3p$ peak can be performed [26]. However, peak fitting is not required for band alignment as long as no lineshape change is observed across the interface. The reference binding energy for the Cr $3p$ peak in bulk $Cr_{2-x}Mg_xO_3$ is 43 eV (figure 4.14 (a)).

The same procedure that was carried out on ITO was performed to determined the work function of $Cr_{1.76}Mg_{0.24}O_3$ (figure 4.13). The valence band maximum was measured to lie 0.95±0.1 eV below the Fermi level. The work function of $Cr_{1.76}Mg_{0.24}O_3$ was determined 5.5±0.1 eV.

Photoelectron spectra recorded during the interface formation of ITO-$Cr_{1.76}Mg_{0.24}O_3$ are shown in figure 4.15 (a)-(c). Based on the evolution of the core level binding energy for each material the surface potential change across the interface can be determined. The magnitude of the BB is determined from the core level binding energy shift across the interface. It is important that a true shift of the core level is observed and not just a line shape change. Included in the Appendix

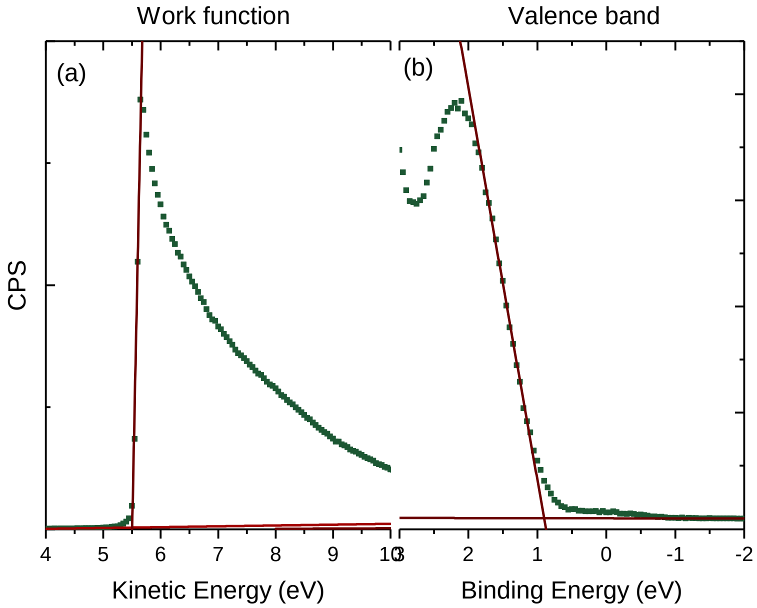

Figure 4.13: (a) UP spectra of $Cr_{2-x}Mg_xO_3$ showing the work function 5.5±0.1 eV (b) XP spectra of the valence band region. The valence band maximum lies 0.95 eV below the Fermi level

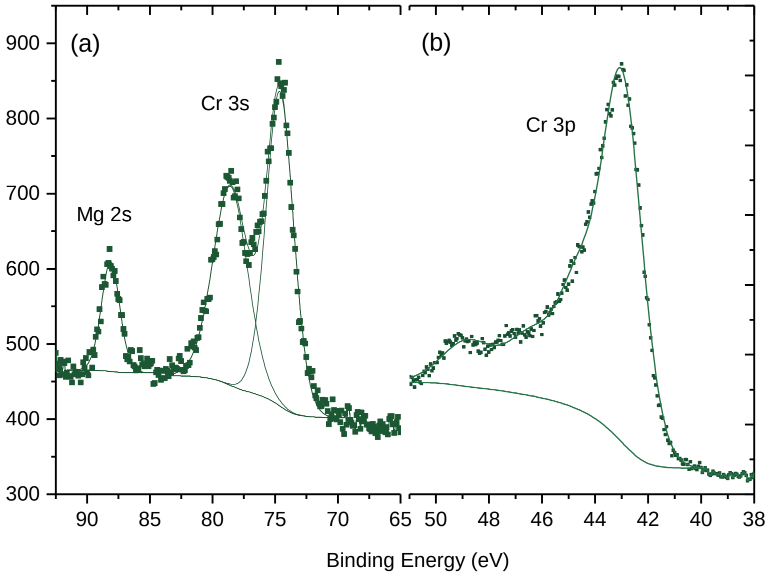

Figure 4.14: (a) Cr 3s and Mg 2s peaks are used to calculate the doping ratio of magnesium to be 11.7 % (b) Cr 3p peak from a $Cr_{2-x}Mg_xO_3$ sample of thickness 30 nm showing the reference peak binding energy of 43 eV.

Band alignment of ITO-$Cr_{1.76}Mg_{0.24}O_3$

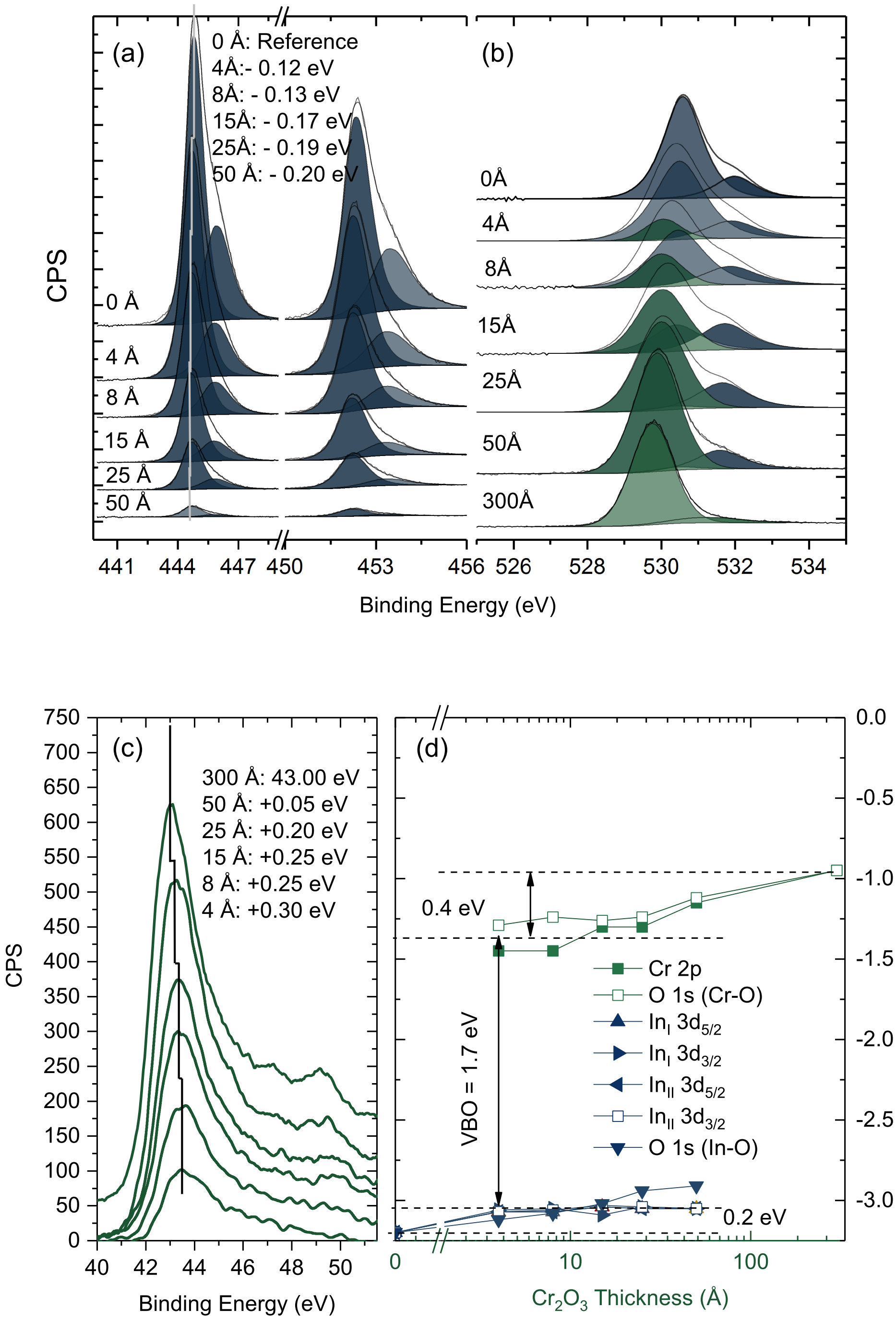

Figure 4.15: Photoelectron spectra of the ITO/$Cr_{1.76}Mg_{0.24}O_3$ interface. The $Cr_{1.76}Mg_{0.24}O_3$ film thickness is indicated in Ångströms. (a) In $3d_{5/2}$ and $3d_{3/2}$ spin orbit split peaks showing a core level shift of 0.2 eV across the interface (b) O 1*s* peak showing the Cr-O and In-O components at intermediate coverage. The same magnitude of core level shift is recorded for the O 1*s* components. (c) A 0.5 eV in the core level is seen in the Cr 3*p* core level. (d) E_f-E_{VBM} calculated from the core level binding energies (a)-(c).

(figure A.1) is the normalised Cr 3*p* peak taken at various thicknesses during the deposition of $Cr_{2-x}Mg_xO_3$ upon ITO. No lineshape change was observed. This shows any shift in the core level binding energy likely originated due to the built in potential at the interface which arose from the diffusion of carriers across the interface.

The lineshape was also monitored in the In $3d_{5/2}$ peak (figure A.2); following the deposition of 4Å of $Cr_{1.76}Mg_{0.24}O_3$ upon ITO there is a reduction in the intensity of the In_{II} component fitted to the In $3d_{5/2}$ peak. No further changes in the lineshape of the In 3*d* peaks are observed for greater thicknesses of the $Cr_{2-x}Mg_xO_3$. Due to the initial lineshape change, the individual components In_I and In_{II} were tracked instead of the overall peak center.

For the substrate the BB is equal to the core level change observed in the film. The BB_{ITO} was found to be 0.2 eV:. This was determined by averaging the core level change seen in the spin orbit split $3d_{5/2}$ and $3d_{3/2}$ components and the In-O component of the O 1*s* core level.

To find the true BB within the deposited film ($Cr_{2-x}Mg_xO_3$) the change in the film's core level has to be subtracted from the induced surface potential change from the substrate (Equation 4.1) over the same thickness regime [49].

$$BB_{\text{film}} = \Delta E_{\text{core level film}} - \Delta E_{\text{core level substrate}} \tag{4.1}$$

The average core level shift in the Cr 3*p* peak and the Cr-O component of the O 1*s* peak across the ITO-$Cr_{1.76}Mg_{0.24}O_3$ interface was 0.4 eV (figure 4.15(c)). Over the same thickness regime (4Å→ 50Å) the average change in the In 3*d* and O 1*s* peaks was 0.1 eV. This is subtracted from the core level shift induced in the deposited film of $Cr_{2-x}Mg_xO_3$ to give a BB of 0.3 eV.

The change in the valence band maximum as function of thickness is shown in figure 4.15. The valence band offset is derived directly from the difference of substrate and film valence band maxima at intermediate thicknesses. The minimum Valence Band Offset (VBO) was 1.7 eV (indicated in figure 4.15 (d)).

4.6.5 Fundamental Band Gap

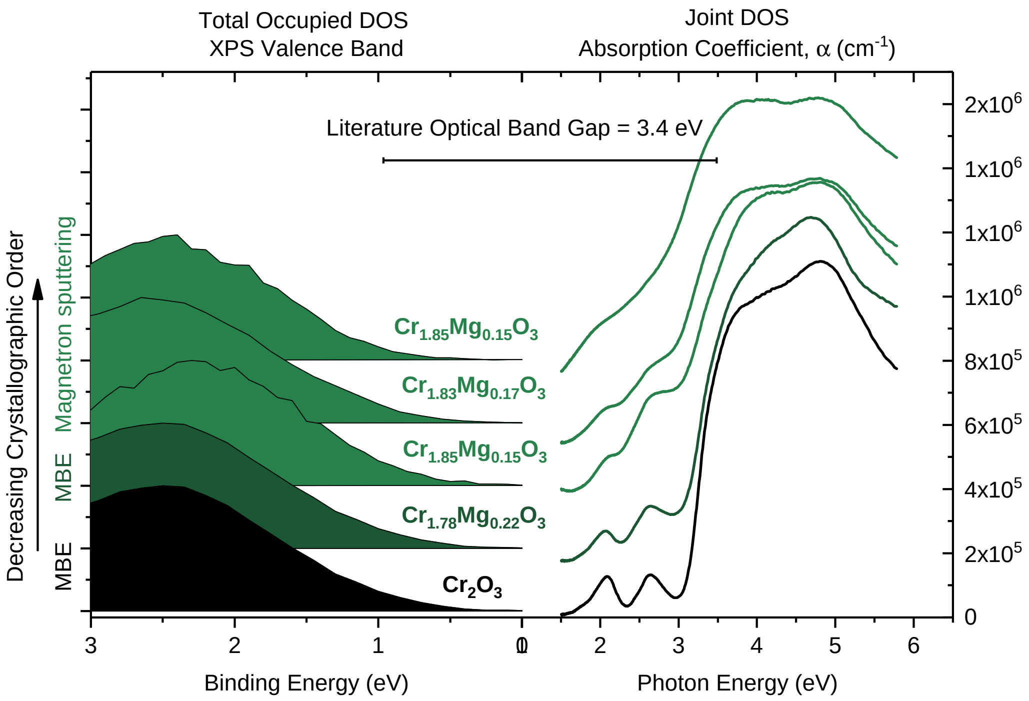

Figure 4.16: The two films, Cr_2O_3 and $Cr_{1.78}Mg_{0.22}O_3$, were grown at a deposition temperature of 873 K on $Al_2O_3(0001)$. The other three films were grown via magnetron sputtering from a ceramic target with a fixed magnesium concentration. The deposition temperature varied from 993 K to room temperature. This created films of varying crystalline quality. The valence band was measured via XPS. The absorption coefficent was calculated from Reflectance and Transmission spectra from UV-Vis. The thickness of the films was measured by XRR.

Using the VBO, the Conduction Band Offset (CBO) can be calculated from Equation 4.2. Reference values for the band gap are usually taken from the literature.

$$\text{CBO} = \text{Band gap}_{\text{film}} + \text{VBO} - \text{Band gap}_{\text{substrate}} \tag{4.2}$$

However, it is important to note that the onset of strong optical absorption (optical band gap) is not necessarily equivalent to the minimum gap between the conduction band and valence band. This is crucial particularly for the band alignment of the ITO/$Cr_{2-x}Mg_xO_3$ interface as one of the roles of $Cr_{2-x}Mg_xO_3$ is to create a Conduction Band Offset (CBO) between the anode and active layer in an organic solar cell. Using the fundamental band gap versus the optical band gap will change the CBO.

In 2008, Walsh *et al.* showed that the fundamental band gap of In_2O_3 is 2.9 eV [50]. The valence band states leading to the direct optical transition of 3.75 eV lay 0.8 eV below the valence band maximum. The fundamental band gap of ITO is reduced to 2.7 eV due to band gap re-normalisation [48, 51].

A similar issue has arisen in Cr_2O_3 and $Cr_{2-x}Mg_xO_3$. The onset of absorption/optical band gap for Cr_2O_3 is well reported as 3.4 eV, but often assumed to be equivalent to the band gap [52, 53]. However, when the absorption coefficient is measured for Cr_2O_3 and $Cr_{2-x}Mg_xO_3$ thin films it shows optical absorption features that lie below 3.4 eV. Their origin was thought to arise from either *d*-*d* dipole forbidden transitions or defect states [8].

Calculating the Absorption Coefficient

To acquire the absorption coefficient (α) of a thin film the transmittance (T) and reflectance (R) spectra of the material is taken by UV-Vis spectroscopy. The absorptance of a material is then be related to the transmittance and reflectance by the following relation:

$$T + R + A = 1 \tag{4.3}$$

Utilising the Beer Lambert law the absorption coefficient can then be approximately related to T and R by the following equation:

$$\alpha = \frac{-ln(T+R)}{t} \tag{4.4}$$

where t is the thickness of the thin film being analysed. The thickness of a thin film was measured precisely by X-Ray Reflectivity (XRR).

A 113 nm film of Cr_2O_3 on Al_2O_3 grown by MBE and matches the literature reports that the onset of strong optical absorption occurs at a photon energy

3.4 eV (see figure 4.16). Epitaxial films of $Cr_{2-x}Mg_xO_3$ (119 nm) deposited upon Al_2O_3 by MBE show the onset of absorption to decrease to 3.3 eV. Additionally however, epitaxial Cr_2O_3 and $Cr_{2-x}Mg_xO_3$ films in figure 4.16 show distinct optical absorption features at 2.1 eV and 2.7 eV below the optical band gap. It is possible that the magnesium doping of the $Cr_{2-x}Mg_xO_3$ lattice creates defect states which leads to sub band gap absorption of light [54]. However, the sharpest defined absorption features below the band gap occur for epitaxial Cr_2O_3 thin films.

Reproducing the origin of the band gap for transition metals by modelling is currently still an issue for theoreticians due to the fact that Density Functional Theory (DFT) describes ground state properties and fails to predict electron-electron correlation in excited states appropriately.

The initial theoretical calculations by Catti *et al.* using the periodic unrestricted Hartee-Fock over estimated the band gap at greater than 15 eV [8]. Using Local Density Approximation (LDA) functionals predicted a band gap for Cr_2O_3 of approximately 1.5 eV [55]. To more accurately predict the electronic structure of Cr_2O_3 DFT+U has been adopted. U is the Hubbard parameter and accounts for on-site Coulomb interactions of localised electrons.

The most recent calculations for Cr_2O_3 have applied a range of values for the U parameter and compared with experimental photoemission valence band spectra. This produced a range of values for the band gap (2.8-3.4 eV) [17, 56, 57] with no states calculated to lie below the optical band gap. Optical modelling of Cr_2O_3 has shown though that two optically allowed transitions exist at photon energies 2.1 eV and 2.7 eV [58]. The origin of these transitions is not fully resolved. However, it is clear that optical modelling and experimental absorption spectra indicate that the fundamental band gap is not 3.4 eV.

We have collaborated with the Condensed Matter Theory group in Trinity College Dublin who recently have reported a method of self consistent method to solve for U and J [59]. Using the U, J that were found from first principles the

Table 4.4: Density functional calculations using LDA xc-functional and PAW pseudopotential for the Cr_2O_3 lattice. The experimental value for the magnetic moment of Cr_2O_3 is 2.8 μB [60].

	Band Gap (eV)	Magnetic Moment (μB)
LDA	1.27	2.30
LDA + U	2.09	2.56
LDA + U + J	2.06	2.59

fundamental band gap was calculated to be 2.1 eV (see Appendix B.1 for further details).

For this work, it will be assumed that a fundamental band gap of 2.1 eV holds for $Cr_{2-x}Mg_xO_3$. This value will be used to determine the CBO that should exist between the ITO and $Cr_{1.76}Mg_{0.24}O_3$ interface.

4.6.6 Energy Band Diagram of ITO - $Cr_{1.76}Mg_{0.24}O_3$

Using the experimentally determined VBO, CBO, BB and work function values the energy band alignment of ITO-$Cr_{1.76}Mg_{0.24}O_3$ can be mapped. The theoretical alignment of p-type $Cr_{2-x}Mg_xO_3$ with n-type ITO by Anderson's rule would predict a VBO offset of 0.65 eV and a CBO of 0.15 eV (figure 4.18 (b)). It assumes the CBO between two materials will be given by the difference in electron affinity. The magnitude of the built-in potential is assumed to be equal to the difference in the two vacuum levels of the two surface brought into contact [61]. With such a small theoretical predicted CBO it could be disregarded as an appropriate ABL for solar cells where ITO is the anode.

However, this is considerably smaller than the experimentally determined values of VBO of 1.7 eV and CBO of 0.9 eV. The electron barrier created between the conduction band minimum of $Cr_{2-x}Mg_xO_3$ and the fermi level of ITO and Type II band alignment determined experimentally would indicate the ITO–$Cr_{2-x}Mg_xO_3$ interface to be useful as an electron blocking layer. To investigate if it aids hole transport the valence band offset between $Cr_{2-x}Mg_xO_3$ and active layer would have to be investigated.

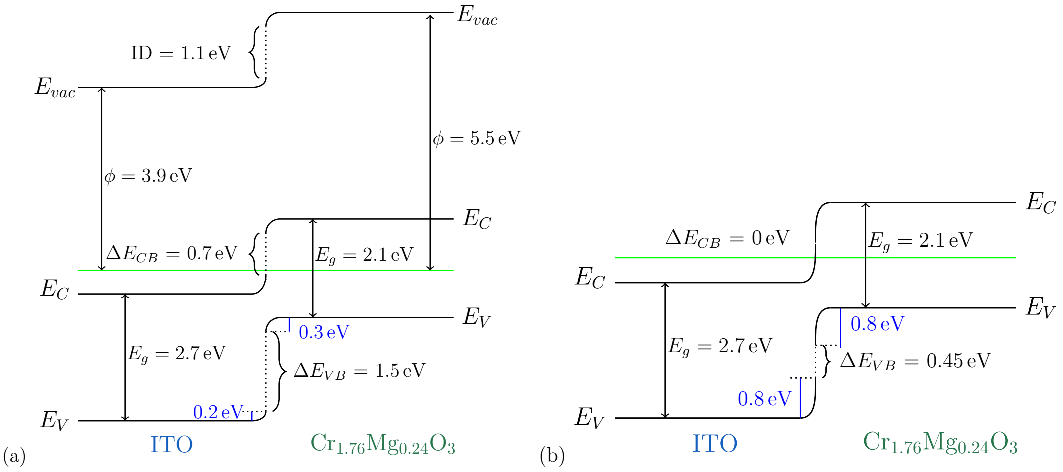

Figure 4.17: (a) Experimentally determined energy band diagram (b) Energy band diagram predicted by Anderson's rule [61]. The work function for ITO and $Cr_{1.76}Mg_{0.24}O_3$ were assumed to be the same values as determined for the energy band alignment studies by UPS. E_c = conduction band minimum, E_v = valance band maximum, E_g = fundamental band gap, WF= workfunction, ΔE_{vb} = valance band offset , ΔE_{cb} = conduction band offset, Fermi level is denoted as the green line.

4.6.7 Comparing the Alignment of $Cr_{2-x}Mg_xO_3$ as an Anode Buffer Layer with Two Choices of Anode

As discussed in Section 4.5.1, an organic cell (figure 4.7) with FTO as the anode showed there was only a marginal increase in the efficiency when $Cr_{2-x}Mg_xO_3$ was used in place of Cr_2O_3 as the Anode Buffer Layer (ABL). This was initially surprising as using $Cr_{2-x}Mg_xO_3$ in place of Cr_2O_3 within the cell decreased the series resistance. When the band alignment of FTO-$Cr_{2-x}Mg_xO_3$ (see figure 4.18 (b)) was mapped, it became apparent it forms a Type III (broken gap) heterojunction, which likely leads to it being ineffective as an ABL. The FTO-$Cr_{2-x}Mg_xO_3$ band alignment is taken from an unpublished paper by Mullarkey et al. The conclusion made was neither Cr_2O_3 nor $Cr_{2-x}Mg_xO_3$ is appropriate as an ABL when using FTO as the anode.

It often occurs that the ABL layer should be switched out for an alternative material if it does not improve the efficiency of the solar cell and the anode is kept. However when comparing the band alignment of FTO and ITO with $Cr_{2-x}Mg_xO_3$ it becomes apparent that the combination of anode and ABL is vitally important.

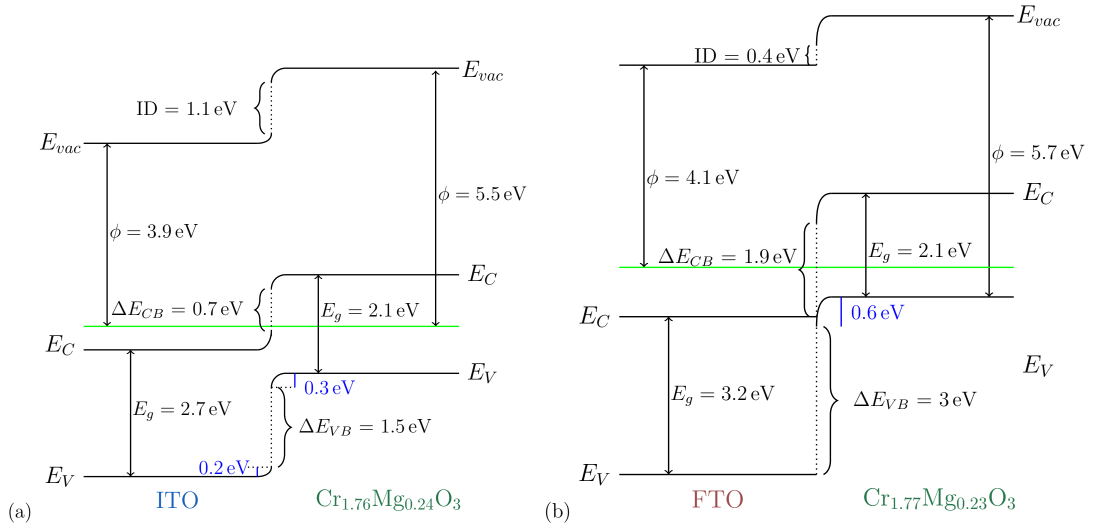

Figure 4.18: Energy band alignment of (a) ITO with $Cr_{1.76}Mg_{0.24}O_3$and (b) FTO with $Cr_{1.77}Mg_{0.23}O_3$. E_c = conduction band minimum, E_v = valance band maximum, E_g = fundamental band gap, WF= workfunction, ΔE_{vb} = valance band offset , ΔE_{cb} = conduction band offset, Fermi level

Due to the rarity of p-type TCOs, the replacement of the anode material for one better aligned to the ABL could also be a viable option.

However, p-type $Cr_{2-x}Mg_xO_3$ is used a passive element within the solar cells as an ABL. This work would like to incorporate $Cr_{2-x}Mg_xO_3$ as active element within a device. The capabilities of an *in-situ* transfer system developed here to facilitate the energy band alignment measurements, could extend the possible use of $Cr_{2-x}Mg_xO_3$ by optimising it's interface with alternative materials in the future.

4.7 Transparent diodes: Engineering Rectifying Behaviour

In fact, another application explored was the use of $Cr_{2-x}Mg_xO_3$ within transparent rectifying diodes. As previously outlined homojunctions are preferable due to the fact that there should be less complications due to large lattice mismatches and electrical conductivity differences [62]. However, as of yet, Tin Oxide and Zinc Oxide homojunctions have relatively low on/off ratios of 10^3 [63]. In fact the highest on/off ratio has been borne by the heterojunction NiO/ZnO [64]. NiO is only semitransparent with the visible optical spectrum. p-type $Cr_{2-x}Mg_xO_3$ has improved transparency over NiO, therefore a more appropriate material for transparent diodes. Arca et al. reported that $Cr_{2-x}Ni_xO_3$ and aluminium doped ZnO (AZO) did not show rectifying behaviour due to the high carrier density of both $Cr_{2-x}Ni_xO_3$ and AZO [4]. By lowering the carrier concentration using intrinsically doped zinc oxide it was theorised a larger built in potential could be created, producing rectifying behaviour. These next sections will explore if a rectifying transparent diode can be engineered.

4.7.1 Deposition of $Cr_{2-x}Mg_xO_3$ on ZnO

The zinc oxide films used within this work were deposited by magnetron sputtering, Section 3.7 outlines an in-depth discussion on magnetron sputtering. The films were deposited at a temperature of 993 K upon $Al_2O_3(0001)$ from a ceramic ZnO target.

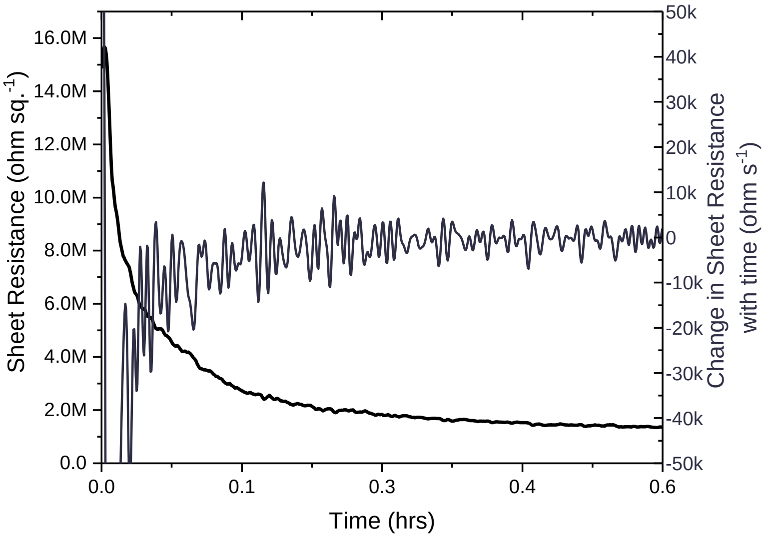

Figure 4.19: Sheet resistance of ZnO films versus time as the film was annealed at 693 K in a nitrogen atmosphere

The as-deposited ZnO films have sheet resistances in excess of 200 MΩ/□. ZnO films were nitrogen annealed (1 atm) *ex-situ* at 593 K. The sheet resistance

Table 4.5: Ideality factor (η) of the heterojunction of ZnO-$Cr_{1.82}Mg_{0.18}O_3$ as function of temperature using the Shockley diode equation 4.6. The ideality fact was determined between a forward bias of 0.5 V and 0.75 V. The on/off current ratio values were taken at a bias of 1.5 V.

Temperature (K)	η	On/Off Ratio
300	12.46	1×10^3
280	11.07	1×10^3
260	10.4	5×10^3
240	10.50	1×10^4
220	8.59	2×10^4
200	6.8	5×10^5

was monitored as the film was annealed (see figure 4.19), once the sheet resistance plateaued at a fixed value the film was cooled to room temperature within a nitrogen atmosphere. The sheet resistance of zinc oxide ranged between 200-300 kΩ/□ deposited at the same temperature of 973 K.

The role of the nitrogen annealing on improving the conductivity within ZnO either faciltates activation of intrinsic donor sites, e.g, V_O or passivates the grain boundaries [65]. No detectable nitrogen incorporation is seen within XPS nor is any change in the Zn 2*p* core level observed.

It was apparent though that vacuum annealing above 573 K reversed the effects of the nitrogen annealing and the films became insulating, suggesting grain boundary passivation is the main effect in these ZnO films. This limited the quality of $Cr_{2-x}Mg_xO_3$ films that could be deposited as a high temperature (873 K) and large oxygen partial pressure (5.4×10^{-3} Pa) is required for the optimum grow conditions. Room temperature deposition of $Cr_{2-x}Mg_xO_3$ had to be optimised as the magnesium incorporation within the films is highly sensitive to the deposition temperature. The doping concentration of samples were calibrated by measuring the atomic ratio of Mg and Cr by XPS using the Mg 2*s* and Cr 3*s* peaks.

Figure 4.20 (b) shows an XRD measurement of the ZnO-$Cr_{1.82}Mg_{0.18}O_3$ heterojunction. The ZnO films grew with a wurtzite structure that is textured along the (002) axis. The absence of any reflex associated with Cr_2O_3 indicates that it is likely amorphous, as would be expected for room temperature deposition.

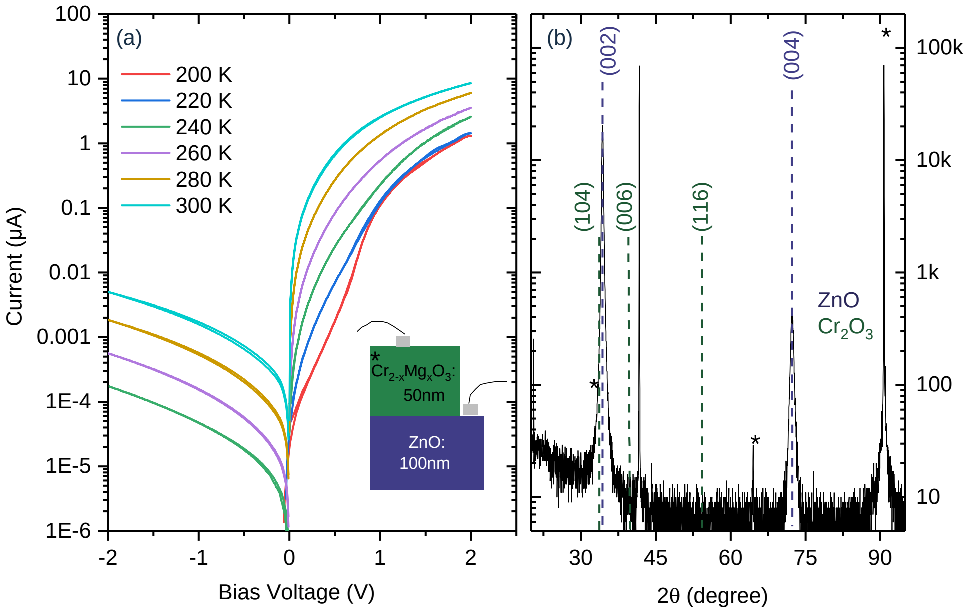

Figure 4.20: (a) Semilog plot of *IV* characteristics of p-type $Cr_{1.82}Mg_{0.18}O_3$ deposited at room temperature on n-type ZnO (b) X-ray diffraction symmetric $\theta/2\theta$ scan of $Cr_{2-x}Mg_xO_3$ deposited at room temperature upon zinc oxide. The zinc oxide film is textured along the (002) axis. No reflexes are observed from $Cr_{2-x}Mg_xO_3$ as it is deposited at room temperature, so is likely amorphous.

The heterojunction was fabricated by a physical shadow mask placed over half the ZnO film and depositing the p-type $Cr_{2-x}Mg_xO_3$ layer. Electrical properties of the stack were probed by placing silver contacts either side of the junction. The convention established was that the forward bias denoted a positive bias applied to the p-type $Cr_{1.82}Mg_{0.18}O_3$ layer.

Contacts

The contacts to both the ZnO and $Cr_{2-x}Mg_xO_3$ thin films were confirmed to be non-rectifying in origin, see figure 4.21.

IV characteristics

The *IV* characteristics of the diode as a function of temperature are contained within figure 4.20 (a). The diode exhibited clear rectifying behaviour. The *IV* curve shows the current increases at higher temperatures due to the fact that

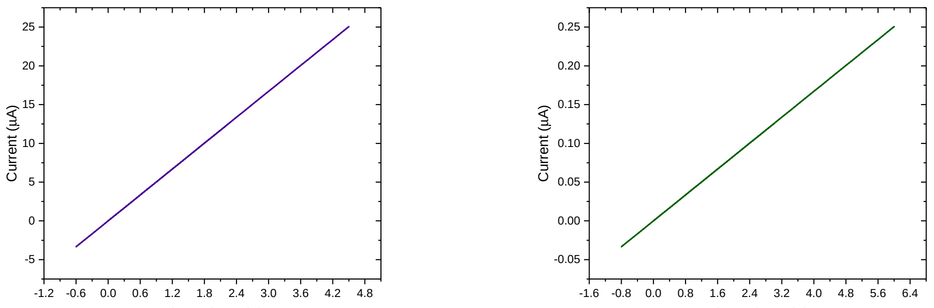

(a) (b)

Figure 4.21: (a) Ohmic contact of Zinc oxide films deposited at 993 K with silver wire contacts (b) Ohmic contacts of $Cr_{2-x}Mg_xO_3$ depoisited at 873 K with silver wire contacts

more carriers can diffuse across the interface. The diode produced an on/off ratio of approximately 10^3 determined by taking a ratio of the current values at 1.5 and -1.5 V at 300 K. This is competitive with some epitaxial heterojunctions, which is remarkable considering that here the p-type oxide is deposited at room temperature [66]. The ideality factor (η) of the diodes can be estimated using the Shockley diode equation [67]:

$$I = I_s e^{\frac{qV}{\eta k_B T}} \tag{4.5}$$

where I_s is the reverse saturation current, I is the forward biased current, q ia the elementary charge, V is the applied voltage, and T is the temperature that the IV curve is measured at. The Shockley diode equation can be rewritten as follows:

$$\eta = \frac{q}{k_b T} \frac{dV}{d \ln I} \tag{4.6}$$

The thermal voltage $V_i = k_b T / q$ multiplied by the slope of the graph in figure 4.20 (a) will give the value of the ideality factor. The ideality factor is a measure of the rate of change in curvature of a semilog plot of I versus V. It can easily be observed that in figure 4.20 (b) the diode has no linear region, so the ideality factor will be far greater than one. The ideality factor between a voltage of 0.5 and 0.75 V is calculated to be between seven and thirteen depending

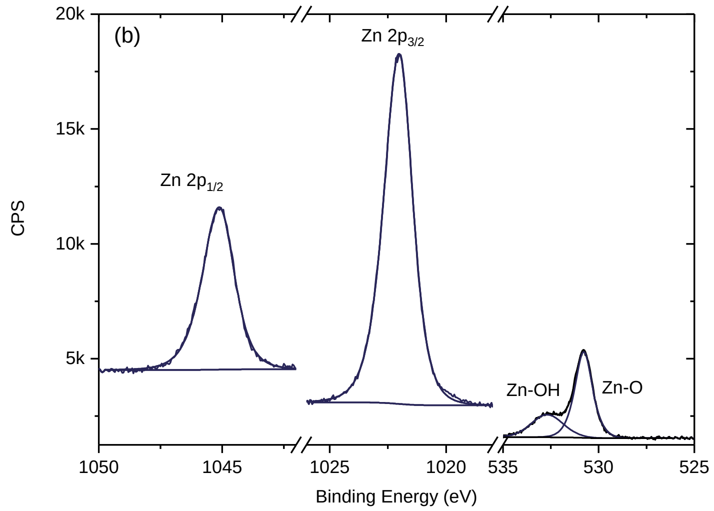

Figure 4.22: XP spectra of the Zn 2p and O 1s core level of ZnO post nitrogen annealing

on the temperature that the IV characteristic was taken at, see Table 4.5. The Sah-Noyce-Shockley theory cannot account for ideality factors greater than 2 [68]. Such high ideality factors have been observed in other oxide diodes previously due to cation mixing at the interface [69]. However, this seems unlikely within this work as the $Cr_{2-x}Mg_xO_3$ films are deposited at room temperature. Understanding the origin of the rectifying behaviour, high ideality factor and how to further optimise the properties of the diode is investigated by mapping the energy band alignment of the interface.

4.7.2 Energy Band Alignment of ZnO and $Cr_{2-x}Mg_xO_3$

XP spectra of the nitrogen annealed ZnO films are shown in figure 4.22. The Zn 2p spin orbit peaks showed no spectral changes with nitrogen annealing, the samples were charge compensated in the pre-annealed state due to the insulating nature of the films. The binding energy of the Zn 2p core level was 1022.15 eV, which is higher than expected for the bulk value of ZnO. The binding energy is consistent with some hydroxide formation on the surface [20]. Indeed, the O 1s had two components, one of which indicated some hydroxide formation on the surface (BE=532.35 eV). However, any vacuum annealing to remove adsorbates

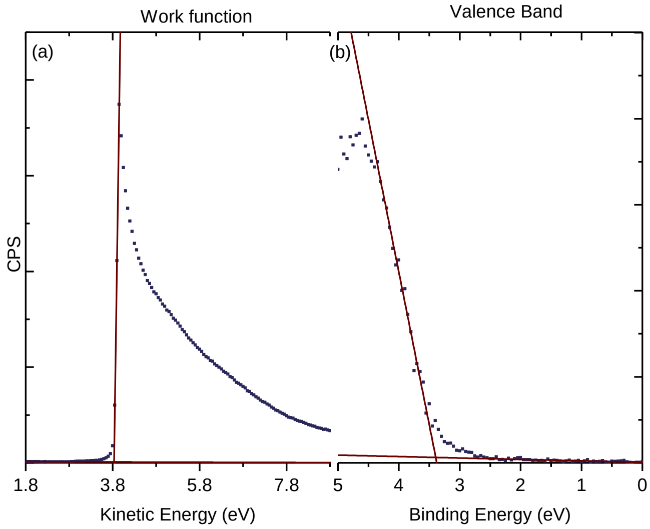

Figure 4.23: (a) UP spectra of ZnO showing the work function of the film to be 3.9+/-0.1 eV. (b) XP spectra of the valence band region. The valence band maximum lies 3.4 eV below the Fermi level.

increased the resistivity of the ZnO film. The energy band alignment was therefore performed on the as received film. As a result the energy band alignment contained within this work may not fully reflect the true alignment of the interface grown in vacuum but nevertheless will give a strong indication of the VBO and CBO offsets.

UP spectra determined the work function of ZnO to be 3.8±0.1 eV with the sample was biased by 5 V. The valence band spectra from XPS determined the VBM to lie 3.4±0.1 eV below the Fermi level. The linear method was used to determine the value of the VBM and work function.

This was repeated from the $Cr_{1.82}Mg_{0.18}O_3$ film. The VBM lay 0.7±0.1 eV below the Fermi level. The work function was determined to be 5.7±0.1 eV. The binding energy of Zn 2*p*, Cr 3*p* and O 1*s* core levels were monitored as a function of $Cr_{2-x}Mg_xO_3$ film thickness. The Cr 3*p* core level showed a binding energy shift of 0.3 eV (see figure 4.24 (c)).

The Zn 2*p* core level shifted by an absolute value of 0.5 eV. However as the $Cr_{2-x}Mg_xO_3$ film thickness increased above 25Å the Zn 2*p* core level shifted back to the bulk reference value of 1022.15 eV. The oxygen peak shifted by the same

Band Alignment of ZnO-$Cr_{1.82}Mg_{0.18}O_3$

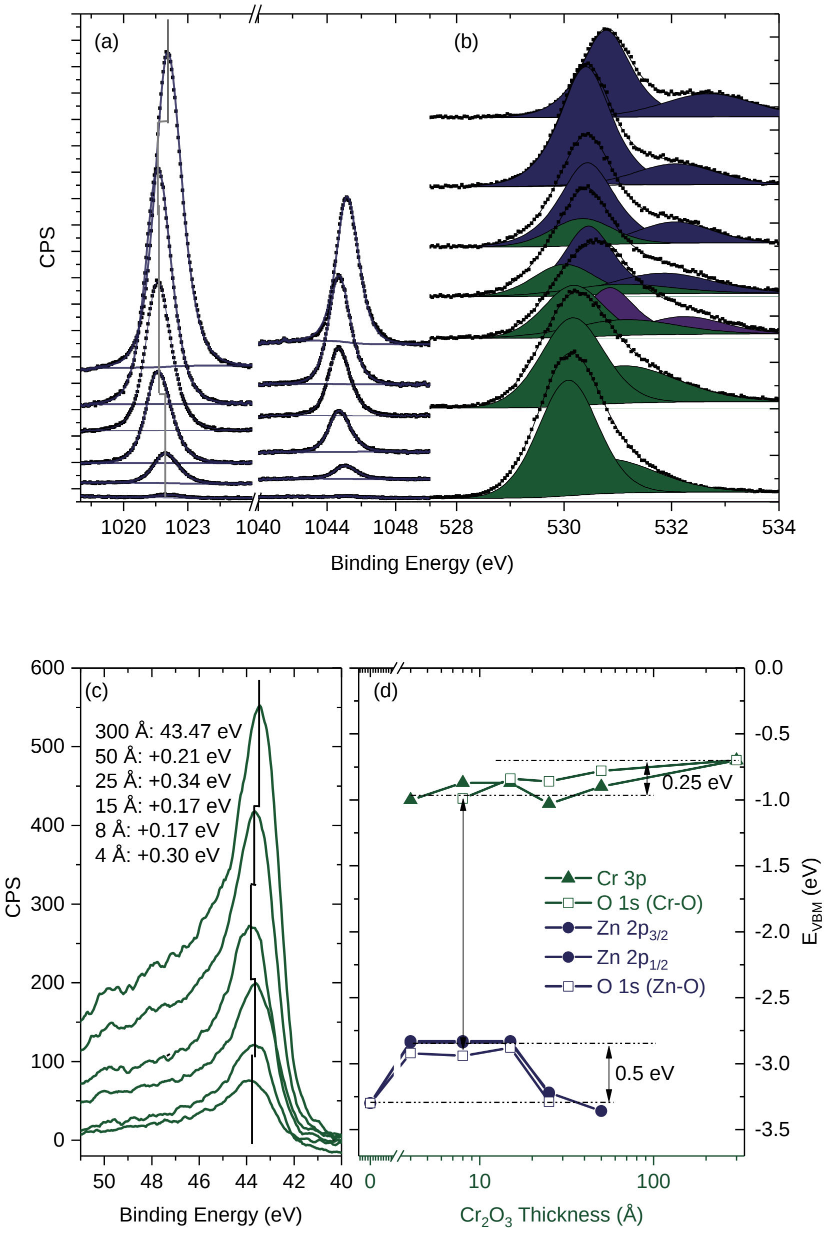

Figure 4.24: Photoelectron spectra of the interface ZnO/$Cr_{1.82}Mg_{0.18}O_3$. The $Cr_{1.82}Mg_{0.18}O_3$ film thickness is indicated in Ångströms. (a) Zn $2p_{3/2}$ and $2p_{1/2}$ spin orbit split peaks show an absolute core level shift of 0.5 eV across the interface (b) O 1*s* peak showing the Cr-O and Zn-O components at intermediate coverage. The same magnitude of core level shift is recorded for the O 1*s* components. (c) A 0.3 eV change in the core level binding energy is observed in the Cr 3*p* core level. (d) E_f-E_{VBM} calculated from the core level binding energies (a)-(c).

magnitude. No lineshape changes in the zinc core levels were observed to explain this shift at the interface (see Appendix A.2).

Inconsistent movement of core levels peaks has been observed at other oxide interfaces, the origin of which can arise from strong BB due to the polarizability of one film, adsorbates producing surface states that do not reflect the bulk properties, and chemical bonding at the interface, among others [36, 49, 70]. Any of these possibilities could explain the observations seen in figure 4.24 (a), more insight can be provided by changing the deposition conditions. The quantity for adsorbates at the interface will vary if the experiment is repeated, changing the magnitude of the shift at the interface. The ZnO-$Cr_{1.82}Mg_{0.18}O_3$ interface was re-grown but exactly the same inconsistent shifting was observed. The chemical bonding at the interface will vary with deposition temperature. While strong band bending due to the polarizability of one film will vary if the extrinsic doping of the $Cr_{2-x}Mg_xO_3$ film is changed. As deposition above room temperature is not possible changing the extrinsic doping of $Cr_{2-x}Mg_xO_3$ was investigated.

The energy band alignment between ZnO and $Cr_{2-x}Mg_xO_3$ films substitutionally doped with 2.3 % and 17 % of magnesium showed the core level peaks in zinc oxide always initially shifted to a lower binding energy by 0.4 and 0.5 eV but above 25Å film thickness of $Cr_{2-x}Mg_xO_3$ the Zn $2p$ shifted back to a higher binding energy. Figure 4.25 shows the changes in the position of the valence band maximum based on the core level changes for a low and high extrinsic doping of the Cr_2O_3 lattice. The magnitude of this effect seen within the zinc oxide films was then independent of the extrinsic doping of the $Cr_{2-x}Mg_xO_3$ films.

This indicates the most likely origin for the inconsistent shift of the core levels is a large quantity of defects created at the interface due to the room temperature deposition of $Cr_{2-x}Mg_xO_3$. The high ideality factor of the diodes correlates strongly with this result.

Even though the origin of the inconsistent band bending in ZnO has been pinpointed, this still makes determining band bending within the $Cr_{2-x}Mg_xO_3$

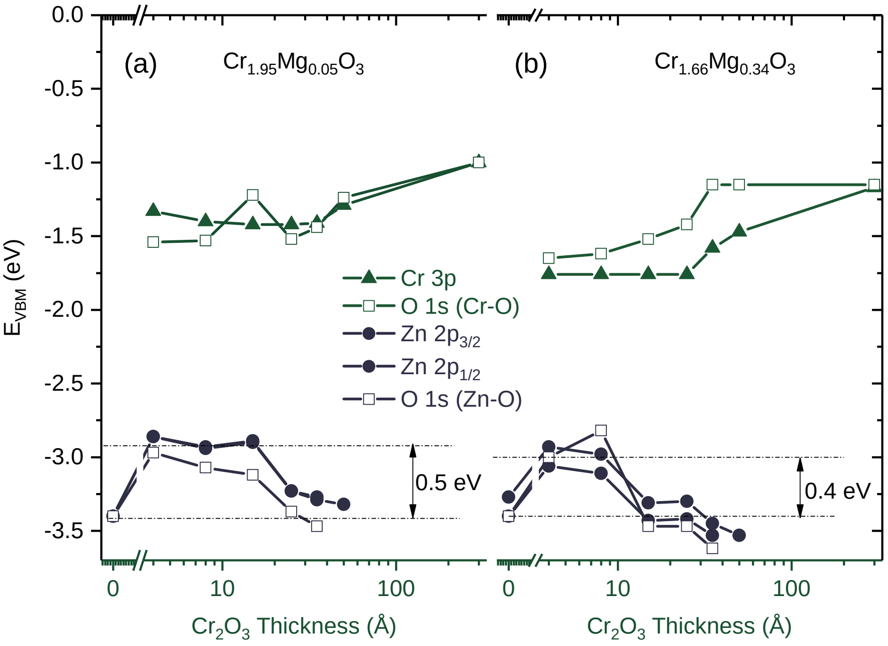

Figure 4.25: (a)E_{VBM}-E_f fo the interface of $Cr_{1.95}Mg_{0.05}O_3$ (b) E_{VBM}-E_f fo the interface of $Cr_{1.66}Mg_{0.34}O_3$

films complicated. As mentioned when mapping the ITO-$Cr_{2-x}Mg_xO_3$ interface, the change in the films core level ($Cr_{2-x}Mg_xO_3$) has to be subtracted from the induced surface potential change from the substrate (Equation 4.1) over the same thickness regime [49]. However, in the case of the inconsistent band bending of the substrate it is not clear what is a true shift in the core levels due the diffusion of carriers across the interface. It is noted that between a $Cr_{2-x}Mg_xO_3$ thickness of 4Å and 15Å no change in the Zn 2*p* core level is seen at any of the interfaces made with $Cr_{2-x}Mg_xO_3$ films. Any core level of Cr 3*p* over this thickness regime is taken as a true band bending within the film. However, the core level changes within the $Cr_{2-x}Mg_xO_3$ films seen over the larger range of thickness values cannot be verified without reversing the stacking, i.e, depositing the ZnO upon a substrate of $Cr_{2-x}Mg_xO_3$. This could not be performed yet due to the lack of facilities to transfer *in-situ* between the magnetron sputtering system.

The VBO was taken to be the minimum value determined between the interface of ZnO and $Cr_{2-x}Mg_xO_3$. The literature value for the ZnO optical band gap (3.3 eV) is the reported fundamental band gap between the CBO and VBO [65].

$$\mathrm{CBO} = \mathrm{Band\ gap}_{\mathrm{film}} + \mathrm{VBO} - \mathrm{Band\ gap}_{\mathrm{substrate}} \tag{4.7}$$

$$\mathrm{CBO} = 2.1\ \mathrm{eV} + \mathrm{VBO}_{\mathrm{minimum}} - 3.3\ \mathrm{eV} \tag{4.8}$$

With these parameters the energy band diagram can be mapped for $Cr_{2-x}Mg_xO_3$-ZnO interfaces as the magnesium concentration changes. For all interfaces between ZnO and $Cr_{2-x}Mg_xO_3$ films the energy band diagrams, shown in figure 4.26, indicate the CBO is much smaller than the VBO. Therefore, electrons should be the dominant carriers under forward bias.

The threshold voltages for this diode was ≈ 0.1 V (see figure 4.20 (a)). The low threshold voltages, large ideality factors and inconsistent band bending contained within the ZnO film suggest the interface states strongly influence the behaviour of the diodes [**Mishra2007**]. However, there is little that can be changed at the $Cr_{2-x}Mg_xO_3$-ZnO interface to improve this. One solution could be to explore the deposition of the $Cr_{2-x}Mg_xO_3$-ZnO stack reversed, i.e, the p-type layer will be deposited first. The ZnO films can be annealed in a nitrogen atmosphere after the deposition of the n-type layer upon $Cr_{2-x}Mg_xO_3$. For these studies the effects of nitrogen annealing upon the $Cr_{2-x}Mg_xO_3$ layer will have to be investigated. Also the *in-situ* transfer of samples between the magnetron sputtering system and XPS will have to be developed so the interface properties by band alignment can be investigated.

The most likely fruitful outlook is to seek out an alternative low carrier concentration n-type conducting oxide. The band alignment of the ITO-$Cr_{2-x}Mg_xO_3$ would indicate that In_2O_3 could be an appropriate candidate material. In_2O_3 can withstand higher deposition temperatures, producing a less defective interface which could increase the ideality factor and performance of the resultant

Energy Band Diagrams at the Interface of ZnO-Cr$_{2-x}$Mg$_x$O$_3$

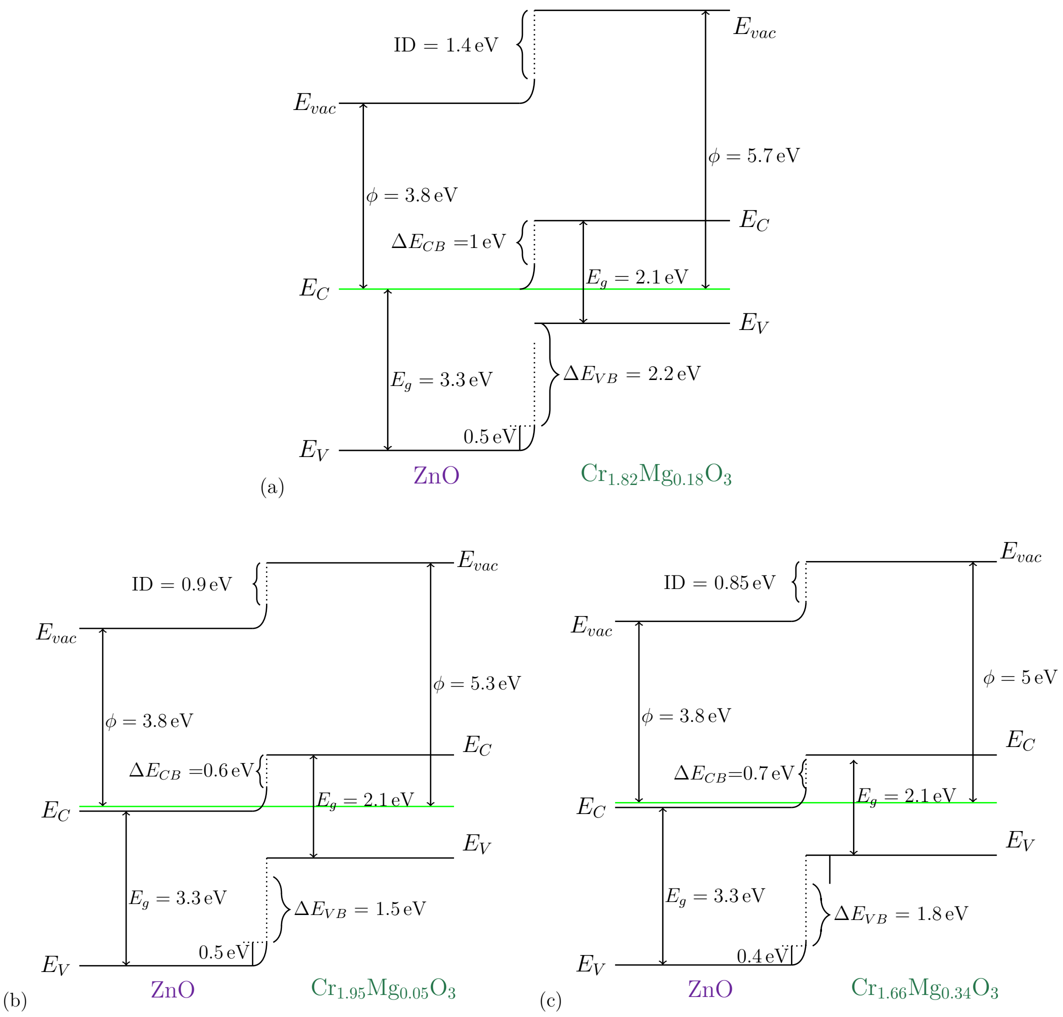

Figure 4.26: Energy band alignment for (a) the optimum magnesium doping of Cr$_{2-x}$Mg$_x$O$_3$ (b) the low extrinsic doping of Cr$_{2-x}$Mg$_x$O$_3$ and (c) a higher extrinsic doping of Cr$_{2-x}$Mg$_x$O$_3$. E_c = conduction band minimum, E_v = valance band maximum, E_g = fundamental band gap, WF= workfunction, ΔE_{vb} = valance band offset , ΔE_{cb} = conduction band offset, Fermi level

diodes.

Bibliography

[1] RF Huang, Anil K Agarwal, and Harlan U Anderson. “Oxygen Activity Dependence of the Electrical Conductivity of Li-Doped Cr_2O_3”. *Journal of the American Ceramic Society* 67.2 (1984), 146–150.

[2] Arve Holt and Per Kofstad. “Electrical conductivity and defect structure of Mg-doped Cr_2O_3”. *Solid State Ionics* 100 (1997), 201.

[3] E. Arca, K. Fleischer, and I. V. Shvets. “Magnesium, nitrogen codoped Cr_2O_3: A p-type transparent conducting oxide”. *Appl. Phys. Lett.* 99.11 (2011), 111910.

[4] Elisabetta Arca, Michael A McInerney, and Igor V Shvets. “Band alignment at the interface between Ni-doped Cr_2O_3 and Al-doped ZnO: implications for transparent p-n junctions”. *Journal of Physics: Condensed Matter* 28.22 (2016), 224004.

[5] Tiffany C Kaspar et al. “Defect compensation by Cr vacancies and oxygen interstitials in Ti^{4+}-doped Cr_2O_3 epitaxial thin films”. *Physical Review B* 94.15 (2016), 155409.

[6] Julian A Crawford and Robert W Vest. “Electrical conductivity of single-crystal Cr_2O_3”. *Journal of Applied Physics* 35.8 (1964), 2413–2418.

[7] N. F. Mott. “Conduction in non-crystalline materials”. *Philos. Mag.* 19 (1969), 835.

[8] M. Catti et al. “Electronic, magnetic and crystal structure of Cr_2O_3 by theoretical methods”. *Journal of Physics and Chemistry of Solids* 57.11 (1996), 1735.

[9] Mark Rubinstein. "Investigation of the Metal-Insulator Transition in V_2O_3 by Nuclear Magnetic Resonance". *Physical Review B* 2.12 (1970), 4731.

[10] Yuzheng Guo, Stewart J Clark, and John Robertson. "Electronic and magnetic properties of Ti_2O_3 , Cr_2O_3 , and Fe_2O_3 calculated by the screened exchange hybrid density functional". *Journal of Physics: Condensed Matter* 24.32 (2012), 325504.

[11] Elisabetta Arca et al. "Effect of Chemical Precursors On the Optical and Electrical Properties of p-Type Transparent Conducting Cr_2O_3:(Mg,N)". *The Journal of Physical Chemistry C* 117.42 (2013), 21901–21907.

[12] Kelvin HL Zhang et al. "P-type transparent conducting oxides". *Journal of Physics: Condensed Matter* 28.38 (2016), 383002.

[13] L. Farrell et al. "Conducting mechanism in the epitaxial p-type transparent conducting oxide Cr_2O_3:Mg". *Phys. Rev. B* 91.12 (2015), 125202.

[14] M O Sullivan et al. "Magnetoresistance of $CuCrO_2$ -based delafossite films". *Journal of Physics: Conference Series* 200.5 (2010), 052021.

[15] DD Sarma et al. "Investigation of hole-doped insulating $La_{1-x}Sr_xCrO_3$ by soft-x-ray absorption spectroscopy". *Physical Review B* 53.20 (1996), 13369.

[16] C Theil, J Van Elp, and Finn Folkmann. "Ligand field parameters obtained from and chemical shifts observed at the Cr $L_{2,3}$ edges". *Physical Review B* 59.12 (1999), 7931.

[17] Aoife B Kehoe et al. "Assessing the potential of Mg-doped Cr_2O_3 as a novel p-type transparent conducting oxide". *Journal of Physics: Condensed Matter* 28.12 (2016), 125501.

[18] Hirofumi Aritani et al. "Characterization of Li-Doped MgO Catalysts for Oxidative Coupling of Methane by Means of Mg K-Edge XANES". *The Journal of Physical Chemistry B* 104.44 (2000), 10133.

[19] Ercan Ünveren et al. "Analysis of highly resolved x-ray photoelectron Cr $2p$ spectra obtained with a Cr_2O_3 powder sample prepared with adhesive tape". *Surface and interface analysis* 36.1 (2004), 92–95.

[20] Mark C. Biesinger et al. "Resolving surface chemical states in XPS analysis of first row transition metals, oxides and hydroxides: Sc, Ti, V, Cu and Zn". *Applied Surface Science* 257.3 (2010), 887.

[21] Mark C. Biesinger et al. "Resolving surface chemical states in XPS analysis of first row transition metals, oxides and hydroxides: Cr, Mn, Fe, Co and Ni". *Applied Surface Science* 257.7 (2011), 2717.

[22] S. Chambers and T. Droubay. "Role of oxide ionicity in electronic screening at oxide-metal interfaces". *Phys. Rev. B* 64.7 (2001).

[23] PA Bhobe et al. "Evidence for a correlated insulator to antiferromagnetic metal transition in CrN". *Physical review letters* 104.23 (2010), 236404.

[24] Eli Stavitski and Frank M.F. de Groot. "The CTM4XAS program for EELS and XAS spectral shape analysis of transition metal L edges". *Micron* 41.7 (2010), 687.

[25] M.G. Brik, N.M. Avram, and C.N. Avram. "Crystal field analysis of energy level structure of the Cr_2O_3 antiferromagnet". *Solid State Communications* 132.12 (2004), 831.

[26] Paul S. Bagus, Eugene S. Ilton, and James R. Rustad. "Ligand-field effects for the 3 p photoelectron spectra of Cr_2O_3". *Physical Review B* 69.20 (2004), 205112.

[27] Hidekazu Ikeno, Teruyasu Mizoguchi, and Isao Tanaka. "Ab initio charge transfer multiplet calculations on the $L_{2,3}$ XANES and ELNES of $3d$ transition metal oxides". *Physical Review B* 83.15 (2011), 155107.

[28] Masahiko Matsubara et al. "Charge Transfer Excitation in Resonant X-ray Emission Spectroscopy of NiO". *J. Phys. Soc. Jpn.* 74.7 (2005), 2052.

[29] J.L. Campbell and T. Papp. “Widths of the Atomic K-N7 Levels”. *Atomic Data and Nuclear Data Tables* 77.1 (2001), 1.

[30] Xiaomei Li, Lizhong Liu, and Victor E. Henrich. “Resonant photoemission determination of the valence electronic structure of Cr_2O_3”. *Solid State Communications* 84.12 (1992), 1103.

[31] Erminald Bertel et al. “Resonant photoemission and the mechanism of photon-stimulated ion desorption in a transition-metal oxide”. *Physical Review B* 31.8 (1985), 5580.

[32] Pingli Qin et al. “Organic solar cells with p-type amorphous chromium oxide thin film as hole-transporting layer”. *Thin Solid Films* 519.13 (2011), 4334.

[33] J. C. Bernede et al. “XPS study of the band alignment at ITO-oxide (n-type MoO_3 or p-type NiO) interface”. *physica status solidi (a)* 209.7 (2012), 1291.

[34] Sandro Lattante. “Electron and hole transport layers: their use in inverted bulk heterojunction polymer solar cells”. *Electronics* 3.1 (2014), 132–164.

[35] Pingli Qin et al. “Nitrogen doped amorphous chromium oxide: Stability improvement and application for the hole-transporting layer of organic solar cells”. *Solar Energy Materials and Solar Cells* 95.3 (2011), 1005–1010.

[36] Zhen Zhang and John T. Yates. “Band Bending in Semiconductors: Chemical and Physical Consequences at Surfaces and Interfaces”. *Chemical Reviews* 112.10 (2012), 5520–5551.

[37] W Jaegermann and D Schmeisser. “Simulation of photoactive semiconductor/electrolyte interfaces in the ultrahigh vacuum by adsorption of H_2O and halogens on layered semiconductors”. *Journal of Vacuum Science & Technology A* 5.4 (1987), 627–628.

[38] Suman Pokhrel et al. “Investigations of conduction mechanism in Cr_2O_3 gas sensing thick films by ac impedance spectroscopy and work function changes measurements”. *Sensors and Actuators B: Chemical* 133.1 (2008), 78.

[39] Annett Thøgersen et al. “Elemental distribution and oxygen deficiency of magnetron sputtered indium tin oxide films”. *Journal of Applied Physics* 109.11 (2011), 113532.

[40] Dongchul Choi, Young Sung Kim, and Yongkeun Son. “Recovery of indium tin oxide (ITO) and glass plate from discarded TFT-LCD panels using an electrochemical method and acid treatment”. *RSC Advances* 4.92 (2014), 50975–50980.

[41] Spyros Diplas et al. “An in situ XPS study of growth of ITO on amorphous hydrogenated Si: Initial stages of heterojunction formation upon processing of ITO/a-Si: H based solar cell structures”. *physica status solidi (a)* 212.1 (2015), 47–50.

[42] JS Kim et al. “X-ray photoelectron spectroscopy of surface-treated indium-tin oxide thin films”. *Chemical Physics Letters* 315.5 (1999), 307–312.

[43] A Bourlange et al. “The influence of Sn doping on the growth of In 2 O 3 on Y-stabilized ZrO 2 (100) by oxygen plasma assisted molecular beam epitaxy”. *Journal of Applied Physics* 106.1 (2009), 013703.

[44] John CC Fan and John B Goodenough. “X-ray photoemission spectroscopy studies of Sn-doped indium-oxide films”. *Journal of Applied Physics* 48.8 (1977), 3524–3531.

[45] Andreas Klein et al. “Transparent Conducting Oxides for Photovoltaics: Manipulation of Fermi Level, Work Function and Energy Band Alignment”. *Materials* 11 (2010), 4892.

[46] A. Klein et al. “Surface potentials of magnetron sputtered transparent conducting oxides”. *Thin Solid Films* 518.4 (2009), 1197.

[47] E. A. Kraut et al. “Semiconductor core level to valence band maximum binding energy differences”. *Phys. Rev. B* 28 (4 1983), 1965.

[48] Oliver Bierwagen. “Indium oxide a transparent, wide-band gap semiconductor for (opto) electronic applications”. *Semiconductor Science and Technology* 30.2 (2015), 024001.

[49] Sebastian Siol et al. “Band Alignment Engineering at Cu_2O/ZnO Heterointerfaces”. *ACS Applied Materials & Interfaces* 8.33 (2016), 21824–21831.

[50] Aron Walsh et al. “Nature of the Band Gap of In_2O_3 Revealed by First-Principles Calculations and X-Ray Spectroscopy”. *Physical Review Letters* 100.16 (2008).

[51] O. Bierwagen et al. “Dissipation-factor-based criterion for the validity of carrier-type identification by capacitance-voltage measurements”. *Appl. Phys. Lett.* 94 (2009), 152110.

[52] Mark T Greiner et al. “Universal energy-level alignment of molecules on metal oxides”. *Nature materials* 11.1 (2012), 76.

[53] M Wilde et al. “Adsorption of potassium on Cr_2O_3 (0001) at ionic and metallic coverages and uv-laser-induced desorption”. *Physical Review B* 59.20 (1999), 13401.

[54] Zhen Zhu et al. “Electronic band structure and sub-band-gap absorption of nitrogen hyperdoped silicon”. *Scientific reports* 5 (2015).

[55] Alexander Yu Dobin, Wenhui Duan, and Renata M Wentzcovitch. “Magnetostructural effects and phase transition in Cr_2O_3 under pressure”. *Physical Review B* 62.18 (2000), 11997.

[56] John J Carey, Merid Legesse, and Michael Nolan. “Low Valence Cation Doping of Bulk Cr_2O_3: Charge Compensation and Oxygen Vacancy Formation”. *The Journal of Physical Chemistry C* 120.34 (2016), 19160–19174.

[57] Samira Dabaghmanesh et al. “Sulfur-alloyed Cr_2O_3: a new p-type transparent conducting oxide host”. *RSC Advances* 7.8 (2017), 4453–4459.

[58] Makiko Muto et al. “Magnetoelectric and second-harmonic spectra in antiferromagnetic Cr_2O_3”. *Physical Review B* 57.16 (1998), 9586.

[59] Glenn Moynihan, Gilberto Teobaldi, and David D ORegan. “A self-consistent ground-state formulation of the first-principles Hubbard U parameter validated on one-electron self-interaction error”. *arXiv preprint 1704.08076* (2017).

[60] Francois Lebreau et al. “Structural, Magnetic, Electronic, Defect, and Diffusion Properties of Cr_2O_3 DFT $+U$ Study”. *The Journal of Physical Chemistry C* 118.31 (2014), 18133.

[61] RL Anderson. “Germanium-gallium arsenide heterojunctions [letter to the editor]”. *IBM Journal of Research and Development* 4.3 (1960), 283–287.

[62] Tripurari Sharan Tripathi and Maarit Karppinen. “Atomic Layer Deposition of p-Type Semiconducting Thin Films: a Review”. *Advanced Materials Interfaces* (2017).

[63] CW Zhong et al. “Stability of High performance p-type SnO TFTs”. *Physical and Failure Analysis of Integrated Circuits (IPFA), 2015 IEEE 22nd International Symposium on the.* IEEE. 2015, 84–87.

[64] Marius Grundmann et al. “Oxide bipolar electronics: materials, devices and circuits”. *Journal of Physics D: Applied Physics* 49.21 (2016), 213001.

[65] S. B. Zhang, S.-H. Wei, and Alex Zunger. “Intrinsic n-type versus p-type doping asymmetry and the defect physics of ZnO”. *Physical Review B* 63.7 (2001).

[66] Kelvin HL Zhang et al. “Electronic Structure and Band Alignment at the NiO and $SrTiO_3$ p–n Heterojunctions”. *ACS Applied Materials & Interfaces* 9.31 (2017), 26549–26555.

[67] S.M. Sze. *Physics of Semconductors.* Ed. by S.M. Sze. Wiley-Interscience, 1969.

[68] Chih-Tang Sah, Robert N Noyce, and William Shockley. “Carrier generation and recombination in pn junctions and pn junction characteristics”. *Proceedings of the IRE* 45.9 (1957), 1228–1243.

[69] Yingge Du et al. “An all-perovskite pn junction based on transparent conducting p-$La_{1-x}Sr_xCrO_3$ epitaxial layers”. *Applied Physics Letters* 111.6 (2017), 063501.

[70] Jonas Deuermeier et al. “Reactive magnetron sputtering of Cu_2O: Dependence on oxygen pressure and interface formation with indium tin oxide”. *Journal of Applied Physics* 109.11 (2011), 113704.

Chapter 5

Investigating the Electronic and Mechanical Properties of Low Temperature Nanocrystalline Cu_xCrO_2

Some applications (displays, thin film solar cells, among others) require materials that are transparent yet also electrical conductors, as a metal contact would inhibit their optical functionality [1, 2]. To date, such transparent electrodes are made from doped metal oxides, most commonly *n*-type Indium Tin Oxide (ITO) [3]. However, there is great scope for flexible electronic devices e.g. printed solar cells, to compliment the mature silicon based electronic industry [4]. The electrical conductivity of ITO is strongly linked to it's long range crystalline order. ITO is quite brittle and often cracks on polymeric substrates under a low strain when deposited over large areas, thus it has shown sub par performance on flexible substrates [5, 6].

Recently, *n*-type amorphous transparent semiconducting oxides such as Indium Gallium Zinc Oxide (IGZO) satisfy the basic criteria required for flexible devices: highly conductive when deposited at low temperatures [7]. It's amorphous nature avoids the complexities and variability of it's polycrystalline counterpart, ITO.

Analogous p-type TCOs have so far only found use in laboratory devices, e.g., buffer layers in dye sensitized solar cells, hole injector in organics light emitting diodes, and water splitting electrodes, while also finding use a possible new range of transparent electrical contacts for p-type semiconductors such as amorphous silicon [8–11].

With an outlook towards cheap printable electronics these lab devices may become industrially relevant. In addition, roll to roll processing of devices requires materials that can withstand tensile strain even if the active device will not be designed to be intentionally bent.

Most p-type TCOs are polycrystalline though, with processing temperatures in excess of 1000 K, which is too high for use with flexible substrates. Only one amorphous *p*-type TCO has been synthesised so far: zinc rhodium oxide [12, 13], however the low conductivity at room temperature (0.14 $\mathrm{Scm^{-1}}$) is not sufficient for applications as a high performance transparent electrode.

This chapter will discuss the design, electronic structure and mechanical properties of a recently synthesised, highly conductive transparent p-type oxide, $\mathrm{Cu}_x\mathrm{CrO}_2$ [14]. Experimental results show that the conductivity of this oxide does not appear to be linked to long range crystalline order, although it is not entirely amorphous. It's suitability as a large area flexible electrode is assessed here as it has deposition temperatures compatible with such substrates.

$\mathrm{Cu}_x\mathrm{CrO}_2$ p-type oxides films were grown by spray pyrolysis (using the procedure outlined in section 3.8) at a deposition temperature of 618 K using copper and chromium acetylacetonate as precursors. A comparison of the Figure of Merit (FoM) with other p-type oxides and ITO is graphed in figure 5.1. A range of FoM values can be achieved with the $\mathrm{Cu}_x\mathrm{CrO}_2$ films by varying the copper concentration. Previous growth of any CuCrO_2 phase had required deposition temperature in excess of 823 K achieving polycrystalline films with a conductivity of 0.9 $\mathrm{Scm^{-1}}$ [15]. The films grown by spray pyrolysis in this work were two orders of magnitude higher in conductivity. This chapter will provide insight into the electronic structure of $\mathrm{Cu}_x\mathrm{CrO}_2$ by employing X-ray Diffraction, X-ray

Absorption Spectroscopy (XAS), X-ray Photoelectron Spectroscopy (XPS) and Resonant Photoemission Spectroscopy (RPES).

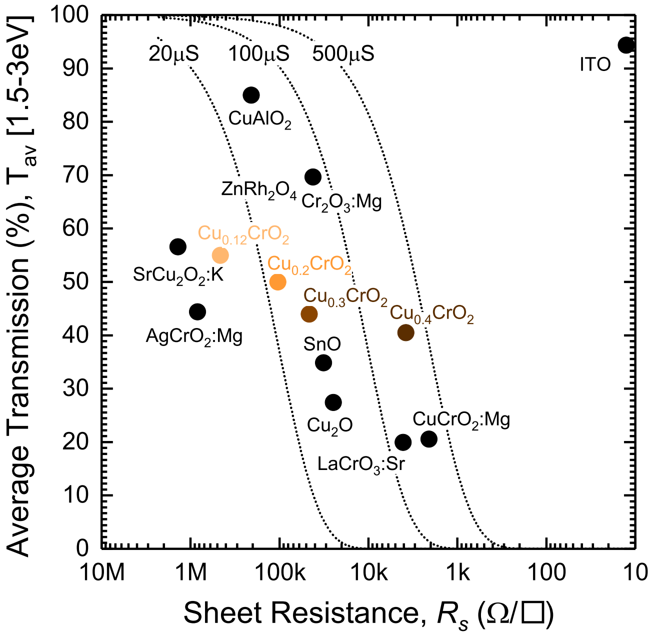

Figure 5.1: Plot of the FoM for nanocrystalline Cu_xCrO_2 for $x = 0.12$, 0.2, 0.3 and 0.4. Other p-type TCOs are plotted for comparison [16–25].

5.1 Verifying the Structure of Cu_xCrO_2

Figure 5.2 shows Grazing Incidence X-Ray Diffraction (GIXRD) measurements performed with a grazing incidence angle of 1° using a large copper soller slit and a scintillation detector on films grown upon polyimide (a standard flexible substrate) and float glass.

The candidate structures for the films were either the spinel $CuCr_2O_4$, corundum Cr_2O_3:Cu or delafossite $CuCrO_2$. Two reflexes were seen in the diffractogram; the diffraction lines were not consistent with Cr_2O_3. GIXRD showed that the reflexes were likely the (012) and (110) diffraction lines of the $CuCrO_2$ rhombohedral structure (space group R$\bar{3}$m). However, the diffraction lines were low in intensity and could also possibly correlate to the spinel $CuCr_2O_4$ (211) and (411) reflexes.

To unambiguously determine the crystalline structure, the copper oxidation

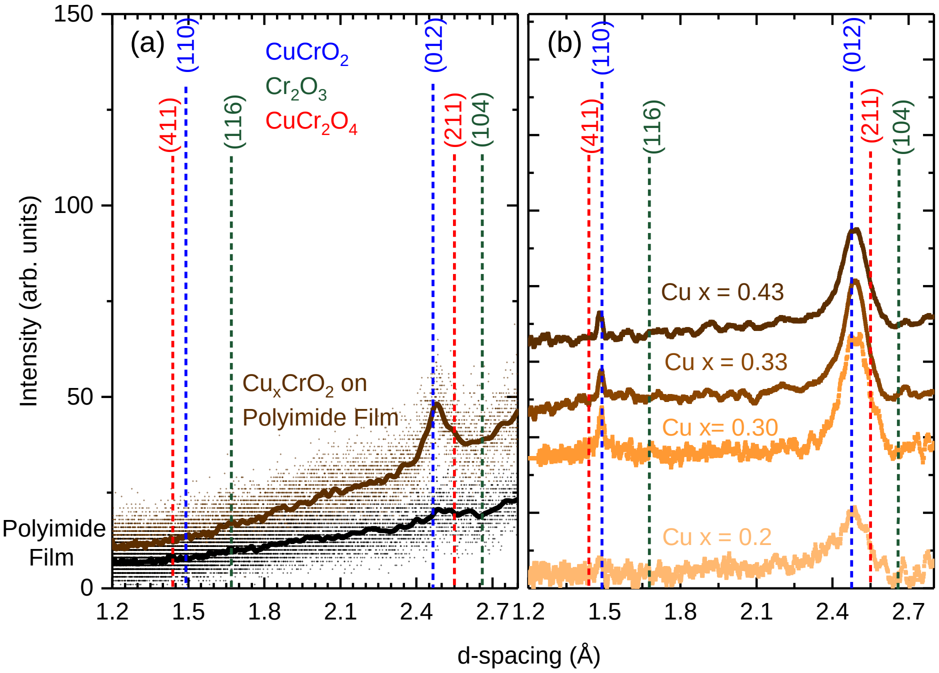

Figure 5.2: Grazing incidence x-ray diffraction of (a) Cu_xCrO_2 grown on polyimide compared to bare polyimide. (b) Cu_xCrO_2 with varying copper content. XRD diffraction lines are shown for $CuCrO_2$, Cr_2O_3 and $CuCr_2O_4$.

state was verified by XPS by analysing the Cu 2*p* core level. The spinel phase ($CuCr_2O_4$) would require the copper to reside in a 2+ oxidation state while within the $CuCrO_2$ structure the copper should adopt an oxidation state of 1+. The oxidation state is easily resolved for copper by XPS indicating the likely structure of the material. The copper Auger LMM peak can be used to quantify the oxidation of copper but due to the close proximity of the Cr 2*p* core level to this Cu Auger and the difficulty in assigning relative amounts of different oxidation states the Cu 2*p* core level was used here [26].

All samples were chemically cleaned *ex-situ* in methanol, acetone and isopropanol in an ultrasonic bath. XPS of the as received film (see figure 5.3 (a)) showed that the main component of the Cu 2*p* core level had a binding energy (932.55 eV), lineshape and FWHM consistent with Cu^{1+} being the predomination oxidation state within the p-type oxide films. A second component was found to reside within the Cu 2*p* core level at a much higher binding energy, 935.20 eV,

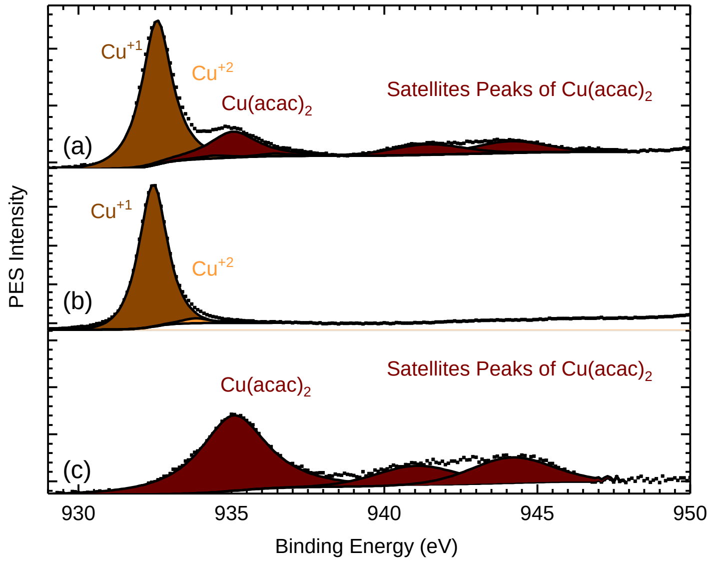

Figure 5.3: (a) XPS spectra of Cu 2*p* peak of Cu_xCrO_2 as deposited and (b) argon sputtered surface of the Cu 2*p* of Cu_xCrO_2. The Cu $2p_{3/2}$ peak is consistent with a Cu^{+1} oxidation state with a binding energy of 932.4 eV, FWHM = 1.1. Small quantities of Cu^{+2} at 933.8 eV are still present after sputtering. The Cu satellite peaks between 940-945 eV for Cu^{2+} is notably absent. (c) $Cu(acac)_2$ precursor.

than would be expected for a Cu^{+2}-O bond. The Cu^{2+} state within CuO can be identified by a broad peak (Full Width Half Maximum (FWHM) equal to 3 eV) at a binding energy of 934.4±0.25 eV and a large shake up structure between 940 eV and 950 eV [27]. The shake up structure (figure 5.3 (a)) did not have the signature shape indicating a Cu-O bond associated with the spinel phase. Figure 5.3 (c) shows an XP spectra of the unreacted copper acetylacetonate precursor used to grow the film. It matches the spectral features seen on the as received surface indicating residual vapours in the chamber may deposit on the surface leaving a layer of unreacted precursor on each film.

Figure 5.3 (b) showed the spectra after argon sputtering. The argon ion gun was operated at 500 V for 10 minutes with a sputter current of 2–3 μA. The resultant Cu 2*p* spectrum (figure 5.3 (b)) showed the composition of the bulk film to be 98 % Cu^{1+}, 2 % Cu^{2+} and all traces of the precursor removed.

Hence, based on the XPS and XRD measurements the structure for the films

Table 5.1: Copper 2*p* spectral composition the (a) as received and (b) argon sputtered Cu_xCrO_2 surface. BE= Binding Energy

(a)	BE (eV)	Area (%)	**(b)**	BE (eV)	Area (%)
Cu^{+1}	932.55	61.30		932.46	98.38
Cu^{+2}	934.44	1.19		934.44	1.62
$Cu(acac)_2$	935.20	17.79			
$Cu(OH)_2$	936.41	1.11			
$Cu(acac)_2$ Sat. 1	941.43	8.81			
$Cu(acac)_2$ Sat. 2	944.14	9.79			

was concluded to be a nanocrystalline $CuCrO_2$ delafossite structure [14, 28]. From the XRD pattern the a and c lattice parameters were calculated to be 2.98±0.05 Åand 17.16±0.05 Å, respectively, which is close to their crystalline values of 2.97 Å and 17.1 Å. The weak (012) reflex (figure 5.2) is attributed to ordering of the O-Cu-O planes in the nanoscale regime. The average coherent domain size using the Scherrer equation was estimated to be less than 10 nm. The (006) reflex for $CuCrO_2$ is notably absent: indicating either a randomly ordered CrO_6 environment or a strong crystallographic texturing of the film.

5.2 Growth of Cu_xCrO_2 Films

To achieve the optimum film optical and electrical properties a screening of the copper/chromium ratio, temperature and oxygen partial pressure was carried out. The aforementioned film properties showed a strong dependence on temperature. The films' electrical conductivity is greatly reduced when grown outside the temperature window of 618 ± 3 K upon float glass. This is likely due to the fact that in spray pyrolysis the substrate temperature governs precursor decomposition and the rate of solvent evaporation. The change in either parameters is likely to effect the growth rate: affecting the depositing of alternating layers of Cr and Cu that compose the delafossite structure. The narrow surface temperature for optimum film growth was unchanged for growth on the polyimide films (with a thickness of 0.08 mm) once they were placed upon float glass and not directly upon the hot plate.

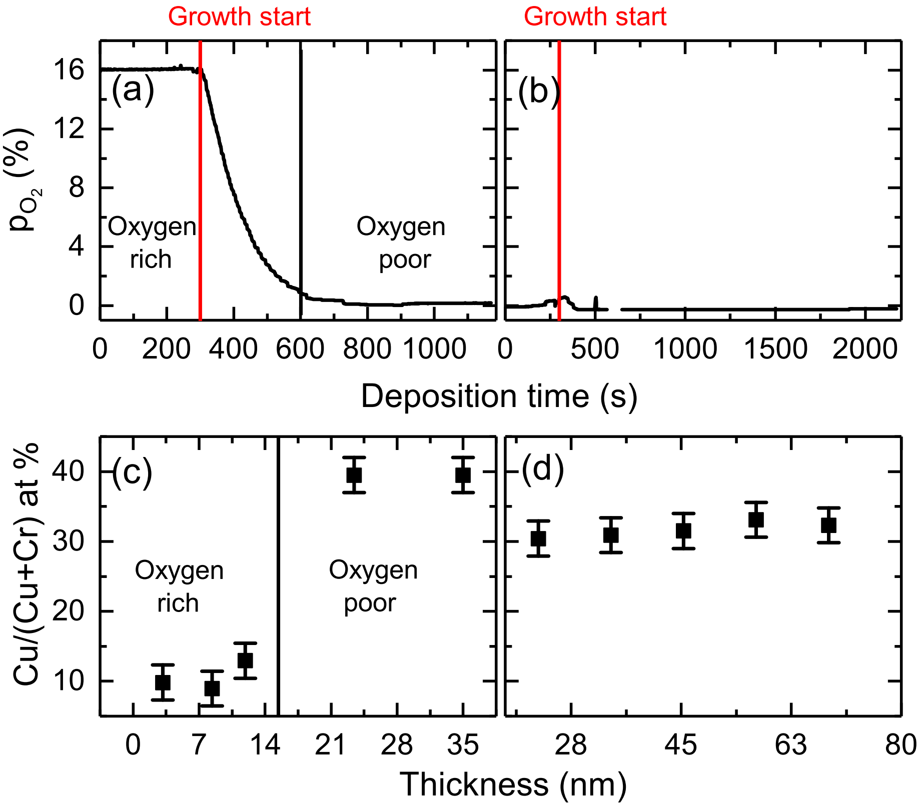

Figure 5.4: (a) The oxygen partial pressure during growth for a non evacuated chamber (b) The oxygen partial pressure during growth for a chamber pre evacuated with nitrogen (c) Depth profile of a Cu_xCrO_2 film when the initial oxygen partial pressure of the chamber is 16 % (d) Depth profile of a Cu_xCrO_2 film when the initial oxygen partial pressure within the chamber is $\approxeq$ 0 %

The effect of the oxygen partial pressure on the composition of the initial Cu_xCrO_2 films was quantified by using XPS depth profiling and measuring the atomic concentration of chromium and copper. The residual precursor seen on as-grown films (see figure 5.3 (a)) was first removed before quantifying the Cu/Cr ratio of any film. The Cr 2*p* and Cu 2*p* core levels were used to quantify the composition of the films. A one to one Cu:Cr ratio would be expected for a stoichiometric delafossite phase. All films quantified (figure 5.1) were deficient in copper. $Cu_{0.4}CrO_2$ was the highest copper content that could be incorporated into the lattice under these growth conditions, which gave the highest conductivity achieved of 12 Scm^{-1} [14]. Increasing the copper/chromium precursor ratio further did not result in a higher quantity of copper incorporated into the lattice at these temperatures.

The film was etched using an argon ion gun operated at a voltage of 750 V with a sputter current of 8.5 μA. The atomic ratio was taken at each interval after sputtering for 0, 10, 33 and 60 minutes. The Cu 2*p* and Cr 2*p* lineshape does not change significantly. The rate of etching by argon sputtering was estimated by XRR of a film before and after 15 minutes of etching using the above sputtering conditions. The reduced thickness was then converted into an estimate of the etching time to create an approximate depth profile of an entire film.

Cu_xCrO_2 films grown in an oxygen rich environment showed that a consumption of oxygen occurred until the overall chamber oxygen partial pressure lowered to be approximately 0 %. This consumption of oxygen during film growth is often seen when using methanol as a solvent, however the XPS depth profile revealed that as the oxygen partial pressure within the chamber decreased the incorporation of copper within the films increased (see figure 5.4 (a)&(c)). This was attributed to the fact that the formation of Cr_2O_3 is favoured in an oxygen rich environment.

Growth of films without a controlled constant oxygen partial chamber pressure then led to films with an inhomogeneous incorporation of copper. Pre-evacuation of the growth chamber with nitrogen gas to reduce the partial pressure of oxygen within the chamber to be approximately 0 % ensured the copper incorporation was homogeneous (see figure 5.4 (b)&(d)). However, if some small quantity of oxygen (approximately 2 %) is not introduced into the chamber the reaction mechanism to produce Cu_xCrO_2 films does not proceed and the precursors are left on the surface of the substrate. A fixed ratio of compressed air/nitrogen (5 %/95 %) sprayed into the chamber was found to result in the most conductive Cu_xCrO_2 [28]. The highest FoM and conductivity is achieved with $x = 0.42$, however a more transparent but resistive Cu_xCrO_2 film can be achieved with a lower copper content, as is shown in figure 5.1.

Popa et al. pushed the copper content even higher to $Cu_{0.45}CrO_2$ by depositing films by chemical vapour deposition [29] and achieved a conductivity of 100 Scm^{-1}. The XRD measurements showed that a much higher ordering of the O-Cu-O planes which most likely contributes to the higher conductivity observed.

5.3 Electronic Structure of Cu_xCrO_2

The previous two sections outline how the crystalline structure and phase has been verified. However, an explanation for the deficient Cu_xCrO_2 nanocrystalline films being two orders of magnitude more conductive than polycrystalline $CuCrO_2$ films is desired. How the local atomic coordination of the Cu_xCrO_2 films changes with an increasing copper concentration provides insight into the electronic structure of the thin films. This can be probed by spectroscopic technique XAS.

When the Cr L edge for Cu_xCrO_2 films (figure 5.5 (b)) is compared with the epitaxial $Cr_{2-x}Mg_xO_3$ and Cr_2O_3 Cr $L_{2,3}$ edge (see figure 4.2) it is apparent that the absorption features are not as sharp as in the epitaxial films. This likely arises due to a more ordered local coordination of the chromium atoms than the nano crystalline Cu_xCrO_2 films which have a random crystal axis orientation. Spectral features remain consistent across the films, indicating the local electronic structure of the chromium atoms within Cu_xCrO_2 films is similar to the $Cr_{2-x}Mg_xO_3$ films.

5.3.1 Cu L_3 edge

Unlike the chromium absorption spectra, the assignment of a clear oxidation state and electronic structure with a cuprite phase, Cu_2O (Cu^{+1}), is difficult. The copper x-ray absorption spectra have been difficult to analyze. Nominally, a Cu^{1+} oxidation state would be expected to have fully occupied Cu 3d states in the valence band and an empty Cu 4s conduction band. Band structure calculations by Hulbert et al. show Cu_2O to have substantial 3d character in the conduction

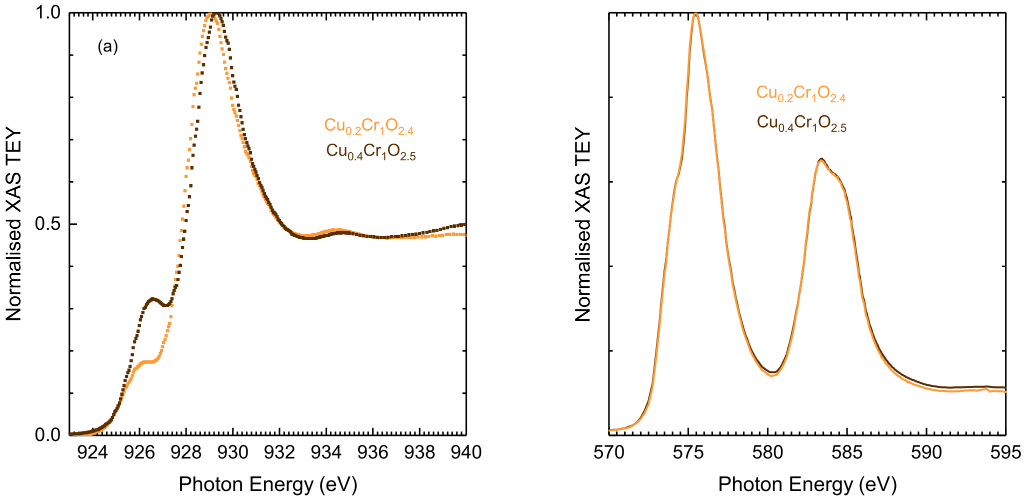

Figure 5.5: (a) X-ray Absoprtion Spectroscopy of the Cu L_3 edge of $Cu_{0.2}Cr_1O_{2.4}$ and $Cu_{0.4}Cr_1O_{2.5}$.(b) Cr $L_{2,3}$-edge of $Cu_{0.2}Cr_1O_{2.4}$, $Cu_{0.4}Cr_1O_{2.5}$

band and conversely 4*s* character in the valence band [30]. However, experimentally the Cu $L_{2,3}$ edge is difficult to analyze as x-ray spectroscopic investigations are nearly always overly sensitive to a mixed ground state as 2*p* edge core level spectroscopy is dominated by atomic multiplet effects as noted for instance in Resonant Inelastic X-ray Spectra (RIXS) of Cu_2O being dominated by $3d \rightarrow 3d^*$ transitions [31].

Surface Electronic Structure of Cu_xCrO_2 Films

Figure 5.6 (a) shows the as-grown Cu L_3 edge. A large absoprtion feature is seen at a photon energy of 926 eV below the onset of the L_3 edge. When the sample is argon sputtered at a pressure of 4 $\times 10^{-4}$ Pa with a beam energy of 1 keV at grazing incidence the intensity of the feature is significantly reduced. The pre-edge absorption feature does not reappear after vacuum annealing but oxygen annealing at 1×10^{-3} Pa at 500 K produces the same Cu L_3 edge features seen in the as-grown film. The pre-edge feature of the Cu L_3 edge appears to be associated with surfaces exposed to air or oxygen annealing. This would indicate an increase in the number of a defect-like complex associated with increasing the copper content in the films themselves. The fact that this increase is not observed by vacuum annealing alone and that the Cr $L_{2,3}$ edge is not affected leads to the identification of a Cu-O$_i$ defect complex as a likely candidate.

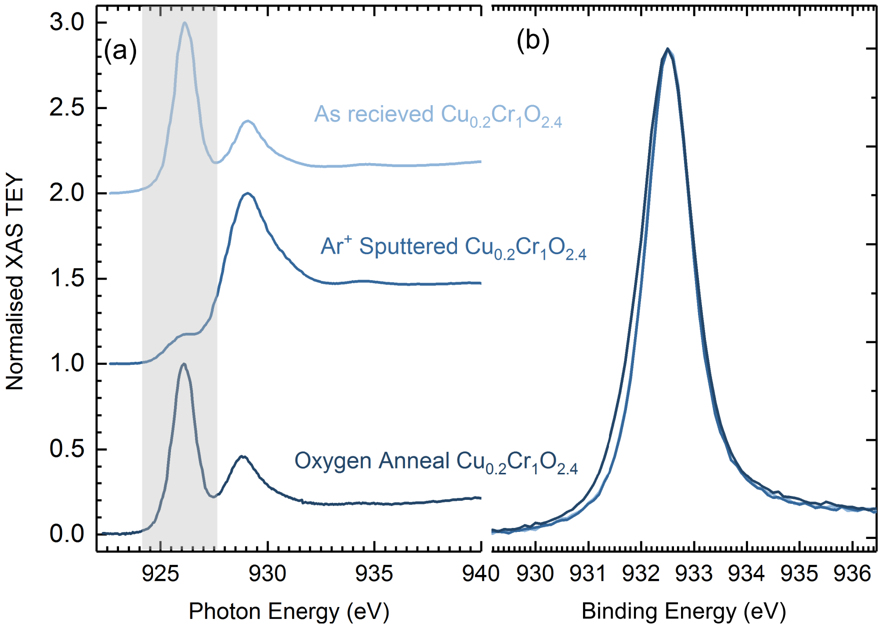

Figure 5.6: (a)X-ray Absoprtion Spectroscopy of the Cu L_3 edge as a function of surface preparation. A large pre-peak, contained within the grey box, is observed at $h\nu = 926$ eV in as-received Cu$_x$CrO$_2$ films. Argon sputtering reduces, but does not eliminate this peak entirely. Oxygen annealing after argon sputtering reproduces the same prepeak. (b) X-ray photoelectron spectroscopy of Cu$_x$CrO$_2$ films highlighting the core level changes when the sample is argon sputtered and annealed in oxygen. A slight increase in the peak asymmetry is noted when the film is annealed in oxygen.

The increase in intensity of the Cu L_3 edge pre-edge feature correlates with an increase in asymmetry of the Cu $2p$ core level, reflecting an increase in metallicity of the system [32]. This indicates some doping of the lattice occurs with the increase in intensity of this pre-edge Cu L_3 feature. Figure 5.5 also shows that this feature appears in the bulk Cu L_3 edge and increases in intensity in the more conducting Cu$_{0.4}$CrO$_2$ sample, further confirming that this feature is associated with an increase in the conductivity of Cu$_x$CrO$_2$ films.

A similar pre-edge feature was found to appear in the Cu L_3 edge of magnesium doped CuCrO$_2$; increasing in intensity with magnesium concentration [33]. The appearance of feature is then suggested to originate due to a different copper electronic configuration associated with defect complexes that are generated by magnesium substitution [33], while they natively occur in the copper deficient Cu_xCrO_2.

Density Functional Theory (DFT) calculations of single point defects in Cu_xCrO_2 have shown that V_{Cu} are the most readily formed intrinsic defects, while Mg_{Cu} is the dominant defect in doped materials [34]. However, no evaluation of complex defects such as Mg_{Cu}–V_{Cu} or V_{Cu}–O_i has been performed yet. In the related Cu_2O, it has already been shown that the formation of defect complexes readily occurs, explaining, e.g., why Sr^{+2} doping in Cu_2O leads to p-type conductivity as the p-type Sr_{Cu}–V_{Cu} defect complex is more likely to form than the n-type Sr_{Cu} isolated point defect [35]. In a similar fashion, other native defect complexes in $CuCrO_2$ could be contributing factors. The identification of their detailed nature would require *ab initio* analysis of many possible combinations including Cr_{Cu}–V_{Cu}, V_{Cu}–O_i and others.

Popa et al. has provided further insight into the origin of the conductivity for non stoichiometric $CuCrO_2$. Unlike the XP spectra which reflects an average composition of the sample, STEM EELS provides an elemental mapping of the individual grains of the Cu_xCrO_2 films: it confirms the deposited sample is composed of alternative planes of Cr and Cu as would be expected for a delafossite phase, with a clear absence of some copper rows. After thermal treatment under argon atmosphere at 1173 K these defects are healed and the resultant samples contain stoichiometric $CuCrO_2$ with excess Cr precipitated at grain boundaries into Cr_2O_3 or Cr metal phases [29]. The films become more resistive after annealing further promoting the concept that off stoichiometric $CuCrO_2$ has an acceptor doping of the lattice due to the absence of copper rows. Although the absence of copper rows prior to annealing likely provides acceptor doping of the films, it does not confirm that the charge carriers move along the copper planes as theorised by Popa et al. [29]. Resonant Photoemission Spectroscopy (RPES) is both sensitive to the unoccupied Density Of States (DOS) within the valence band and element selective so the conduction mechanism of the charge carriers can be analysed more in depth.

5.3.2 Electronic Structure of the Valence Band of Cu_xCrO_2

RPES was performed on both $Cu_{0.4}CrO_2$ and $Cu_{0.2}CrO_2$ films, while resonant separately to the Cr 3*d* and Cu 3*d* states. The theoretical background of RPES as a technique is outlined in section 3.4. Experimental confirmation of the composition of the valence band in this manner is not often performed for many materials, due to the need for a tunable photon energy range. Theoretical modelling is the most routine method to analyse the band structure of a given material, however DFT calculations on the electronic structure of the delafossite $CuCrO_2$ led to conflicting reports on the nature of the top of the valence band: whether it is predominately composed Cu or Cr 3*d* states. Chemical modulation of the valence band proposed by Kawazoe et al. would expect the top of the valence band to have mainly Cu 3*d* character, whereas it would be desirable to have mainly Cr 3*d* character for better thermoelectric properties [36, 37]. Due to the fact that both CuO and Cu_2O show much higher conductivity than Cr_2O_3 it would be intuitive to assume that Cu 3*d* states composed the valence band maximum. The first reports from theoretical and experimental studies suggested that Cu 3*d* states lay at the top of the valence band [38–40]. Reports following this have showed that by changing the Hubbard parameter (U), it could be equally possible that Cr 3*d* states compose the top of the valence band [34, 37]. For this reason, the band structure of $CuCrO_2$ is under debate in the literature. Experimentally for $CuCrO_2$:Mg films, the position of the valence band maximum as measured by RPES showed evidence that in fact chromium states predominately compose the top of the valence band [33]. This was also verified to hold true within this work for Cu_xCrO_2 films.

Cr 3p-3d Resonance in $Cu_{0.2}CrO_2$

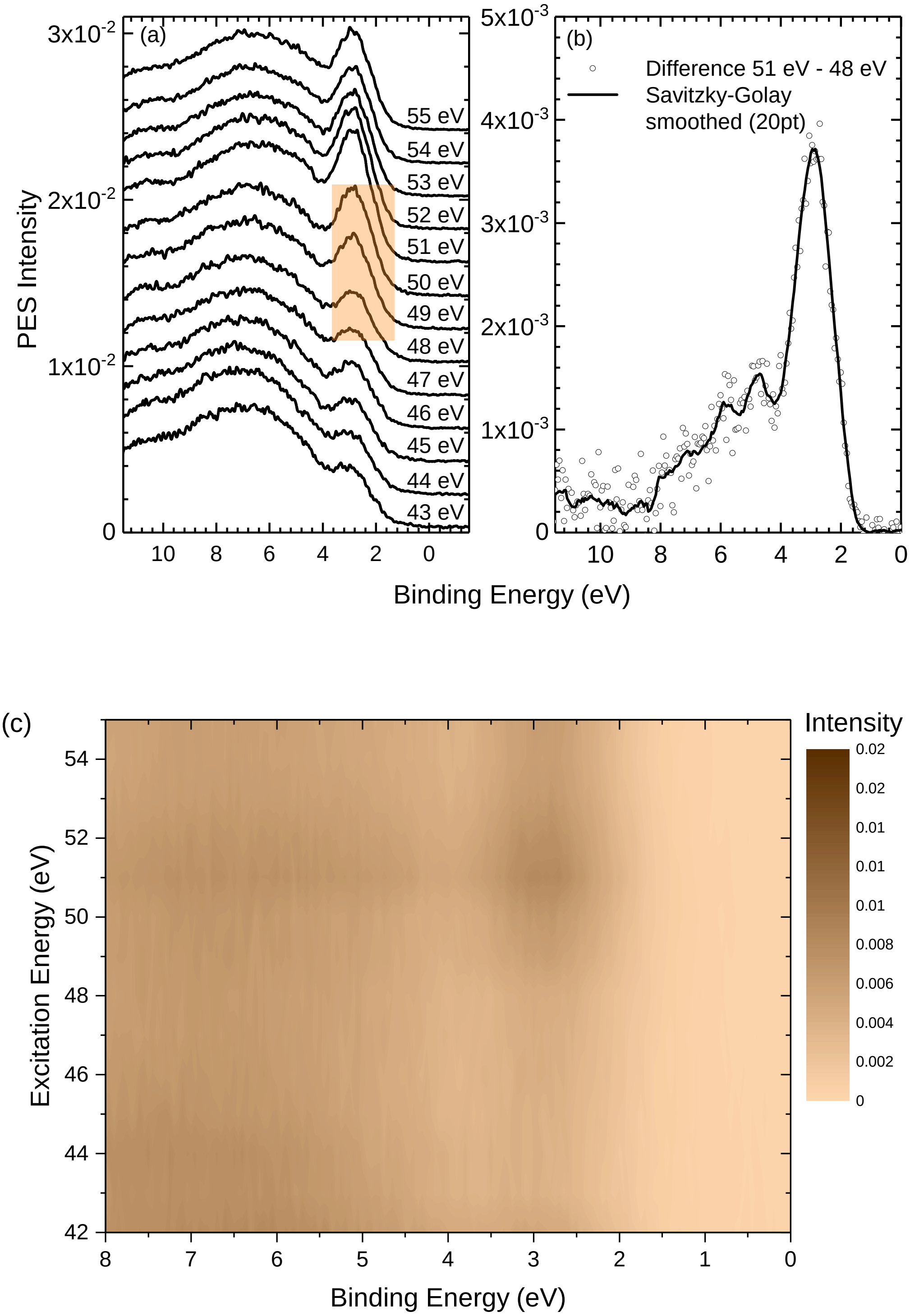

Figure 5.7: The orange box in (a) indicates the region where resonant behaviour is exhibited between 48 and 51 eV. (b) By taking the difference of the two valence band spectra at 48 and 51 eV the partial Cr 3d unoccupied DOS can be plotted. It appears at a binding energy of 3 eV within the valence band with a FWHM of 1.7 eV, with an photoemission intensity increase equal to 0.4 %. (c) 2D contour plot of the valence band intensity changes across the range of excitation energies.

Cr $3p$-$3d$ Resonance in $Cu_{0.4}CrO_2$

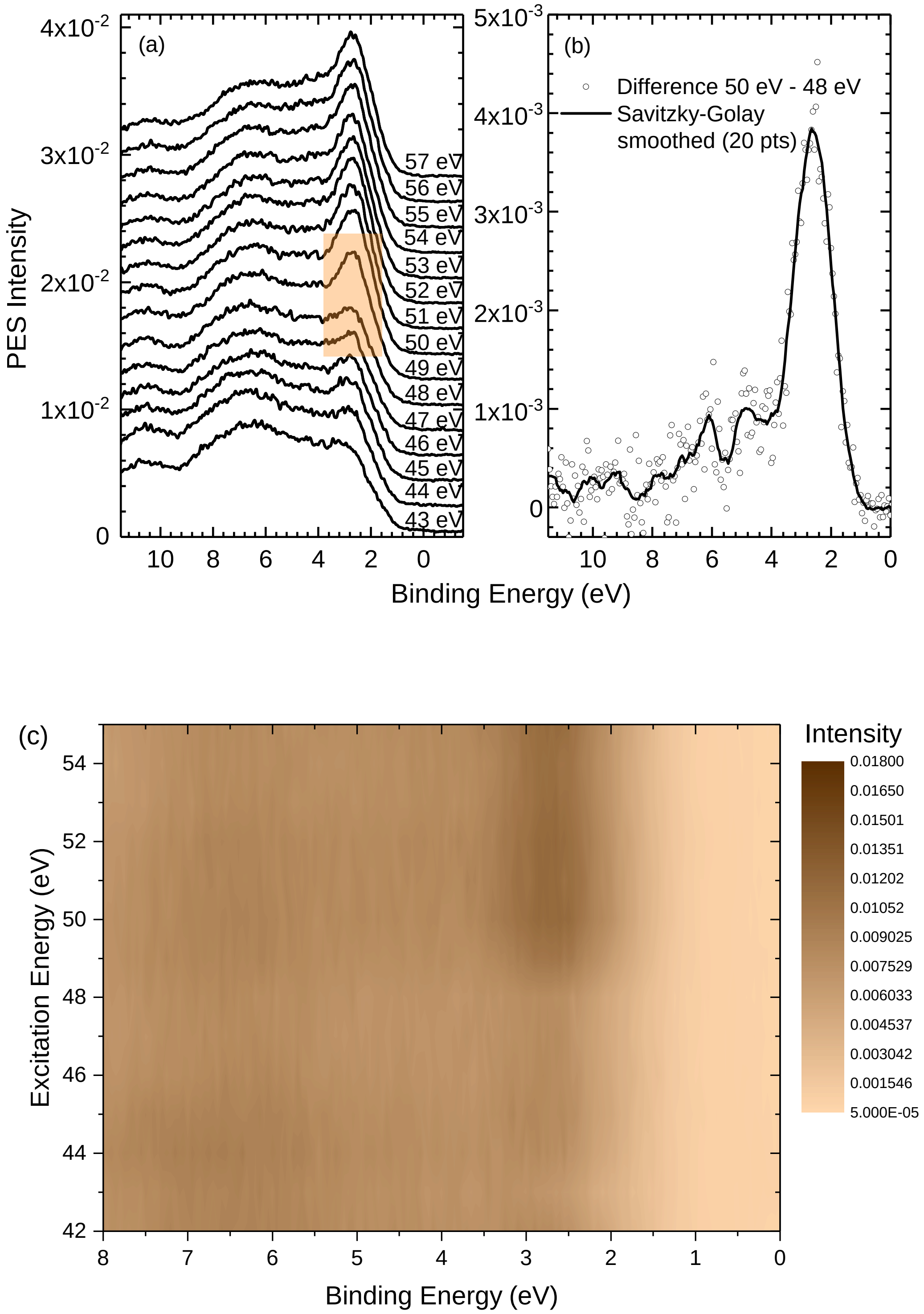

Figure 5.8: The orange box in (a) indicates the region where resonant behaviour is exhibited between 48 and 50 eV. (b) By taking the difference of the two valence band spectra at 48 and 50 eV the partial Cr $3d$ unoccupied DOS can be plotted. Peak fitting shows the sharp onset of resonance to be at a binding energy of 2.6 eV with a FWHM equal to 1.6 eV and an increase of PES intensity is 0.4 % from 48-50 eV at 2.6 eV binding energy for the $Cu_{0.4}CrO_2$ sample. (c) 2D contour plot of the valence band intensity changes across the range of excitation energies.

5.3.3 Chromium Resonance within Cu_xCrO_2Films

Figure 5.7 and 5.8 shows measurements for the investigated Cu_xCrO_2 films over the photon energy range that is resonant to a Cr 3*p* - 3*d* transition. The spectral feature nearest the valence band maximum at a binding energy of 2.6 eV, for the highest copper content Cu_xCrO_2 sample, shows a resonance to this transition between the photon energies of 48 eV and 51 eV. The intensity of this Cr 3*p* - 3*d* resonance is broader and less intense by a factor of nearly two compared to the $Cr_{2-x}Mg_xO_3$ film (see figure 4.5).

The Cr 3*p* - 3*d* resonance is composed of two distinct onsets for the $Cu_{0.4}CrO_2$ film which matches the features seen within the $Cr_{2-x}Mg_xO_3$ films (see figure 5.8). The origin of the two separate resonant features within $Cr_{2-x}Mg_xO_3$ films was found to originate because of the an energetic splitting of the t_{2g} and e_g levels. It would seem likely that the disordered nature and lack of long range order in the Cu_xCrO_2 films could lead to a breakdown of crystal field symmetry rules and the absence of these features. However, the observation of two distinct resonances within the $Cu_{0.4}CrO_2$ films lends further evidence to the localisation of Cr 3*d* states.

However, a second resonance between an excitation energy of 44 eV and 46 eV that exists in $Cu_{0.4}CrO_2$ and $Cr_{2-x}Mg_xO_3$ is not seen in $Cu_{0.2}CrO_2$ (see figure 5.7). This is likely due to the resonance being of too low intensity to be detectable.

Comparison of the Chromium Resonance within Cu_xCrO_2 and $Cr_{2-x}Mg_xO_3$ Films

A comparison between the resonant features occurring between the photon energies of 48 eV and 51 eV seen in all chromium based p-type TCO films within this work are plotted in figure 5.9 (c). The chromium resonance occurs within all films near the valence band maximum. This correlates well with the previous works by Yokobori et al. on crystalline $CuCrO_2$:Mg films where the top of the valence band exhibits a strong chromium resonance around the Cr 3*p*-3*d* transition. The intensity change at resonance within the $CuCrO_2$:Mg film was found to be 0.3 %, which is approximately the magnitude of the observed intensity change in the copper deficient Cu_xCrO_2 films investigated here [33]. What is particularly striking

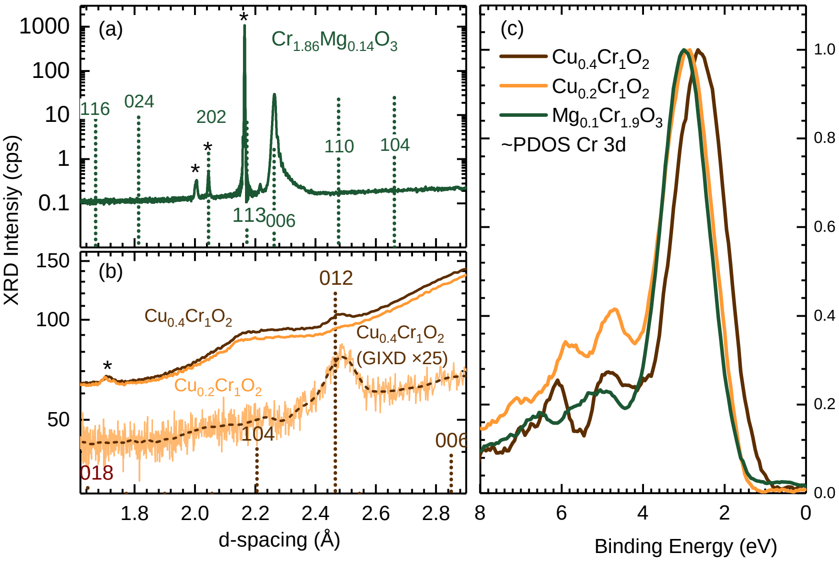

Figure 5.9: (a) X-ray diffraction of the analysed samples. The top panel shows the epitaxially grown $Cr_{2-x}Mg_xO_3$. Only the 006 reflex of the eskolaite phase is observed. (b) The lower panel shows the data for the nanocrystalline Cu_xCrO_2. To illustrate the polycrystalline nature, a symmetric $\theta/2\theta$ measurement is compared to a grazing incidence measurement. Only the strongest $CuCrO_2$ reflex can be observed for the sample with higher copper content. Structures originating from the substrate and/or sample holders have been marked with an $*$. (c) Comparison of unoccupied partial DOS of the Cr $3d$ states of three films $Cr_{2-x}Mg_xO_3$, $Cu_{0.2}CrO_2$ and $Cu_{0.4}CrO_2$

is that all three differential spectra observed in the Cu_xCrO_2 and $Cr_{2-x}Mg_xO_3$ films shows similar chromium resonant features while possessing vastly different crystalline ordering, demonstrated with the XRD measurements in figure 5.9 (a). As the unoccupied DOS associated with the Cr $3d$ states in unchanged by long range order, it is suggested that there is a localisation of the Cr $3d$ states within the CrO_6 octahedra.

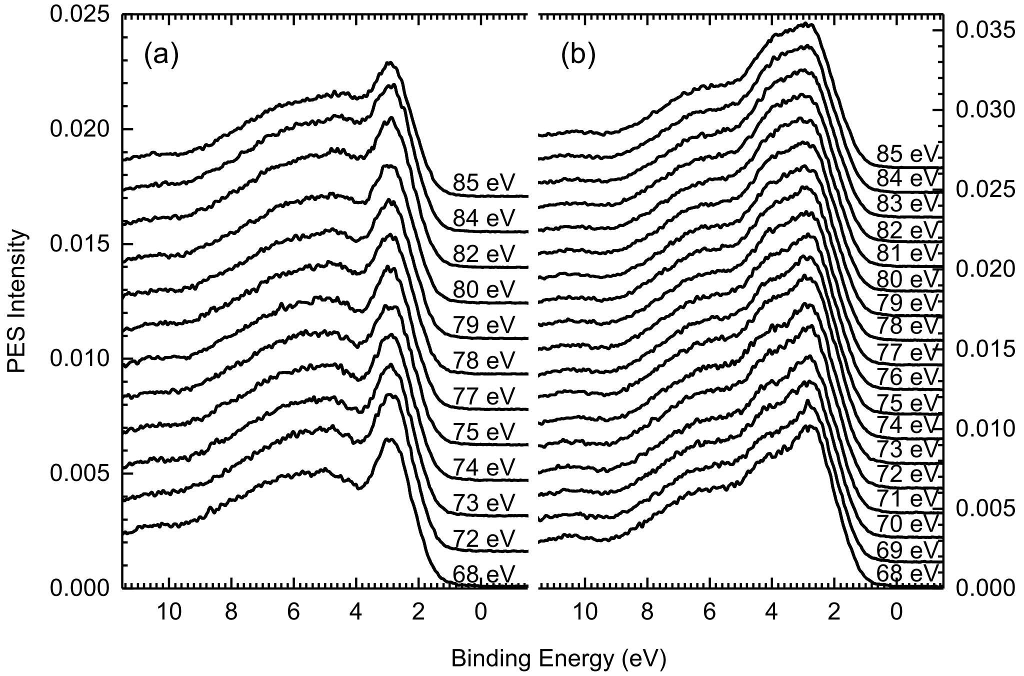

Figure 5.10: Valence band spectra of Cu_xCrO_2 films over the photon energies 68-85 eV, probing the copper 3*p*-3*d* resonance of (a) $Cu_{0.20}CrO_2$ (b) $Cu_{0.40}CrO_2$

5.3.4 Copper Resonance within Cu_xCrO_2 Films

The highest occupied states of the copper atoms will also compose the valence band of Cu_xCrO_2 films, which are the Cu 3*d* states. However no copper resonance is seen as shown in Fig. 5.10. Stoichiometric, crystalline $CuCrO_2$:Mg shows a weak resonance around the Cu 3*p*-3*d* transition, approximately a factor of four smaller than for the Cr 3*p*-3*d* resonance [33]. In contrast to these measurements, the Cu_xCrO_2 films are substantially copper deficient and crystallographically disordered. [28]. The two charge transfer satellites at 13 eV and 15 eV corresponding to Cu^+ ($3d^{10}$) and Cu^{2+} ($3d^9$) like initial states are not observed as in $CuCrO_2$:Mg [33]. It would be expected that reduced intensity, due to a lower copper content, could render the Cu 3*p*-3*d* resonance and charge transfer satellites unresolvable in these films while also being further complicated by the delocalised nature of copper *d* states due to on-site 3*d*–4*s* hybridization which introduces 4*s* character into the valence band. The lack of any detectable copper

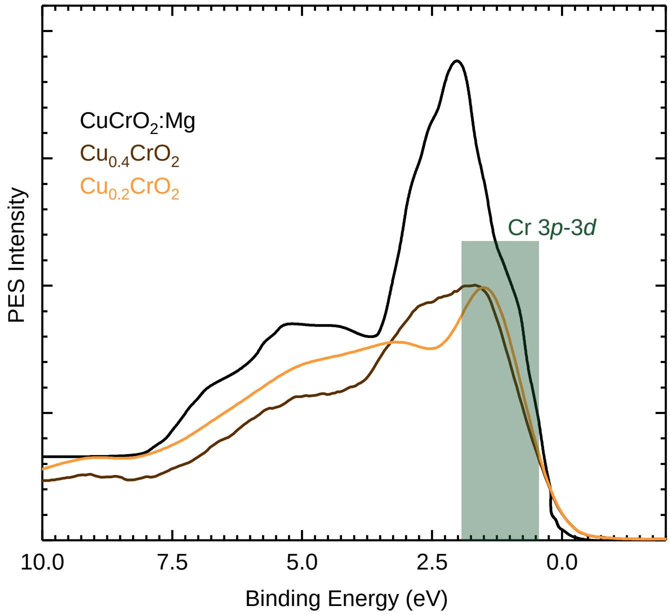

Figure 5.11: Valence-band spectra of all p-type films compared at the photon energy of 85 eV. For comparison, all spectra have been aligned to the valence-band maximum of $CuCrO_2$:Mg [33] to account for shifts in the Fermi level of the different oxide films.

resonance sets an upper limit on any resonant behaviour.

This upper limit of a weak copper resonance and a strong chromium resonance lends support to the proposed mechanism by Yokobori et al. that the ground state of $CuCrO_2$ is showing signs of a Cu 4*s*–Cr 3*d* charge transfer in $CuCrO_2$ films.

A qualitative comparison of the DOS of Cu_xCrO_2 films for x= 0.2, 0.4 and 1 was made due to the absence of a copper 3*p*-3*d* resonance. DFT calculations can model the composition of the valence band spectra. However, as mentioned previously, some discrepancy can arise about the best parameters to model a particular material. Experimental reports become crucial to providing qualitative evidence for modelling material properties.

The top of the valence band in all three films at 1.5 eV is attributed to the Cr 3*d* states, as the position coincides with the Cr 3*d* partial DOS extracted from the differential valence band PES. The spectral features of Yokobori et al. were assigned by DFT calculations in their report with predominant oxygen *p* states lying between 4 and 8 eV. We assume the O 2p states to lie in a similar energetic region for our Cu_xCrO_2 films.

Comparing the spectral shape of the three Cu_xCrO_2 films' valence bands, the higher the copper content in a film correlates to increase in intensity at approximately 3 eV apparent. This lies in a similar region as in the DFT calculations for the Cu 3d states of crystalline $CuCrO_2$:Mg [33]. If compared to the previously investigated crystalline material, all valence-band structures are significantly broadened, which is a consequence of the defective, nanocrystalline nature of the films. Equally, the ratio between the Cr 3d and Cu 3d intensity significantly differs from previous reports, as all films investigated here are copper deficient.

Even thought there is no copper resonance seen within the films, there is an increase in DOS seen at a binding energy of 2.5 eV which correlates with an increase copper content as seen in figure 5.11. This would seem to indicate that the Cu 3d states lie below the valence band but increase the hybridisation between the O 2p and Cr 3d states. $CuCrO_2$ is then different from other delafossites, since electrons are strongly correlated due to the half-filled 3d states of Cr, and the Cu 3d do not compose the valence band maximum.

Conduction Mechanism

In summary, magnesium doping of $CuCrO_2$ and copper deficient Cu_xCrO_2 films lead to formation of some copper defect complex that improves the conductivity of these films above stoichiometric films. The activation energy of carriers within Cu_xCrO_2 is approximate 65 meV [25]. However, the Cr 3d states lie at the top of the valence band maximum. The Cu 3d states lie while below the valence maximum. If the conduction was primarily associated with the Cu 3d states the value of the activation energy would be expected to be much larger. One possibility is that the conduction mechanism within Cu_xCrO_2 must be mediated by the Cr 3d states. Another possibility for p-type metal oxides is that the activation energy is being aritifcally lower by the presence of a large quantity of grain boundaries [41].

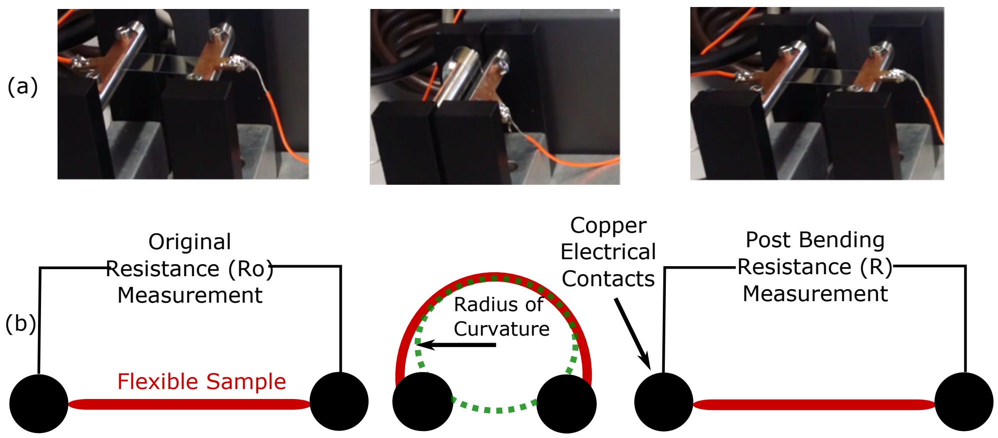

Figure 5.12: (a) Images of the apparatus at each stage of the bending cycle. (b) Schematic of one tensile strain bending cycle. The analogous compressive strain is applied when the film is bent in a ∪-shape

This is certainly a possibility for Cu_xCrO_2 but highly conductive single crystalline magnesium doped $CuCrO_2$ retains a high conductivity leading to some doubt this is the overall conduction mechanism of $CuCrO_2$ [33].

5.4 Low temperature deposition of Cu_xCrO_2upon polyimide film

Cu_xCrO_2 films are one of the only highly conductive p-type oxides at deposition temperatures compatible with flexible substrates, making it a possible candidate as a large area flexible electrode. Cu_xCrO_2 films share a Cr_2O_3 edge sharing network similar to Rh_2O_3 in amorphous zinc rhodium oxide. All corundum structure compounds pocess this same edge sharing network where a third of the chromium sites are unoccupied. These leaves oxygen octhedra “sharing” metal atoms. This edge sharing network Rh_2O_3 in zinc rhodium oxide seems quite insensitive to distortion in an amorphous state [12]. The nanocrystalline nature of the Cu_xCrO_2 films with a disordered CrO_6 edge sharing network could provide a similar resilience for the films to tensile strain.

5.4.1 Depoistion

Copper acetylacetonate (0.012 M) and chromium acetylacetonate (0.03 M) precursors were dissolved in methanol. The solution was sprayed at a rate of 1.67 ml min^{-1} with an air blast nozzle (PNR, model 0331) using a mixture of compressed air/nitrogen (5 %/95 %) controlled with a mass flow controller (Vogtlin, model red-y). The gas pressure was held constant at 17 L min^{-1}. This was sprayed from a distance of 30 cm above a hot plate. Two substrates were used for this work: glass microscope sildes (Fisher brand, thickness 0.8-1 mm) and polyimide (DuPont Kapton) film. The polyimide film rested upon microscope glass slides which lay on the hot plate surface. Heater surface temperature readings during spraying were taken using a type K thermocouple (chromel vs. alumel) welded to the top of the hot plate. The temperature was Proportional Integral Derivative (PID) controlled during spray conditions within 10 K. The surface temperature at the substrate may systematically differ.

5.4.2 Mechanical Measurements

Cu_xCrO_2's suitability as a large area as a flexible electrode was investigated by measuring the change in the electrical resistance after mechanical tensile and compressive strain. As the underlying substrate is insulating, the change in electrical resistance is solely a measure of the structural changes in the conductive oxide induced by the applied mechanical strain.

One folding cycle consists of bending the sample so that the distance between the two electrical contacts decreases from the unfolded value, 31.5 mm. The minimum distance possible between the two contacts was 3.3 mm. If the edges of the sample is bent so that the backside of the film (uncovered with Cu_xCrO_2) are brought closer, a tensile strain is applied to the over layer of thin conducting film. Figure 5.12 shows the procedure schematically, as well as photos of the experimental setup at each stage of the bending cycle. The electrical resistance

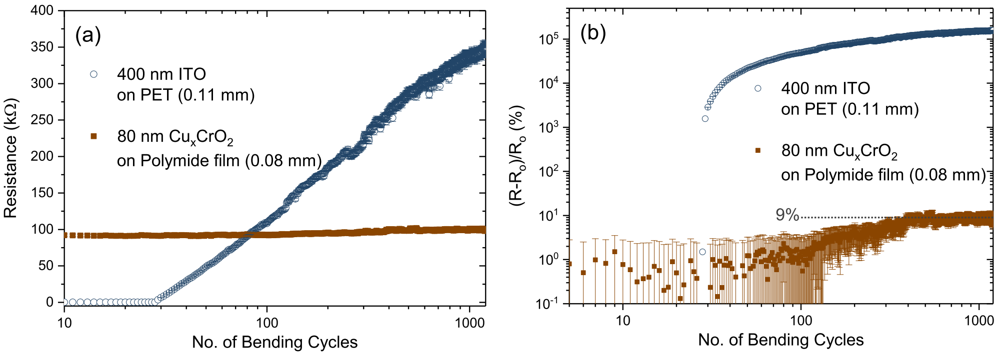

Figure 5.13: (a) absolute resistance change of the Cu_xCrO_2 vs. successive tensile strain bending cycles. The maximum applicable tensile strain of 0.8 % was used. For comparison, similar measurements for ITO (400 nm) is also shown to highlight the relative stability of the p-type Cu_xCrO_2. Before folding the end to end length of the ITO and CuCrO was 30 mm. At the point of maximal tensile strain, this length was reduced to 3.3 mm. (b) change in resistance $(R - R_o)$ normalised by the original film resistance (R_o) vs. successive tensile strain bending cycles

measurements were taken whenever the sample was in the unfolded position. This was due to a large amount of electrical noise due to the simple two wire electrical measurements use to measure the change in sheet resistance. However, this experiment was designed to montior the degradation of the Cu_xCrO_2 film upon polimide film after mechanical stess had been applied. The values of sheet resistance were used to montior any degradation the film as this would the most important quantity that would require to remain stable for electronic devices.

A side profile image was taken of the folded film at the maximum bending point. ImageJ software was then used to estimate the maximum radius of curvature, illustrated in figure 5.12(a). The thin oxide layers grown (80 - 400 nm) are considerably thinner than the substrate. The neutral axis is very close to the centre of the composite. Therefore, strain distributed to the conductive oxide is given by:

$$\text{strain} = \frac{t_s + t_{oxide}}{2r} \approx \frac{t_s}{2r} \tag{5.1}$$

where t_s and t_{oxide} are the thickness of the substrate and conductive oxide films, respectively, and r is the radius of curvature [6]. The mechanical strain applied is dependent on the substrate thickness. Therefore plotting the change in electrical resistance as a function radius of curvature after each bending cycle is not an absolute comparison. The strain induced (calculated using equation. (5.1)) as a function of the change in electrical resistance. Cu_xCrO_2 as it withstood the maximum applicable tensile strain of 0.8 %. No smaller radius of curvature could be obtained with the given films. The only possible way to further increase strain applied to Cu_xCrO_2, and possibly reach the threshold, Cu_xCrO_2 would need to be deposited on much thicker substrates.

5.4.3 Tensile Strain

Figure 5.13 shows the absolute resistance (a) and normalised change in resistance for 1200 bending cycles using the maximum tensile strain of 0.8 %. Within the first 500 cycles the resistance of Cu_xCrO_2 increased by 9 % and no further changes are observed for subsequent cycles. In contrast an ITO film measured for comparison saw a four order of magnitude increase in electrical resistance already within the first 100 cycles. Even though no change in electrical resistance was observed, the high initial resistance (91.6 kΩ) of a film Cu_xCrO_2 may mask any structural degradation in the film. A thin film deposited on a flexible substrate under tension will reach a threshold where channelling cracks appear which allow partial relaxation of stress, eventually followed by buckling delamination [42].

5.4.4 Compressive Strain

Scanning Electron Microscopy (SEM) images of the Cu_xCrO_2 film grown on polyimide film are shown in Fig. 5.14(d,e). The film, imaged after more than 100 cycles was mounted mechanically bent under maximum tensile strain. By mounting the films under tensile strain any thin channelling cracks should be exposed, however none were observed. This indicates the threshold strain where cracking of the film occurs has not been reached.

In contrast to the stability of the films under tensile strain, extensive compressive studies could not be performed due to limitations in the set-up. The

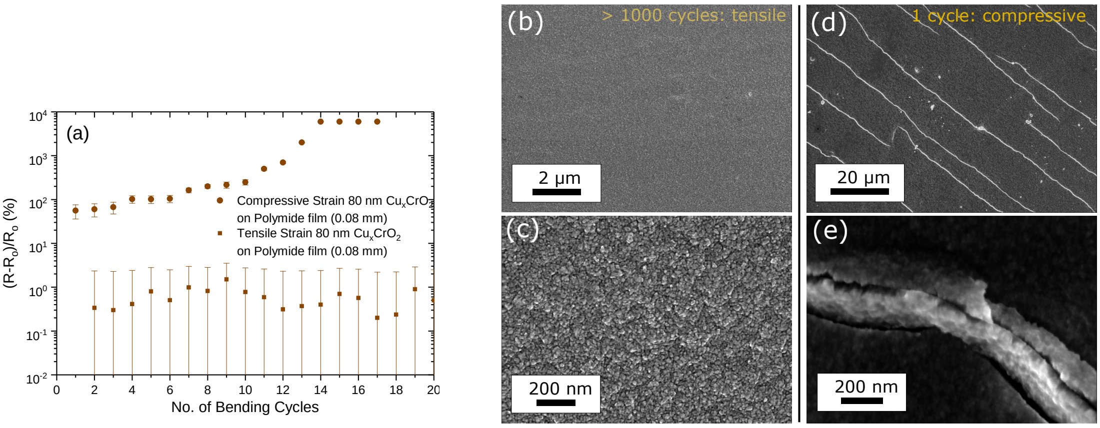

Figure 5.14: (a) change in resistance ($R - R_o$) normalised by the original film resistance (R_o) vs successive tensile/compressive strain bending cycles. The values for the compressive bending cycles saturate at 60 MΩ as this was the operational limit of our electrical measurement system. The large error in the change is resistance arises from the initial resistance reading is 91.6 kΩ while the electrical setup was optimised for readings in the Ω range. (b,c) Scanning Electron Microscopy (SEM) of the Cu_xCrO_2 on polyimide film after more than 1000 bending cycles. To expose potential cracking of the film the sample was mounted under maximum applicable tension; (d) Large scale SEM image of Cu_xCrO_2 on polyimide film after a single compressive strain cycle; (e) Magnified SEM image of a crack seen in (d).

compressive strain applied to the film relies on adheres of the oxide overlayer to the underlying substrae. However films that underwent manual compressive strain cycles (bending the sample down in a ∪-shape) showed large changes in electrical resistance, as shown in Fig. 5.14 (c). Subsequent SEM images show channelling cracks of the films treated this way (see figure 5.14). A small scale image of a single crack (figure 5.13 (g)) shows the film has buckled upwards, indicative of a delamination of the TCO layer leading to subsequent cracking of the film. Delamination of the film would be indicative of poor adherence of the Cu_xCrO_2 film to the underlying substrate. This could be improved by the deposition of a seeding layer upon the polyimide film prior to the growth of the Cu_xCrO_2 films [43].

5.4.5 Optical Properties upon Flexible Substrates

Figure 5.15 shows the optical transmittance and reflectance of the Cu_xCrO_2 films grown upon polyimide film. The bare polyimide film itself absorbs strongly above a photon energy of 2.5 eV. The Cu_xCrO_2, grown with thickness 80 nm, does not detrimentally effect the transmittance when grown upon the bare polyimide film.

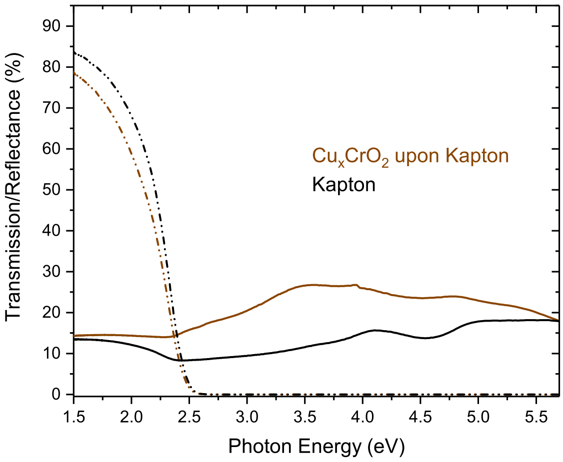

Figure 5.15: Ultra Violet-Visible Spectroscopy of Cu_xCrO_2 grown upon polyimide film. The dotted line denotes the transmission spectra of bare kapton and $CuCrO_2$ upon kapton. The solid line denotes the reflectance spectra.

5.5 Summary

To summarise, Cu_xCrO_2 has been deposited upon flexible substrates. Cu_xCrO_2 does not have any long range crystalline order above the nanoscale, which many oxides need for good electrical conductivity. In the films, O-Cu-O planes are ordered within 8-15 nm grains and the CrO_6 edge shared network is disordered. The films grown on polyimide film film have an electrical conductivity of 6 S cm^{-1} which does not significantly degrade when put under tension that causes significant degradation of ITO films. This work confirms that the nanocrystalline Cu_xCrO_2 is resilient to tensile strain below 0.8 %. This indicates it could be a potential candidate for large flexible electronics.

The next logical step would be to map the band alignment of Cu_xCrO_2 films within test devices but the lack of *in-situ* preparation methods by spray pyrolysis hinders that. It has been previously reported that band offset measurements can be made to give an indication of the alignment of oxide interfaces when samples cannot be prepared *in-situ*. However, the deficient nature of the films gives rise to some surface states, as outlined in section 5.3.1, which does not reflect the bulk state of the film. The disorder that is introduced by argon sputtering is likely to also alter the work function so it does not reflect the bulk properties of the film. As XPS is a surface sensitive technique it is best to characterise the incorporation of $\mathrm{Cu}_x\mathrm{CrO}_2$ within electronic devices by alternative methods [44].

Bibliography

[1] Monica Morales-Masis et al. “Transparent Electrodes for Efficient Optoelectronics”. *Advanced Electronic Materials* 3.5 (2017).

[2] Klaus Ellmer. “Past achievements and future challenges in the development of optically transparent electrodes”. *Nature Photonics* 6 (2012), 809–817.

[3] John F Wager. “Transparent electronics”. *Science* 300.5623 (2003), 1245–1246.

[4] Yi-Bing Cheng et al. “Print flexible solar cells”. *Nature* 539.7630 (2016), 488.

[5] Khalid Alzoubi et al. “Bending Fatigue Study of Sputtered ITO on Flexible Substrate”. *Journal of Display Technology* 7.11 (2011), 593.

[6] Darran R. Cairns et al. “Strain-dependent electrical resistance of tin-doped indium oxide on polymer substrates”. *Applied Physics Letters* 76.11 (2000), 1425.

[7] Kenji Nomura et al. “Room-temperature fabrication of transparent flexible thin-film transistors using amorphous oxide semiconductors”. *Nature* 432.7016 (2004), 488.

[8] J. C. Bernede et al. “XPS study of the band alignment at ITO-oxide (n-type MoO_3 or p-type NiO) interface”. *physica status solidi (a)* 209.7 (2012), 1291.

[9] Chuen-Shii Chou et al. “Preparation of a Counter Electrode with p-Type NiO and it’sApplications in Dye-Sensitized Solar Cell”. *International Journal of Photoenergy* 2010 (2010), 1.

[10] I. D. Parker. “Carrier tunneling and device characteristics in polymer light emitting diodes”. *Journal of Applied Physics* 75.3 (1994), 1656.

[11] David S. Ginley and Clark Bright. “Transparent Conducting Oxides”. *MRS Bulletin* 25.08 (2000), 15.

[12] T. Kamiya et al. “Electrical Properties and Structure of p-Type Amorphous Oxide Semiconductor x.ZnO.Rh_2O_3”. *Advanced Functional Materials* 15.6 (2005), 968.

[13] S. Narushima et al. “A p-Type Amorphous Oxide Semiconductor and Room Temperature Fabrication of Amorphous Oxide p-n Heterojunction Diodes”. *Advanced Materials* 15.17 (2003), 1409.

[14] L. Farrell et al. “Spray pyrolysis growth of a high figure of merit, nanocrystalline, p-type transparent conducting material at low temperature”. *Appl. Phys. Lett.* 107 (2015), 031901.

[15] Suddhasatta Mahapatra and Srinivasrao A Shivashankar. “Low-Pressure Metal–Organic Chemical Vapor Deposition of Transparent and p-Type Conducting $CuCrO_2$ Thin Films with High Conductivity”. *Chemical Vapor Deposition* 9.5 (2003), 238–240.

[16] Arpun R. Nagaraja et al. “Experimental Characterization of a Theoretically Designed Candidate p-Type Transparent Conducting Oxide: Li-Doped Cr_2MnO_4”. *Chem. Mater.* 26.15 (2014), 4598.

[17] R Nagarajan et al. “p-Type conductivity in the delafossite structure”. *International Journal of Inorganic Materials* 3.3 (2001), 265.

[18] A.P. Young and C.M. Schwartz. “Electrical conductivity and thermoelectric power of Cu_2O”. *Journal of Physics and Chemistry of Solids* 30.2 (1969), 249–252.

[19] Y. Park et al. “Work function of indium tin oxide transparent conductor measured by photoelectron spectroscopy”. *Applied Physics Letters* 68.19 (1996), 2699.

[20] S. B. Zhang, S.-H. Wei, and Alex Zunger. “Intrinsic n-type versus p-type doping asymmetry and the defect physics of ZnO”. *Physical Review B* 63.7 (2001).

[21] CW Zhong et al. “Stability of High performance p-type SnO TFTs”. *Physical and Failure Analysis of Integrated Circuits (IPFA), 2015 IEEE 22nd International Symposium on the.* IEEE. 2015, 84–87.

[22] Renhuai Wei et al. “Facile chemical solution synthesis of p-type delafossite Ag-based transparent conducting $AgCrO_2$ films in an open condition”. *Journal of Materials Chemistry C* 5.8 (2017), 1885–1892.

[23] Atsushi Kudo et al. “$SrCu_2O_2$: a p-type conductive oxide with wide band gap”. *Applied Physics Letters* 73.2 (1998), 220–222.

[24] K. Badeker. “Cadmium Oxide”. *Ann. Phys. (Leipzig)* 22 (1907), 749.

[25] L. Farrell et al. “Conducting mechanism in the epitaxial p-type transparent conducting oxide Cr_2O_3:Mg”. *Phys. Rev. B* 91.12 (2015), 125202.

[26] S Poulston et al. “Surface oxidation and reduction of CuO and Cu_2O studied using XPS and XAES”. *Surface and Interface Analysis* 24.12 (1996), 811–820.

[27] Mark C. Biesinger et al. “Resolving surface chemical states in XPS analysis of first row transition metals, oxides and hydroxides: Sc, Ti, V, Cu and Zn”. *Applied Surface Science* 257.3 (2010), 887.

[28] Leo Farrell et al. “Synthesis of nanocrystalline Cu deficient $CuCrO_2$: a high figure of merit p-type transparent semiconductor”. *J. Mater. Chem. C* 4.1 (2016), 126.

[29] Petru Lunca Popa et al. “Invisible electronics: Metastable Cu-vacancies chain defects for highly conductive p-type transparent oxide”. *Applied Materials Today* 9 (2017), 184–191.

[30] S. L. Hulbert et al. “Copper $L_{2,3}$ near-edge structure in Cu_2O”. *Physical Review B* 30.4 (1984), 2120.

[31] J. P. Hu et al. “On-site interband excitations in resonant inelastic x-ray scattering from Cu_2O”. *Physical Review B* 77.15 (2008), 155115.

[32] Sunjic Doniach and M Sunjic. “Many-electron singularity in X-ray photoemission and X-ray line spectra from metals”. *Journal of Physics C: Solid State Physics* 3.2 (1970), 285.

[33] T. Yokobori et al. “Electronic structure of the hole-doped delafossite oxides $CuCr_{1-x}Mg_xO_2$”. *Phys. Rev. B* 87.19 (2013), 195124.

[34] David O. Scanlon and Graeme W. Watson. “Understanding the p-type defect chemistry of $CuCrO_2$”. *J. Mater. Chem.* 21.11 (2011), 3655.

[35] Michael Nolan and Simon D. Elliott. “Tuning the Transparency of Cu_2O with Substitutional Cation Doping”. *Chem. Mater.* 20.17 (2008), 5522.

[36] Hiroshi Kawazoe et al. “p-type electrical conduction in transparent thin films of $CuAlO_2$”. *Nature* 389 (1997), 939.

[37] Xiaoming Wang, Weiwei Meng, and Yanfa Yan. “Electronic band structures and excitonic properties of delafossites: A GW-BSE study”. *Journal of Applied Physics* 122.8 (2017), 085104.

[38] David O. Scanlon et al. “Effect of Cr substitution on the electronic structure of $CuAl_{1-x}Cr_x O_2$”. *Phys. Rev. B* 79.3 (2009), 035101.

[39] Hiroki Hiraga et al. “Electronic structure of the delafossite-type $CuMO_2$ (M = Sc, Cr, Mn, Fe, and Co): Optical absorption measurements and first-principles calculations”. *Physical Review B* 84.4 (2011), 041411.

[40] T. Arnold et al. “X-ray spectroscopic study of the electronic structure of $CuCrO_2$”. *Phys. Rev. B* 79.7 (2009), 075102.

[41] Jonas Deuermeier et al. “Highly conductive grain boundaries in copper oxide thin films”. *Journal of Applied Physics* 119.23 (2016), 235303.

[42] B. Cotterell and Z. Chen. “Buckling and cracking of thin films on compliant substrates under compression”. *International Journal of Fracture* 104.2 (2000), 169.

[43] Rong Long and Martin L Dunn. “Channel cracks in atomic-layer and molecular-layer deposited multilayer thin film coatings”. *Journal of Applied Physics* 115.23 (2014), 233514.

[44] Alessio Giampietri, Giovanni Drera, and Luigi Sangaletti. “Band Alignment at Heteroepitaxial Perovskite Oxide Interfaces. Experiments, Methods, and Perspectives”. *Advanced Materials Interfaces* 4.11 (2017).

Chapter 6

Conclusions and Outlook

This thesis has focused generally on studying the properties of two novel p-type TCOs: $Cr_{2-x}Mg_xO_3$ and Cu_xCrO_2. Within this body of work there have been two main focuses: the first was to investigate the fundamental physics behind the mobility of charge carriers within these two chromium based p-type transparent conducting oxides. The mobility within both oxides was not quantifiable by Hall effect technique. This in itself is not remarkable but a more general trend within the literature was observed, that chromium containing oxides all had an immeasurable mobility by DC Hall effect [1, 2]. Resonant Photoemission Spectroscopy (RPES) carried out on $Cr_{2-x}Mg_xO_3$ and Cu_xCrO_2 films could locate the position of the unoccupied density of states (holes) within the valence band and the elemental states they were correlated to. The position of the charge carriers associated with the Cr 3*d* states, determined by RPES, show striking similarity to one another (figure 6.1 (b)). As the Cu_xCrO_2 and $Cr_{2-x}Mg_xO_3$ films differed significantly in long range crystalline order (see figure 6.1 (a)) the similarity in the Cr 3*d* states suggests the localisation of the holes. This correlates well with the previous works on crystalline $CuCrO_2$:Mg films where the top of the valence band exhibited a strong chromium resonance around the Cr 3*p*-3*d* transition.

Even thought there is no copper resonance seen within the films so the precise location of the Cu 3*d* states could be verified, there is an increase in DOS with increasing copper content in Cu_xCrO_2 films below the valence band maximum.

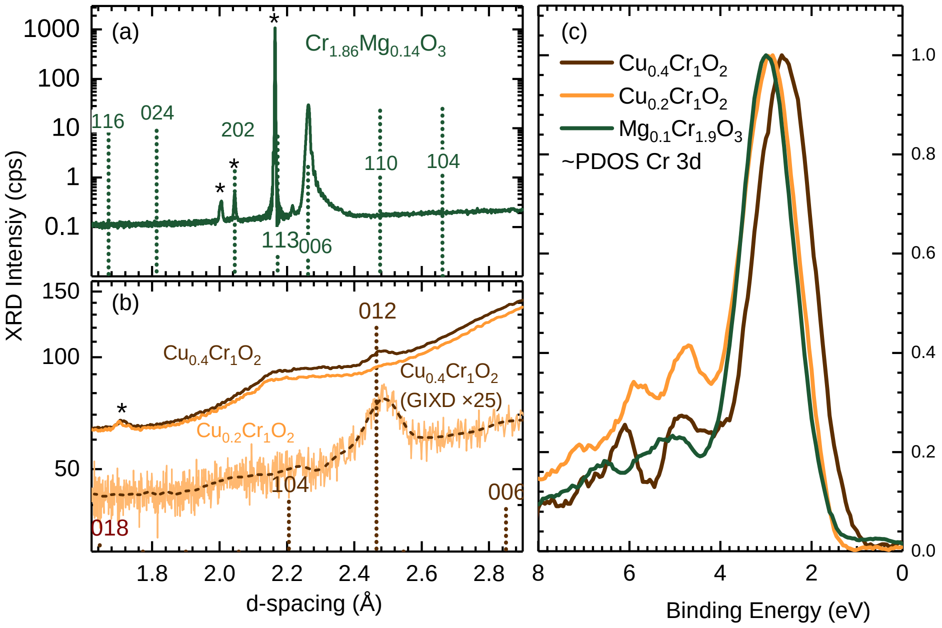

Figure 6.1: (a) and (b) X-ray diffraction of the analysed Cu_xCrO_2 and $Cr_{2-x}Mg_xO_3$ films. (c) Comparison of Cr 3*d* partial density of states (PDOS) within three films $Cr_{2-x}Mg_xO_3$, $Cu_{0.2}CrO_2$ and $Cu_{0.4}CrO_2$

This valence band maximum of these films is composed of the Cr 3*d* states. This would seem to indicate that the Cu 3*d* states lie below the valence band but increase the hybridisation between the O 2*p* and Cr 3*d* states.

It appears then that $CuCrO_2$ is then different from other delafossites, since charge carriers are strongly correlated due to the half-filled 3*d* states of chromium. More generally chromium containing p-type oxides will have highly localised carriers within the Cr 3*d* states.

Even though both chromium based oxides have an immeasurable Hall effect voltage (low mobility) there are many applications where this does not limit the use of p-type TCOs. Due to the rarity of these materials they are hence investigated in prototype devices where mobility is not a concern. This is the second main focus of this thesis.

One of these applications is a selective contact within thin film solar cells. In organic solar cells the anode ITO has poor band alignment to current organic active layers. To improve the extraction of holes from the cell a high work function p-type oxide is often placed between the anode and active layer. The valence band and conduction band offset between ITO and a p-type oxide will govern largely how effective the p-type material is as a selective contact. Therefore, instead of incorporating $Cr_{2-x}Mg_xO_3$ into active devices as a selective contact, the energy band alignment of $Cr_{2-x}Mg_xO_3$ was performed with ITO. Theoretically the band alignment of ITO-$Cr_{2-x}Mg_xO_3$ can be predicted by Anderson's rule. The result of using Anderson's rule to align this interface can be seen from figure 6.2 (a). It produced a very stark difference to the experimentally determined values in figure 6.2(b). This is because Anderson's rule ignores the chemical bonding and surface states that may be created by bringing two surfaces into contact. The experimentally determined Type II band alignment of $Cr_{1.76}Mg_{0.24}O_3$ and ITO with a relatively large conduction band offset would indicate it could be used as an selective in solar cells. However, the alignment of the p-type oxide to the active layers themselves within the solar cells would also have to be considered. Nevertheless the future outlook of this thesis would be seek the incorporation of $Cr_{2-x}Mg_xO_3$ as a selective contact in solar cells where ITO is being used as the anode but has poor alignment to the active layer.

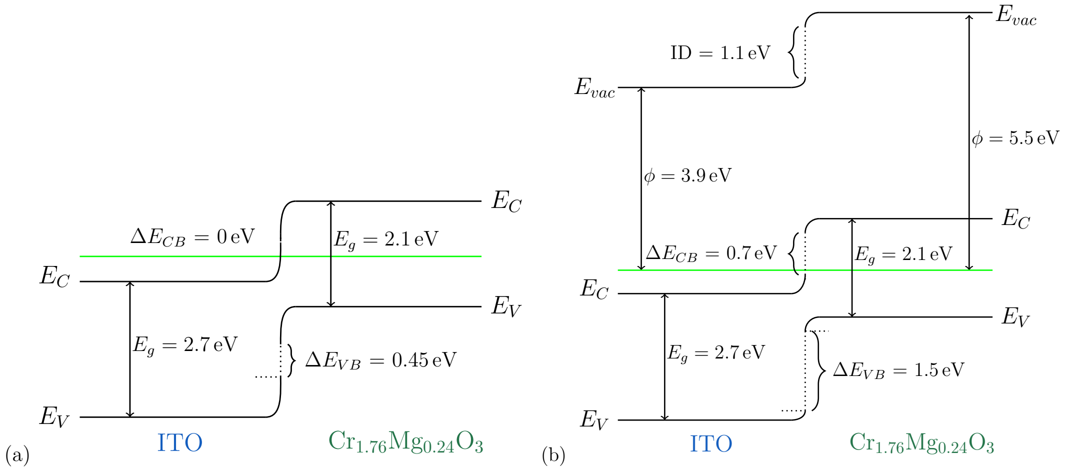

Figure 6.2: (a) Energy band diagram predicted by common anion rule. (b) Experimentally determined energy band diagram. The work function for ITO and $Cr_{1.76}Mg_{0.24}O_3$ were assumed to be the same values as determined for the energy band alignment studies by UPS. E_c = conduction band minimum, E_v = valance band maximum, E_g = fundamental band gap, WF= workfunction, ΔE_{vb} = valance band offset , ΔE_{cb} = conduction band offset, Fermi level is denoted by the green line

Another application explored was the use of $Cr_{2-x}Mg_xO_3$ within transparent rectifying diodes. A report by Arca et al. reported that $Cr_{2-x}Ni_xO_3$ and aluminium doped ZnO (AZO) did not show rectifying behaviour due to the high carrier density of both $Cr_{2-x}Ni_xO_3$ and AZO [3]. By lowering the carrier concentration using intrinsically doped zinc oxide it was theorised a larger built in potential could be created, producing rectifying behaviour. Unfortunately complications with retaining the electrical conductivity of intrinsic ZnO when depositing $Cr_{2-x}Mg_xO_3$ via MBE occurred. The p-type $Cr_{2-x}Mg_xO_3$ films had to be deposited at room temperature upon ZnO. Nevertheless, rectifying behaviour between ZnO and $Cr_{2-x}Mg_xO_3$ was observed. The diode produced an on/off ratio of $\approxeq 10^3$ determined at a bias voltage 1.5/-1.5 V at 300 K. This is not competitive with the NiO/ZnO diode which showed high rectification on/off ratios of 10^9. The $Cr_{2-x}Mg_xO_3$-ZnO diodes has a rather high ideality factor of between seven and thirteen depending on the temperature that the IV characteristics were measured at. The energy band alignment of the two surfaces of ZnO and $Cr_{2-x}Mg_xO_3$ indicated defect states are present at the interface: this is likely the source of such high ideality factors for the diodes.

The outlook for this work will be to explore the deposition of the $Cr_{2-x}Mg_xO_3$-ZnO stack reversed, i.e, the p-type layer will be deposited first. The ZnO films can be annealed in a nitrogen atmosphere after the deposition of the n-type layer upon $Cr_{2-x}Mg_xO_3$. For these studies the effects of nitrogen annealing upon the $Cr_{2-x}Mg_xO_3$ layer will have to be investigated. Also the *in-situ* transfer of samples between the magnetron sputtering system and XPS will have to be developed so the interface properties by band alignment can be investigated.

The future outlook of this thesis would also include characterising the optical response of the $Cr_{2-x}Mg_xO_3$-ZnO diodes as ZnO has a wide direct band gap of 3.3 eV and with a large exciton binding energy of 60 meV, (larger than Gallium Nitride). These features make it a promising candidate for applications using blue and ultraviolet light sources, such as UV detectors [4].

Due to the difficulty in retaining conductivity of ZnO films under the optimum growth condition for p-type oxides it could likely be more fruitful to seek an alternative intrinsic n-type TCO. As indicated by the Type II band alignment of ITO-$Cr_{2-x}Mg_xO_3$, In_2O_3 may be a possible alternative which could withstand higher deposition temperatures and produce a less defect interface, possibly increasing the ideality factor of the diodes.

Finally, the resilience of Cu_xCrO_2 to mechanical strain was investigated. In spite of the prevalence of TCOs within electronic devices it has been a passive layer until the development of the n-type TCO, Indium Gallium Zinc Oxide (IGZO). The high mobility that could be achieved at room temperature is the reason it is competitive with amorphous silicon as an active layer in flat screen displays [5]. In contrast, p-type oxides have extremely high deposition temperatures which as seen from above can be problematic. The analogous amorphous p-type TCO: Rhodium Zinc Oxide has very low conductivity so is not appropriate for many industrial applications. The relatively low deposition temperature of Cu_xCrO_2 films made it compatible with growth on polyimide films. The lack of long range order the material required to retain electrical conductivity and the fact that it shares a CrO_6 edge sharing network similar to that of the RhO_6 network in amorphous Zinc Rhodium Oxide meant it withstand the maximum applicable tensile strain of 0.8 %. If the thickness of the flexible substrate on which the films were deposited was increased the maximum application stress could also be increased further to reach the threshold at which the films would break but the initial results are very promising as a large area flexible electrode.

Bibliography

[1] Kelvin HL Zhang et al. “P-type transparent conducting oxides”. *Journal of Physics: Condensed Matter* 28.38 (2016), 383002.

[2] E Norton et al. “X-ray spectroscopic studies of the electronic structure of chromium-based p-type transparent conducting oxides”. *Physical Review B* 93.11 (2016), 115302.

[3] Elisabetta Arca, Michael A McInerney, and Igor V Shvets. “Band alignment at the interface between Ni-doped Cr_2O_3 and Al-doped ZnO: implications for transparent p-n junctions”. *Journal of Physics: Condensed Matter* 28.22 (2016), 224004.

[4] ZhanWu Wang, Yonggao Yue, and Yan Cao. “Influence of annealing temperature on properties of nitrogen-doped zinc oxide films deposited by magnetron sputtering”. *Superlattices and Microstructures* 65 (2014), 7–13.

[5] John F Wager. “Transparent electronics”. *Science* 300.5623 (2003), 1245–1246.

Appendices

Appendix A

Energy Band Alignment: Lineshape of Core Levels

A.1 $Cr_{2-x}Mg_xO_3$ - ITO Interface

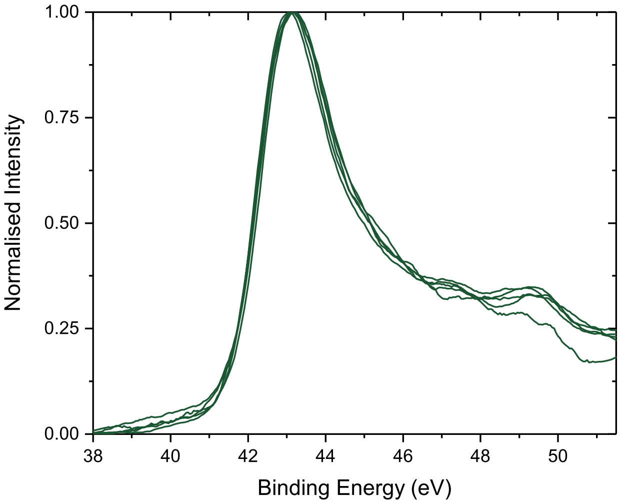

Figure A.1: Line shape of the Cr 3p core level across the ITO-$Cr_{1.76}Mg_{0.24}O_3$ interface.

The lineshape of the core levels for $Cr_{1.76}Mg_{0.24}O_3$ and ITO are plotted in Figures A.1 & itolineshapechanges. As mentioned within the main text, it is cruical to evaluate the change in lineshape as the film is deposited upon the substrate.

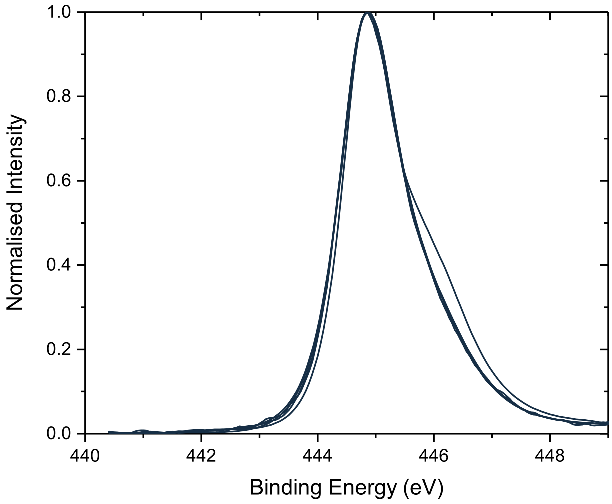

Figure A.2: Line shape of the In $3d_{5/2}$ core level across the ITO-$Cr_{1.76}Mg_{0.24}O_3$ interface.

For the Figure A.1 the peak center of each Cr 3*p* core level was shifted to the reference binding of the bulk 30 nm Cr 3p core level binding energy of 43.00 eV. All core levels were area normalised. No changes in FWHM or additional components are observed.

For the Figure A.2 the peak center of In $3d_{5/2}$ core level was shifted to the reference binding of the 90 nm In $3d_{5/2}$ core level binding energy of 444.80 eV. All core levels were area normalised. After deposition of 4Åof $Cr_{1.76}Mg_{0.24}O_3$a reduction in In_{II} component is seen. No further changes in FWHM or additional components are observed.

A.2 $Cr_{2-x}Mg_xO_3$ - ZnO Interface

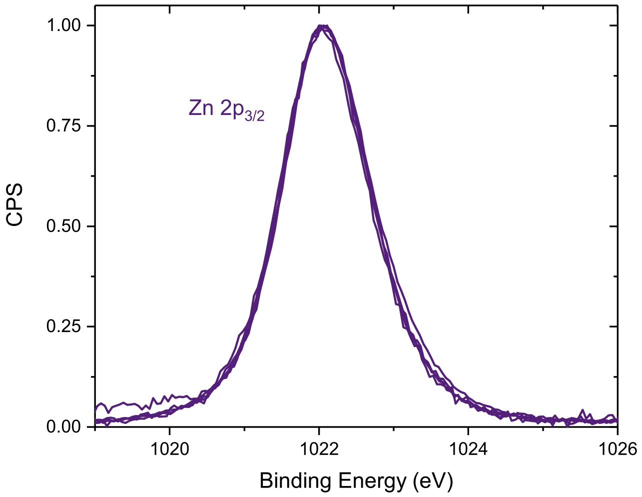

Figure A.3: Line shape of the Zn $2p_{3/2}$ core level across the ZnO-$Cr_{1.82}Mg_{0.18}O_3$ interface.

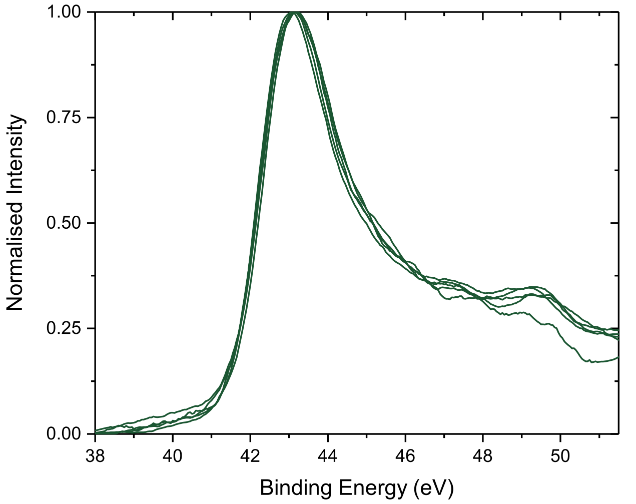

Figure A.4: Line shape of the Cr 3*p* core level across the ZnO-$Cr_{1.82}Mg_{0.18}O_3$ interface.

In Figure A.3, the peak centre of each core level was shifted to the reference binding of the 100 nm Zn $2p_{3/2}$ core level binding energy of 1022 eV. All core levels were area normalised and in Figure A.4, the peak center of the Cr 3*p* was shifted to the reference binding of the bulk 30 nm Cr 3p core level binding energy of 43.00 eV. All core levels were area normalised. No changes in FWHM or additional components are observed.

Appendix B

Fundamental Band Gap of Cr_2O_3

The magnitude of the fundamental band gap was crucial to properly understand the CBO offsets that occur between n-type TCOs and p-type Cr_2O_3 and $Cr_{2-x}Mg_xO_3$. Density functional theory calculations were performed by Glenn Moynihan under the supervision of Prof. David O'Reagan. U was calculated from first-principles, the methodology of which is outlined below.

B.1 First Principles Method of Solving for the Hubbard Parameter of Cr_2O_3

Spin-polarised density-functional theory (DFT) calculations are performed in the linear-scaling ONETEP package [1, 2] with a Local Density Approximation (LDA) [3] for the exchange-correlation functional, and the projector-augmented wave (PAW) method [4] to treat the core states.

The kinetic energy cutoff is 1100 eV and the cutoff radius for the support functions, given by non-orthogonal generalised Wannier functions (NGWFs) [5], is 12 a_0 such that total energetic convergence is achieved to within 2×10^{-5} Ha per atom. A 3x3x2 supercell is utilised with Brillouin zone with sampling at the Γ-point.

The non-self-consistent U and J values for chromia are computed according to the variational linear response method described in [6](unpublished), which is adapted from the method by Cococcioni and De Gironcoli [7].

To compute the U and J, a uniform potential shift α is applied to the $3d$ orbitals in one Cr atom in the crystal and varied between ±0.2 eV in intervals of 0.1 eV.

The computed Hubbard parameter is U=2.8±0.1 eV, and the corresponding Hund's exchange parameter is $J = 0.435 \pm 0.004$ eV, which, to our knowledge, is the first time these have been computed for chromia from a linear-response approach and compare reasonably well with previous values [8–10].

The parameters were then used within the rotationally invariant DFT+U [7] and DFT+U+J [12] malfunction applied to all Cr atoms, where the Hubbard projectors are defined as the occupied Kohn-Sham Cr 3d orbitals.

The band gap for the DFT+U calculation is 2.10 eV and the magnetic moment is 2.56 μB (see Figure B.1), which are significant improvements on the DFT (PBE) values of 2.27 eV and 2.30 μB, respectively.

The band gap for the DFT+U+J calculation is 2.06 eV and the magnetic moment is 2.59 μB, which present a marginal difference compared to the DFT+U results, see Figure B.2.

The density of states (DOS) of both calculations were then calculated with a Gaussian smearing of 0.29 eV, this to compare the XPS valence band spectral features which are limited by an experimental resolution limit of FWHM=0.58 eV.

The constituent states of the valence band from -1.5 eV up to the Fermi level are, on average, 70% Cr and 30% O, whereas the conduction band is composed of 80% Cr and 20% O up to 4 eV above the Fermi level, which confirms the Mott-Hubbard character [10].

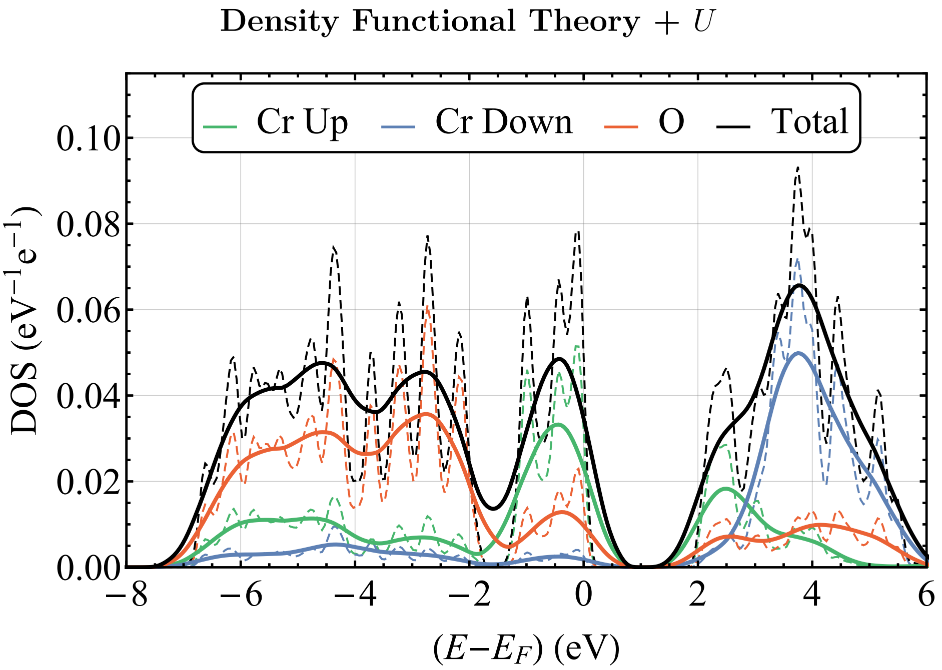

Figure B.1: Occupied and unoccupied density of states for Cr_2O_3 calculated using density functional theory + U, where the value of the Hubbard parameter has been determined from first principles to be 2.8±0.1 eV

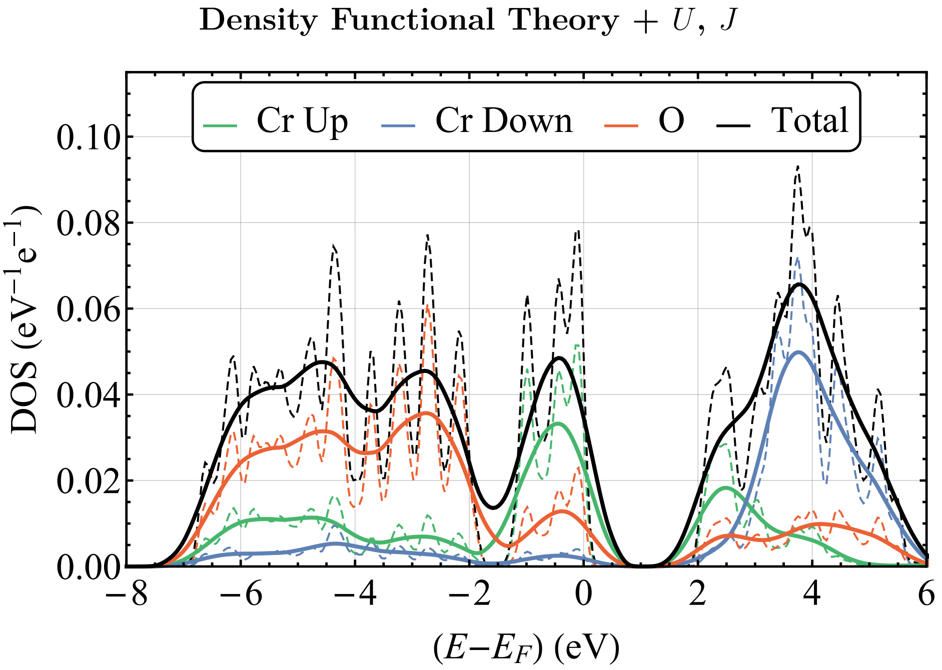

Figure B.2: Occupied and unoccupied density of states for Cr_2O_3 calculated using density functional theory + U, J, the addition of the J does not change the projection of the density of states but gives a better agreement with the expected experimental value for the magnetic moment for Cr_2O_3

Experimental Observation of the Occupied Density States and Joint Density of States

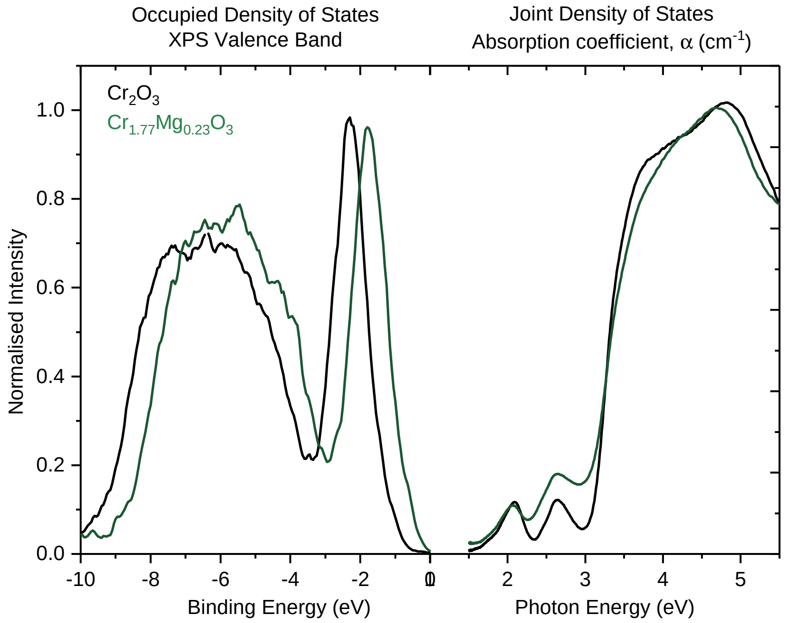

Figure B.3: The two films, $Cr_2O_3$and $Cr_{1.78}Mg_{0.22}O_3$, were grown at a deposition temperature of 873 K upon Al_2O_3(0001). The valence band was measured via XPS. The absorption coefficent was calculated from Reflectance and Transmission spectra from UV-Vis. The thickness of the films was measured by XRR.

B.2 Comparison with Experimentally Observed Band Gap

When the Guassian smearing is applied to the as calculated occupied density of states in Figures B.1 and B.2, a comparison with high resolution XP spectra of the valence band shows similar features are resolved experimentally.

The absorption coefficient of Cr_2O_3 and $Cr_{1.76}Mg_{0.24}O_3$ films has been calculated by the following relation:

$$\alpha = \frac{-ln(T+R)}{t} \tag{B.1}$$

where T is the transmittance, R is the reflectance and t is the thickness of the thin film being analysed. The thickness of a thin film was measured precisely by X-ray Reflectivity (XRR). The shape of the calculated unoccupied density of states does not match the absorption coefficient, which is not surprising as the DFT calculation would have to incoporate a weighing to optically allowed transitions to get a better match the optical features. However, what is notable is the magnitude of band gap calculated matched the onset of first sub band gap optical transition. This lends further evidence to the magnitude of the fundamental gap between the conduction and valence bands is less than the optical band gap of 3.4 eV.

Bibliography

[1] Chris-Kriton Skylaris et al. “Introducing ONETEP: Linear-scaling density functional simulations on parallel computers”. *The Journal of chemical physics* 122.8 (2005), 084119.

[2] David D O Regan et al. “Linear-scaling DFT+ U with full local orbital optimization”. *Physical Review B* 85.8 (2012), 085107.

[3] John P Perdew and Alex Zunger. “Self-interaction correction to density-functional approximations for many-electron systems”. *Physical Review B* 23.10 (1981), 5048.

[4] Peter E Blöchl. “Projector augmented-wave method”. *Physical review B* 50.24 (1994), 17953.

[5] Nicola Marzari et al. “Maximally localized Wannier functions: Theory and applications”. *Reviews of Modern Physics* 84.4 (2012), 1419.

[6] Glenn Moynihan, Gilberto Teobaldi, and David D ORegan. “A self-consistent ground-state formulation of the first-principles Hubbard *U* parameter validated on one-electron self-interaction error”. *arXiv preprint 1704.08076* (2017).

[7] Matteo Cococcioni and Stefano De Gironcoli. “Linear response approach to the calculation of the effective interaction parameters in the LDA+ U method”. *Physical Review B* 71.3 (2005), 035105.

[8] A Rohrbach, J Hafner, and G Kresse. “Ab initio study of the (0001) surfaces of hematite and chromia: Influence of strong electronic correlations”. *Physical Review B* 70.12 (2004), 125426.

[9] Nicholas J Mosey and Emily A Carter. “Ab initio evaluation of Coulomb and exchange parameters for DFT+ U calculations”. *Physical Review B* 76.15 (2007), 155123.

[10] Siqi Shi, Aleksander L Wysocki, and Kirill D Belashchenko. “Magnetism of chromia from first-principles calculations”. *Physical Review B* 79.10 (2009), 104404.